

A COMPUTATIONAL MODEL FOR FLUID-POROUS STRUCTURE INTERACTION

by

Rana Zakerzadeh

B.Sc. in Biomedical Engineering, Tehran Polytechnic, 2009

M.Sc. in Biomedical Engineering, Tehran Polytechnic, 2011

Submitted to the Graduate Faculty of
Swanson School of Engineering in partial fulfillment
of the requirements for the degree of
Doctor of Philosophy

University of Pittsburgh

2016

UNIVERSITY OF PITTSBURGH
SWANSON SCHOOL OF ENGINEERING

This dissertation was presented

by

Rana Zakerzadeh

It was defended on

July 26, 2016

and approved by

Peyman Givi, Ph.D. Distinguished Professor and James T. MacLeod Professor, Department of
Mechanical Engineering & Materials Science

Spandan Maiti, Ph.D., Assistant Professor, Department of Bioengineering

Anne Robertson, Ph.D., William Kepler Whiteford Professor, Department of Mechanical
Engineering & Materials Science

Dissertation Director: Paolo Zunino, Ph.D., Assistant Professor, Department of Mechanical
Engineering & Materials Science

Copyright © by Rana Zakerzadeh

2016

A COMPUTATIONAL MODEL FOR FLUID-POROUS STRUCTURE INTERACTION

Rana Zakerzadeh, PhD

University of Pittsburgh, 2016

In this work, we utilize numerical models to investigate the importance of poroelasticity in Fluid-Structure Interaction, and to establish a connection between the apparent viscoelastic behavior of the structure part and the intramural filtration flow. We discuss a loosely coupled computational framework for modeling multiphysics systems of coupled flow and mechanics via finite element method. Fluid is modeled as an incompressible, viscous, Newtonian fluid using the Navier-Stokes equations and the structure domain consists of a thick poroelastic material, which is modeled by the Biot system. Physically meaningful interface conditions are imposed on the discrete level via mortar finite elements or Nitsche's coupling. We also discuss the use of our loosely coupled non-iterative time-split formulation as a preconditioner for the monolithic scheme.

We further investigate the interaction of an incompressible fluid with a poroelastic structure featuring possibly large deformations, where the assumption of large deformations is taken into account by including the full strain tensor. We use this model to study the influence of different parameters on energy dissipation in a poroelastic medium. The numerical results show the effects of poroelastic parameters on the pressure wave propagation, filtration of the incompressible fluid through the porous media, and the structure displacement.

Keywords: Fluid-structure interaction, Poroelasticity, Finite elasticity, Energy dissipation.

TABLE OF CONTENTS

PREFACE	XII
1.0 INTRODUCTION	1
2.0 LINEAR MODEL FOR FPSI	6
2.1 FORMULATION	8
2.1.1 What is the Nitsche’s method?	11
2.2 WEAK FORMULATION	13
2.3 NUMERICAL PROCEDURE	17
2.3.1 Partitioned scheme	18
2.3.2 Monolithic scheme	21
2.4 NUMERICAL SIMULATIONS	24
2.4.1 FSI analysis of pulsatile flow in a compliant channel	25
2.4.2 Performance analysis of loosely coupled scheme as a preconditioner	29
2.4.3 Convergence analysis	32
2.4.4 Absorbing boundary condition	34
2.4.5 Sensitivity analysis of poroelastic parameters	36
2.5 SUMMARY	41
3.0 ENERGY DISTRIBUTION IN THE COUPLED FSI PROBLEMS	42
3.1 BACKGROUND	43

3.2	FORMULATION	46
3.2.1	Energy estimation	50
3.3	NUMERICAL PROCEDURE	53
3.4	NUMERICAL SIMULATIONS	55
3.4.1	Benchmark 1: FSI analysis for short pressure wave	56
3.4.2	Benchmark 2: FSI analysis under physiological condition	59
3.4.3	Energy balance analysis	61
3.4.4	Viscoelastic model analysis	67
3.4.5	Poroelastic Model Analysis	70
3.5	SUMMARY	71
4.0	NONLINEAR MODEL FOR FPSI	72
4.1	FORMULATION	75
4.1.1	Fluid model in the ALE form	78
4.1.2	Lagrangian formulation of the structure model	80
4.1.3	Coupling conditions over the interface	82
4.2	NUMERICAL PROCEDURE	83
4.2.1	Spatial discretization using finite elements	84
4.2.2	Time discretization	86
4.2.3	Structure problem	87
4.2.3.1	Newton's method	89
4.2.4	Darcy problem	91
4.2.5	Fluid problem	92
4.2.6	Mesh movement	93

4.3	NUMERICAL SIMULATIONS.....	94
4.3.1	Benchmark 1: FSI analysis of pulsatile flow in a compliant channel	95
4.3.2	Benchmark 2: FSI analysis of the flow in a cross-section model.....	97
4.3.3	Sensitivity analysis of model parameters.....	101
4.3.3.1	Loading rate and source term amplitude	101
4.3.3.2	Young’s modulus.....	104
4.3.3.3	Storage coefficient	105
4.3.3.4	Hydraulic conductivity	106
4.4	DISCUSSION.....	107
5.0	CONCLUSION.....	114
	BIBLIOGRAPHY	120

LIST OF TABLES

Table 1. Fluid and structure parameters.....	25
Table 2. Average number of GMRES iterations for different time steps	31
Table 3. Convergence in time of the monolithic and the partitioned scheme.....	33
Table 4. Physical and numerical parameters for benchmark problem 1	56
Table 5. Physical and numerical parameters for benchmark problem 2.....	60
Table 6. Physical and numerical parameters for benchmark problem 1	98
Table 7. Mesh sensitivity results.....	100
Table 8. Exponent of the power law for different parameters on the sensitivity analysis	112

LIST OF FIGURES

Figure 1. Schematic of the problem configuration	8
Figure 2. Schematic of the interface conditions in FPSI system	12
Figure 3. Result for pressure in fluid and displacement in structure	26
Figure 4. Top panel: displacement of the fluid-structure interface at times 1.5, 3.5 and 5.5 ms from left to right. Bottom panel: intramural flow $q.n$ at different planes in the arterial wall, located at the interface, at the intermediate section and at the outer layer	27
Figure 5. Snapshots of the pressure and solid deformation at 2ms, 4ms, and 6ms from left to right for straight cylinder	28
Figure 6. Snapshots of the pressure and solid deformation at 2ms, 4ms, and 6ms from left to right for curved vessel.....	29
Figure 7. Pressure obtained with (right) and without (left) prescribing absorbing boundary condition for the outflow at $t = 2\text{ms}$ (up) and $t = 8\text{ms}$ (bottom).....	35
Figure 8. Mean fluid pressure with (dashed line) and without (solid line) absorbing boundary condition for outflow	36
Figure 9. Displacement of the fluid-wall interface for different k values at $t=3.5\text{ms}$	39
Figure 10. Displacement of the fluid-wall interface at $t=3.5\text{ms}$ for $\lambda = 4.28 \times 10^6$ and $\lambda = 4.28 \times 10^5$	40
Figure 11. Displacement of the fluid-wall interface at $t=3.5\text{ms}$ for different values of storativity	40
Figure 12. Computational approach; (a) poro-viscoelastic model of the arterial wall (left), schematic of the fluid and structure domains (right); (b) inflow/outflow pressure waves and choice of snapshot times (left); computational mesh (middle), Coupling conditions in Fluid-poroviscoelastic structure interaction (right).....	52
Figure 13. A snapshot of the pressure wave traveling from left to right coupled with the radial component of the structure displacement. The legend shows the values for the pressure (bottom scale) and displacement (top scale)	57
Figure 14. Fluid–structure interface displacement (left panel) and mean pressure (right panel) versus z , at $t = 4, 8, 12$ ms, computed with the monolithic scheme by Quaini [73] (time	

step =e-4; dashed line) and with operator-splitting scheme [72] (time step=5e-5; dotted line). Our result is plotted using a solid line.....	58
Figure 15. Time evolution of the energy in each component for elastic (top, left), viscoelastic (top, right) and poroelastic cases with $k= 5\times 10^{-6} \text{ cm}^3 \text{ s/g}$ (left) and $k= 5\times 10^{-9} \text{ cm}^3 \text{ s/g}$ (right) in benchmark problem 1.....	58
Figure 16. Time evolution of energy components for viscoelastic case with $\eta =3\times 10^4 \text{ dyne.s/cm}^2$; The plot shows kinetic and stored energy in wall (circle), fluid kinetic energy (dash-dot line) , fluid viscous dissipation (dotted line), wall viscoelastic loss (dashed line), total energy (star), and total input energy to the system (solid line); for the straight tube (top panel) and stenosed tube (bottom panel)	62
Figure 17. Available energy at the final time (5ms) in each component for different constitutive models in benchmark problem 1 (first plot from top); energy distribution at the snapshot times for elastic, viscoelastic ($\eta =3\times 10^4 \text{ dyne.s/cm}^2$) and poroelastic models.	64
Figure 18. Energy dissipation rate (relative to systole) for viscous loss (top), viscoelastic loss (middle) and filtration energy loss (bottom) during one heart cycle.....	65
Figure 19. Time lag in viscoelastic model between normalized pressure in the channel (solid line) and normalized wall radial displacement (dashed line) at the midpoint of the channel for different values of wall viscous modulus , $\eta =3\times 10^4 \text{ dyne.s/cm}^2$ (top), $\eta =1\times 10^4 \text{ dyne.s/cm}^2$ (middle), and poroelastic model (bottom) are shown in left panel, corresponding hysteresis plots for each case obtained by plotting the fluid pressure at the center of the channel versus the radial wall displacement are provided in right panel.	68
Figure 20. Analysis of energy flow (top); Energy diagram in poroelastic and viscoelastic models (bottom)	69
Figure 21. Geometric configuration, reference (left) and present (right)	75
Figure 22. Left (weak pressure wave), right (strong pressure wave), Attached plots shows comparison for displacement at the middle of the wall for linear (dashed) and nonlinear (solid line) elasticity.	96
Figure 23. Schematic of the geometrical model for benchmark problem 2.....	97
Figure 24. Snapshot for fluid and wall during expansion phase in the model at 2ms; colors represent fluid pressure and wall displacement.....	99
Figure 25. Filtration velocity through the wall and Darcy pressure at t=2ms for the test case with loading rate=6ms and $k=5\times 10^{-6}$	99
Figure 26. Hysteresis loop for different mesh size (left), Schematic of the measuring indicator used in the sensitivity analysis (right)	100

Figure 27. Mesh sensitivity analysis plots for different mesh sizes (left) and time steps (right)	101
Figure 28. Different source terms g	102
Figure 29. Comparing loops for different values of loading rate, with $k=5e-6$	102
Figure 30. Comparing hysteresis loop for different values of the source term g	103
Figure 31. Comparing fluid pressure, wall displacement, Darcy pressure and filtration velocity for different values of loading rate, 3ms (dashed), 6ms (dotted), and 12ms (solid) lines	103
Figure 32. Comparing hysteresis loop for different values of Young's modulus.....	104
Figure 33. Comparing fluid pressure, wall displacement, Darcy pressure and filtration velocity for different values of Young's modulus, $0.1 \times E$ (dashed), E (dotted), and $10 \times E$ (solid) lines	104
Figure 34. Comparing hysteresis loop for different values of storage coefficient s_0	105
Figure 35. Comparing hysteresis loop for different values of hydraulic conductivity	106
Figure 36. Time variation of mass conservation terms in the Biot model through the wall thickness	107
Figure 37. Schematic of the measuring indicator used in the sensitivity analysis.....	110
Figure 38. Sensitivity results for dependence of hysteresis loop to the model parameters	111

PREFACE

به نام خداوند بخشنده مهربان

A PhD was always a part of my life plan. Thinking back, I'm so glad that I decided to come to Pitt. It made me love my PhD and I kind of wish it wasn't over!

Before everything else; I want to especially acknowledge my adviser Paolo Zunino, and my doctoral committee members: Anne Robertson, Spandan Miati and Peyman Givi. I need to deeply thank all of you for your incredible mentorship and providing me the opportunity to complete my PhD in the way that I enjoyed. I feel very fortunate that during my PhD I was mostly doing something that I was passionate about; something that I loved to do; and it certainly was not possible without your supports and inspirations. Thanks for being so wonderful!

Big thanks go to all my officemates, and friends at the University of Pittsburgh, especially to Giusy Mazzone, Martina Bukac, Mahdi Mohebbi, Matthew Oborski, Michael Durka, Parthib Rao, Wendy Janocha; and Ellen Smith at Pitt Writing Center. I am very grateful to be collaborating with Ivan Yotov in the Department of Mathematics on this project. Also, my dissertation owes Larry Taber a great debt for his insightful suggestions.

I thank my parents, and my brothers Hamed and Mohammad; for their encouragement every step of the way. I thank Mehdi, for accompanying me on different parts of the journey and for being always a great listener.

This dissertation is sponsored by the fellowship from Computational Modeling & Simulation PhD program, University of Pittsburgh; for which I am very grateful.

R. Zakerzadeh, July 2016

1.0 INTRODUCTION

Poroelastic materials consist of a porous elastic solid phase, filled with fluid. When the poroelastic material deforms, the volume of the pore fluid changes. In this thesis, we consider the problem of interaction between the viscous flow with a deformable poroelastic medium. Such a problem is of a great importance in a wide range of applications. The filtration of fluids through porous media occurs in industrial process involving air or oil filters, in cross-flow filtration procedures, and in geophysical applications such as modeling groundwater flow in fractured poroelastic media through the rocks and sands. Another example of this type of problem is the area of biology. Since all soft tissues consist of water for a large fraction, poroelastic models required to obtain more realistic simulations. Porous media formulation has been used for modeling blood flow in the myocardium tissue [1], study drug transport and lipid (LDL) in the blood vessel walls [2-5], and interstitial fluid in articular cartilage [6] and intervertebral discs [7].

The theory of the poroelastic material has been studied extensively, however only a few studies have included poroelastic material in FSI simulations, see [4, 8] and references therein. This is probably due to an undeniable inherent mathematical difficulty involved in these problems. Theoretical results on existence of the solution for FSI problems can be found only for certain reduced systems. Therefore, computational models play a significant role in this area as they can predict properties of the Fluid- Porous Structure Interaction (FPSI) system; such as

interstitial fluid velocity, that are extremely difficult to validate with experimental evidence or analytical solutions.

One interesting biological application of FPSI problems is the coupling of flow with mass transport. This is a significant potential application, since mass transport provides nourishment, remove wastes, affects pathologies and allows to deliver drugs to arteries [9]. In the context of hemodynamics, considering arterial wall as an elastic structure is a common assumption in Fluid-Structure Interaction (FSI) simulations; but it neglects realistic arterial wall model. In reality, arterial wall like other soft tissues is viscoelastic and it shows poroelastic behavior as well. Both low- and high density lipoproteins (LDL and HDL) can enter the intima from the plasma [10]. The experimental results show the significant increase in the volume of plasma in the intima in hypertension, which supports the idea that the plasma enters intima as a unit [11]. This could occur by leakage through the endothelial cell junctions presumably [12].

Another practical application of FPSI formulation is in modeling the arterial grafts. Using FPSI model is crucial to investigate how the prosthetic graft behaves in different configurations from implantation to matured artery, as well as in estimating the risk of both mechanical mismatch in the initial stages and the eventual rupture. This is motivated by the fact that in animal experiments, many grafts fail inside the body after implantation, especially in larger animals because of the unreliable mechanical properties. Computational models can predict hemodynamics and mechanical stresses by solving fluid structure interaction for graft in in-vivo condition and therefore guide a robust and reliable design of grafts suitable mechanical properties.

Earlier numerical models used to predict blood flow are based on rigid geometries [13] in which only the arterial lumen needs to be reconstructed and discretized, yielding results in a

relatively short time. However, the rigid wall assumption precludes pressure wave propagation and overestimates wall shear stress. In 2006, Hughes et al [14] developed a FSI model capable of coupling incompressible fluids with non-linear elastic solids and allowing for large structural displacements, and applied it to the problems of arterial blood flow. The new approach is evaluated on a patient specific abdominal aorta. This paper proposed that future developments should address the extensions to hyperelastic materials including viscoelasticity, which are capable of representing more physically realistic behavior of the arterial wall. Moreover, recent in vivo studies, have identified viscoelastic arterial wall properties over a cardiac cycle [15]. Although the material properties of arteries have been widely studied [16-19], to our knowledge, only a few constitutive models for the arterial wall have been deeply analyzed in the time dependent domain, when coupled with the pulsation induced by the heartbeat. This is one of our motivations for this research.

We study the effect of using a poroelastic material model in the interaction between the fluid flow and a deformable structure that can represent the arterial wall. To model the free fluid, we consider Navier- Stokes equations, under the assumptions of incompressible and Newtonian rheology. A well-accepted model for characterizing the behavior of a poroelastic material is provided by the Biot equations. The Biot system consists of the governing equations for the deformation of an elastic skeleton, which is completely saturated with fluid. The average velocity of the fluid in the pores is modeled using the Darcy equation, complemented with an additional term that depends on the volumetric deformation of the porous matrix. Indeed, this term accounts for the poroelastic coupling. In this work we focus on the coupling of the Navier-Stokes and Biot models, for phenomena where time and space dependence of the unknowns play a significant role.

The numerical discretization of the problem at hand features several difficulties. Loosely coupled schemes for fluid–structure interaction may turn out to be unconditionally unstable, under a particular range of the physical parameters of the model [20]. This is the so called added-mass effect. An additional difficulty is combining the Eulerian description of the moving fluid domain with the typical Lagrangian parametrization of the structure [21]. Concerning the analysis, the coupled problem and in particular the formulation of appropriate interface conditions has been studied in [22]. Depending on the field of application, different formulations are available to couple a free flow with a saturated poroelastic material. In the context of geosciences, this coupled problem is used to model the interaction of the material with fractures, as in [22-24]. In the context of biomedical applications, FSI studies involving poroelastic materials are scanty. Among the available contributions, we mention [25] and [2].

This dissertation is organized as follows: In Chapter 2.0 , the computational model for the interaction between the viscous fluid and a poroelastic material using Nitsche’s method, with the assumption of having small deformations, is considered. The work presented in this chapter has been presented at APS-DFD [26] and is published in CMAME journal [27] and proceeding of ICBME proceeding [28, 29] . Moreover, the sensitivity analysis have been performed to analyze the effect of poroelasticity on FSI model, published in [8]. In Chapter 3.0 , the energy distribution in the coupled FSI problem for different constitutive models of the wall is discussed. At the end of this chapter I justify the motivation to extend the work to the finite elasticity formulation. The results of this chapter are published in [30]. In Chapter 4.0 , the nonlinear model for FSI is developed to analyze how poroelasticity can affect the energy dissipation in the porous media when it undergoes large deformations. Parts of this chapter has been presented at

APS-DFD [31] and [32]. In Chapter 5.0 , some final remarks are made with some suggestions for future research.

2.0 LINEAR MODEL FOR FPSI

The objective of this chapter is to develop and analyze a loosely coupled numerical solver for the coupled Biot–Stokes system. In this chapter, we consider only fixed domains Ω_f and Ω_p representing the reference (Lagrangian) configuration of the fluid and solid domains, respectively. As a consequence of the fixed domain assumption, the computational model that we propose is suitable in the range of small deformations. This approach is adopted here to simplify the complexity of the fluid–structure–porous interaction and it is a common assumption for fluid–structure interaction problems when we are in the regime of small deformations. Although simplified, this problem still retains the main difficulties associated with the fluid–porous media coupling. We note that in recent work [17] we have also studied the differences between the fixed and the moving domain approaches in small deformation regime. The results, indicate that in this particular case the effect of geometric and convective nonlinearities is negligible.

In numerical modeling there are only a few rigorous contributions to this type of problems. The coupling between a fluid and a single layer poroelastic structure has been previously studied in [4, 33]. In particular, the work in [4] is based on the modeling and a numerical solution of the interaction between an incompressible, Newtonian fluid, described using the Navier Stokes equations, and a poroelastic structure modeled as a Biot system.

We design a time advancing scheme, which allows us to independently solve the governing equations of the system at each time step. Resorting to time splitting approaches mitigates the difficulty to identify appropriate solvers for the coupled system and reduces the need of large memory storage. The main drawback of loosely coupled splitting schemes is possible lack of stability and accuracy. To overcome these natural limitations, we adopt a non-standard approach for the approximation of the coupling conditions, which is inspired by Nitsche's method for the enforcement of boundary conditions, and it consists of adding appropriate interface operators to the variational formulation of the problem. Using time-lagging, the variational coupled problem can be split into three independent subproblems involving the elasticity equation, Darcy equation for flow in porous media and the Stokes problem, respectively. The stability analysis of the resulting scheme shows how to design appropriate stabilization terms that guarantee the stability of the time advancing algorithm. The Nitsche's coupling approach allows for treating the mixed form of Darcy flow and thus provides accurate approximation to the filtration velocity. This is an alternative to the Lie-splitting scheme developed in [31], which is suitable for the pressure formulation of Darcy flow.

This chapter is organized as follows. In Section 2.1 we present the governing equations of the prototype problem at hand, complemented by initial, boundary and interface conditions. The numerical discretization scheme, and in particular the approximation of the interface conditions is presented in Section 2.1.1. Section 2.3 is devoted to the development and analysis of the loosely coupled scheme and discusses the use of the loosely coupled scheme as a preconditioner for the monolithic scheme. Numerical experiments and convergence analysis of the benchmark test are discussed in Section 2.4. The corresponding results support and complement the available theory.

2.1 FORMULATION

We consider the flow of an incompressible, viscous fluid in a channel bounded by a thick poroelastic medium. In particular, we are interested in simulating flow through the deformable channel with a two-way coupling between the fluid and the poroelastic structure. We assume that the channel is sufficiently large so that the non-Newtonian effects can be neglected. The fluid is modeled as an incompressible, viscous, Newtonian fluid using the Navier-Stokes equations in a deformable domain $\Omega_f(t)$:

$$\rho_f \left(\frac{\partial v}{\partial t} + v \cdot \nabla v \right) = \nabla \cdot \sigma_f \quad \text{in } \Omega_f \quad (2.1)$$

$$\nabla \cdot v = 0 \quad \text{in } \Omega_f \quad (2.2)$$

Here v and ρ_f stand for fluid velocity vector field and fluid density, respectively, and $\sigma_f = -p_f I + 2\mu_f D(v)$ is the fluid Cauchy stress tensor where p_f is fluid pressure, μ_f is fluid dynamic viscosity and fluid strain rate tensor is defined as $D(v) = \frac{1}{2}(\nabla v + \nabla v^T)$.

We consider problem configurations as the channel extends to the external boundary, see Figure 1. This configuration is suitable for FSI in arteries. In this case, denote the inlet and outlet fluid boundaries by Γ_f^{in} and Γ_f^{out} , respectively.

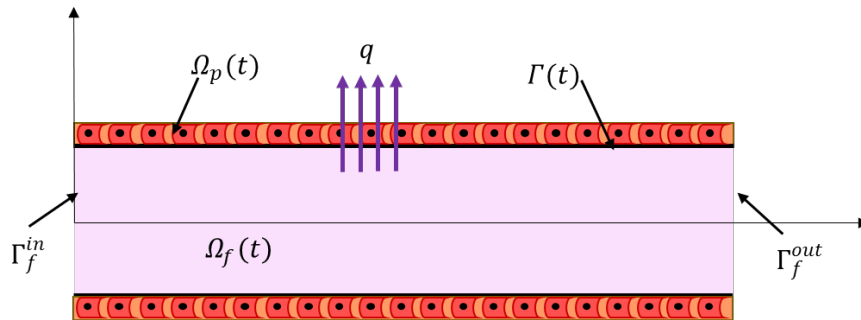


Figure 1. Schematic of the problem configuration

At the inlet and outlet boundary we prescribe the following conditions:

$$\sigma_f n_f = -p_{in}(t)n_f \quad \text{or} \quad v = v_{in}(t) \quad \text{on } \Gamma_f^{in} \times (0, T) \quad (2.3)$$

$$\sigma_f n_f = 0 \quad \text{on } \Gamma_f^{out} \times (0, T) \quad (2.4)$$

where n_f is the outward normal unit vector to the fluid boundaries and $p_{in}(t)$ is the pressure increment with respect to the ambient pressure surrounding the channel. The fluid domain is bounded by a deformable porous matrix consisting of a skeleton and connecting pores filled with fluid, whose dynamics is described by the Biot model. In particular, we consider the problem formulation analyzed in [34] and addressed in [24] for geomechanics.

To model the poroelastic properties of the wall, we use the Biot system [24, 35] that describes the mechanical behavior of a homogeneous and isotropic elastic skeleton, and connecting pores filled with fluid. We assume that the fluid flow through the porous medium is modeled using the Darcy equation. Hence; the Biot system for a poroelastic material consists of the momentum equation for balance of total forces (2.5), Darcy's law (2.6) and the storage equation (2.7) for the fluid mass conservation in the pores of the matrix:

$$\rho_p \frac{\partial^2 U}{\partial t^2} - \nabla \cdot (\sigma^S - \alpha p_p I) = 0 \quad \text{in } \Omega_p \quad (2.5)$$

$$k^{-1} q = -\nabla p_p \quad \text{in } \Omega_p \quad (2.6)$$

$$\frac{\partial}{\partial t} (s_0 p_p + \alpha \nabla \cdot U) + \nabla \cdot q = 0 \quad \text{in } \Omega_p \quad (2.7)$$

In equation (2.6), the relative velocity of the fluid within the porous wall is denoted by q , p_p is the fluid pressure. And hydraulic conductivity of the porous matrix is denoted by k . the coefficient s_0 in (2.7) is the storage coefficient, and the Biot-Willis constant α is the pressure-storage coupling coefficient. σ^S denotes the elasticity stress tensor.

We assume that the poroelastic structure is fixed at the inlet and outlet boundaries:

$$U = 0 \quad \text{on } \Gamma_p^{in} \cup \Gamma_p^{out} \quad (2.8)$$

that the external structure boundary Γ_p^{ext} is exposed to external ambient pressure

$$n_p \cdot \sigma^E n_p = 0 \quad \text{on } \Gamma_p^{ext} \quad (2.9)$$

where n_p is the outward unit normal vector on $\partial\Omega_p$, and that the tangential displacement of the exterior boundary is zero:

$$U \cdot t_p = 0 \quad \text{on } \Gamma_p^{ext} \quad (2.10)$$

where $U \cdot t_p$ denotes the tangential component of the vector U . On the fluid pressure in the porous medium, we impose following boundary conditions:

$$p_p = 0 \quad \text{on } \Gamma_p^{ext}, \quad q \cdot n_p = 0 \quad \text{on } \Gamma_p^{in} \cup \Gamma_p^{out} \quad (2.11)$$

At the initial time, the fluid and the poroelastic structure are assumed to be at rest, with zero displacement from the reference configuration

$$v = 0, \quad U = 0, \quad \frac{\partial U}{\partial t} = 0, \quad p_p = 0. \quad (2.12)$$

The fluid and poroelastic structure are coupled via the following interface conditions, where we denote by n the outward normal to the fluid domain and by t the tangential unit vector on the interface Γ . We assume that n, t coincide with the unit vectors relative to the fluid domain Ω_f . For mass conservation, the continuity of normal flux implies (2.13).

$$\left(v - \frac{\partial U}{\partial t}\right) \cdot n = q \cdot n \quad \text{on } \Gamma \quad (2.13)$$

We point out that the fluid velocity field is allowed to have a non-vanishing component transversal to the interface Γ , namely $v \cdot n$. This velocity component accounts for the small deformations of the fluid domain around the reference configuration Ω_f . We also note that the displacement of the solid domain U doesn't have to be equal to zero on the interface. There are

different options to formulate a condition relative for the tangential velocity field at the interface. A no-slip interface condition is appropriate for those problems where fluid flow in the tangential direction is not allowed,

$$v \cdot t = \frac{\partial U}{\partial t} \cdot t \quad \text{on } \Gamma. \quad (2.14)$$

Concerning the exchange of stresses, the balance of normal components of the stress in the fluid phase gives:

$$n \cdot \sigma_f n = -p_p \quad \text{on } \Gamma. \quad (2.15)$$

The conservation of momentum describes balance of contact forces. Precisely, it says that the sum of contact forces at the fluid-porous medium interface is equal to zero:

$$n \cdot \sigma_f n - n \cdot \sigma_p n = 0 \quad \text{on } \Gamma, \quad (2.16)$$

$$t \cdot \sigma_f n - t \cdot \sigma_p n = 0 \quad \text{on } \Gamma. \quad (2.17)$$

2.1.1 What is the Nitsche's method?

One original feature of the proposed research is to approximate the complex interface conditions between the fluid, the porous medium and the structure mechanics using the Nitsche's method Figure 2. Originally Nitsche's method was designed for imposing essential boundary conditions weakly, at the level of variational formulation, but it can be used for handling internal interface conditions as well [36] and also in the particular case of fluid-structure interaction [37]. A Nitsche's coupling has been proposed in [37, 38] for the interaction of a fluid with an elastic structure. Here, we extend those ideas to the case where a porous media flow is coupled to the fluid and the structure. The advantage of the Nitsche's method is that it provides flexibility of

implementation on unstructured grids. Because there is no need to choose conforming fluid and structure meshes at the interface.

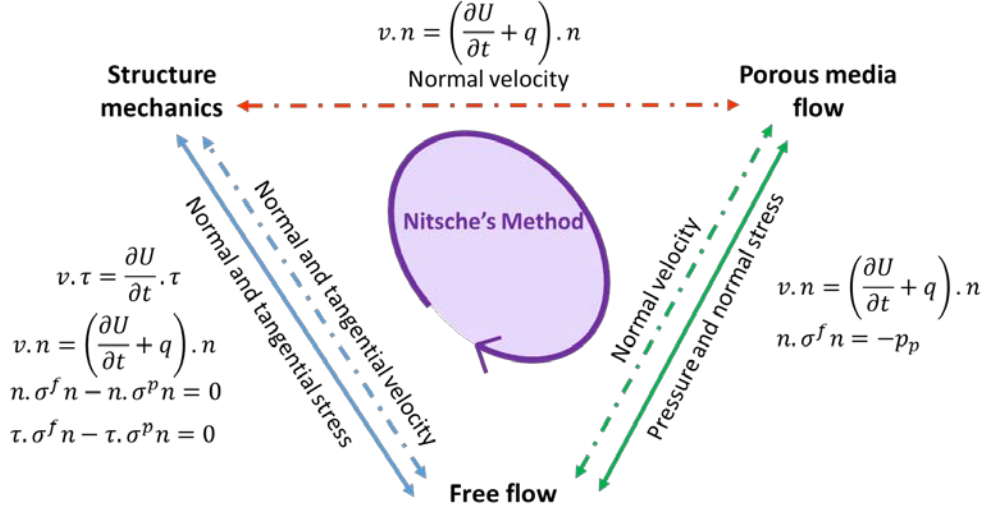


Figure 2. Schematic of the interface conditions in FPSI system

Nitsche's method is utilized in this work to overcome the difficulty of the loosely coupled method in stability and accuracy. In particular, we have selected Nitsche's method for enforcing coupling condition (2.13). Strong enforcement cannot handle (2.13) since it is a multi-variable equation that cannot be enforced into the finite element space directly. In contrast, Nitsche's method can do it since it is a weak enforcement. A simple example of how to apply Nitsche's method is provided using Poisson equation (2.18).

$$-\Delta u = f \text{ in } \Omega \quad \text{and } u = 0 \text{ on } \partial\Omega \quad (2.18)$$

In strong enforcement we define $V_g = \{v \in H^1(\Omega) \mid v = 0 \text{ on } \partial\Omega\}$ and we seek $u \in V_g$ such that $(\nabla u, \nabla v)_\Omega = (f, v)_\Omega \quad \forall v \in V_0$. While, if we want to impose this essential boundary condition weakly, with Nitsche method: we find $U \in V^h \subset H^1(\Omega)$ such that $a(U, v) = (f, v)_\Omega \quad \forall v \in V^h$, and we have:

$$\begin{aligned}
a_h(U, v) = & \int_{\Omega} \nabla U \cdot \nabla v \, dx \\
& - \int_{\partial\Omega} \frac{\partial U}{\partial n} \cdot v \, ds - \int_{\partial\Omega} \frac{\partial v}{\partial n} \cdot U \, ds + \frac{\gamma}{h} \int_{\partial\Omega} U \cdot v \, ds
\end{aligned} \tag{2.19}$$

where γ is a positive constant. The main advantage is that the finite element space and is not affected by the interface conditions.

In [39] a similar problem to what we are addressing here has been solved using Lagrange multiplier. It has been shown that the convergence rates are the same, however the continuity of flux across the interface is enforced in a stronger way with the use of Lagrange multiplier. More precisely, we get pointwise continuity on the interface, while penalization as done in Nitsche leads to a weaker imposition of this interface condition. Nitsche coupling conditions are more loose. The resulting scheme can be split or preconditioned, so in the end we may use iterative solver to solve the system. Lagrange multiplier method does not allow for it, so we have a monolithic scheme which we have to solve using a direct solver.

2.2 WEAK FORMULATION

For the spatial discretization, we exploit the finite element method. Let T_h^f and T_h^p be fixed, quasi-uniform meshes defined on the domains Ω_f and Ω_p . We require that Ω_f and Ω_p are polygonal or polyhedral domains and that they conform at the interface Γ . We also require that the edges of each mesh lay on Γ . We denote with V_h^f, Q_h^f the finite element spaces for the velocity and pressure approximation on the fluid domain Ω_f , with V_h^p, Q_h^p the spaces for velocity and pressure approximation on the porous matrix Ω_p and with X_h^p, \dot{X}_h^p the approximation spaces

for the structure displacement and velocity, respectively. We assume that all the finite element approximation spaces comply with the prescribed Dirichlet conditions on external boundaries $\partial\Omega_f, \partial\Omega_p$. The bilinear forms relative to the structure, are defined as:

$$\begin{aligned} a_s(U_h, \varphi_{p,h}) &:= 2\mu_p \int_{\Omega_p} D(U_h):D(\varphi_{p,h})dx + \lambda_p \int_{\Omega_p} (\nabla \cdot U_h)(\nabla \cdot \varphi_{p,h})dx, \\ b_s(p_{p,h}, \varphi_{p,h}) &:= \alpha \int_{\Omega_p} p_{p,h} \nabla \cdot \varphi_{p,h} dx. \end{aligned} \tag{2.20}$$

For the fluid flow, and the filtration through the porous matrix, the bilinear forms are:

$$\begin{aligned} a_f(v_h, \varphi_{f,h}) &:= 2\mu_f \int_{\Omega_f} D(v_h):D(\varphi_{f,h})dx, \\ a_p(q_h, r_h) &:= \int_{\Omega_p} \kappa^{-1} q_h \cdot r_h dx, \\ b_f(p_{f,h}, \varphi_{f,h}) &:= \int_{\Omega_f} p_{f,h} \nabla \cdot \varphi_{f,h} dx, \\ b_p(p_{p,h}, r_h) &:= \int_{\Omega_p} p_{p,h} \nabla \cdot r_h dx \end{aligned} \tag{2.21}$$

After integrating by parts the governing equations, in order to distribute over test functions the second spatial derivatives of velocities and displacements as well as the first derivatives of the pressure, resorting to the *dual-mixed* weak formulation of Darcy's problem, the following interface terms appear in the variational equations,

$$I_\Gamma = \int_\Gamma (\sigma_{f,h} n \cdot \varphi_{f,h} - \sigma_{p,h} n \cdot \varphi_{p,h} + p_{p,h} r_h \cdot n) \tag{2.22}$$

Starting from the expression of I_Γ , Nitsche's method allows us to weakly enforce the interface conditions. More precisely, we separate I_Γ into the normal and tangential components with respect to Γ and we use balance of stress over the interface, namely (2.15), (2.16), (2.17) to substitute the components of $\sigma_{f,h}$ into $\sigma_{p,h}$ and $p_{p,h}$.

As a result, I_Γ can be rewritten as,

$$I_\Gamma = \int_\Gamma n \cdot \sigma_{f,h}(v_h, p_{f,h}) n (\varphi_{f,h} - r_h - \varphi_{p,h}) \cdot n + \int_\Gamma t \cdot \sigma_{f,h}(v_h, p_{f,h}) n (\varphi_{f,h} - \varphi_{p,h}) \cdot t.$$

Since the expression of the interface terms involves the stresses only on the fluid side, this formulation can be classified as a *one-sided* variant of Nitsche's method for interface conditions. We refer to [36] for an overview of different formulations. The enforcement of the kinematic conditions (2.13) and (2.14) using Nitsche's method is based on adding to the variational formulation of the problem appropriate penalty terms. This results in the transformed integral,

$$\begin{aligned} -I_\Gamma^*(v_h, q_h, p_{f,h}, p_{p,h}, U_h; \varphi_{f,h}, r_h, \psi_{f,h}, \psi_{p,h}, \varphi_{p,h}) = \\ - \int_\Gamma n \cdot \sigma_{f,h}(v_h, p_{f,h}) n (\varphi_{f,h} - r_h - \varphi_{p,h}) \cdot n - \int_\Gamma t \cdot \sigma_{f,h}(v_h, p_{f,h}) n (\varphi_{f,h} - \varphi_{p,h}) \cdot t \\ + \int_\Gamma \gamma_f \mu_f h^{-1} [(v_h - q_h - \partial_t U_h) \cdot n (\varphi_{f,h} - r_h - \varphi_{p,h}) \cdot n + (v_h - \partial_t U_h) \cdot t (\varphi_{f,h} - \varphi_{p,h}) \cdot t], \end{aligned}$$

where $\gamma_f > 0$ denotes a penalty parameter that will be suitably defined later on.

Furthermore, in order to account for the symmetric, incomplete or skew-symmetric variants of Nitsche's method, see [36], we introduce the following additional terms:

$$\begin{aligned} -S_\Gamma^{*,\zeta}(v_h, q_h, p_{f,h}, p_{p,h}, U_h; \varphi_{f,h}, r_h, \psi_{f,h}, \psi_{p,h}, \varphi_{p,h}) = \\ - \int_\Gamma n \cdot \sigma_{f,h}(\zeta \varphi_{f,h}, -\psi_{f,h}) n (v_h - q_h - \partial_t U_h) \cdot n - \int_\Gamma t \cdot \sigma_{f,h}(\zeta \varphi_{f,h}, -\psi_{f,h}) n (v_h - \partial_t U_h) \cdot t, \end{aligned}$$

which anyway do not violate the consistency of the original scheme because they vanish if the kinematic constraints are satisfied. The flag $\zeta \in (1, 0, -1)$ determines if we adopt a symmetric, incomplete or skew symmetric formulation, respectively.

For any $t \in (0, T)$, the coupled fluid/solid problem consists of finding $v_h, p_{f,h}, q_h, p_{p,h} \in V_h^f \times Q_h^f \times V_h^p \times Q_h^p$ and $U_h, \dot{U}_h \in X_h^p \times \dot{X}_h^p$ such that for any $\varphi_{f,h}, \psi_{f,h}, r_h, \psi_{p,h} \in V_h^f \times Q_h^f \times V_h^p \times Q_h^p$ and $\varphi_{p,h}, \dot{\varphi}_{p,h} \in X_h^p \times \dot{X}_h^p$ we have,

$$\begin{aligned}
& \rho_p \int_{\Omega_p} \partial_t \dot{U}_h \cdot \varphi_{p,h} dx + \rho_p \int_{\Omega_p} (\dot{U}_h - \partial_t U_h) \cdot \dot{\varphi}_{p,h} dx \\
& + \rho_f \int_{\Omega_f} \partial_t v_h \cdot \varphi_{f,h} dx + s_0 \int_{\Omega_p} \partial_t p_{p,h} \psi_{p,h} dx + a_s(U_h, \varphi_{p,h}) \\
& - b_s(p_{p,h}, \varphi_{p,h}) + b_s(\psi_{p,h}, \partial_t U_h) + a_p(q_h, r_h) - b_p(p_{p,h}, r_h) \quad (2.23) \\
& + b_p(\psi_{p,h}, q_h) + a_f(v_h, \varphi_{f,h}) - b_f(p_{f,h}, \varphi_{f,h}) + b_f(\psi_{f,h}, v_h) \\
& - (I_\Gamma^* + S_\Gamma^{*\zeta})(v_h, q_h, p_{f,h}, p_{p,h}, U_h; \varphi_{f,h}, r_h, \psi_{f,h}, \psi_{p,h}, \varphi_{p,h}) \\
& = F(t; \varphi_{f,h}, r_h, \psi_{f,h}, \psi_{p,h}, \varphi_{p,h}).
\end{aligned}$$

Problem (2.23) is usually called the semi-discrete problem (SDP). Equation (2.23) must be complemented by suitable initial conditions and $F(\cdot)$ accounts for boundary conditions and forcing terms. We set $p_{in} \neq 0$ or $v_{in} \neq 0$ on Γ_f^{in} . The corresponding forcing term is:

$$F(t; \varphi_{f,h}) = - \int_{\Gamma_f^{in}} p_{in}(t) \varphi_{f,h} \cdot n_f$$

We now address the time discretization. Let Δt denote the time step, $t_n = n\Delta t$, $0 \leq n \leq N$. For the time discretization of the coupled problem, we have adopted the Backward Euler (BE) method for both the flow and the structure problem. We define the first order (backward) discrete time derivative be defined as:

$$d_\tau u^n := \frac{u^n - u^{n-1}}{\Delta t}.$$

The fully discrete coupled fluid-solid problem is to find, at each t_n , $v_h^n, p_{f,h}^n, q_h^n, p_{p,h}^n \in V_h^f \times Q_h^f \times V_h^p \times Q_h^p$ and $U_h^n, \dot{U}_h^n \in X_h^p \times \dot{X}_h^p$ such that for any $\varphi_{f,h}, \psi_{f,h}, r_h, \psi_{p,h} \in V_h^f \times Q_h^f \times V_h^p \times Q_h^p$ and $\varphi_{p,h}, \dot{\varphi}_{p,h} \in X_h^p \times \dot{X}_h^p$ we have,

$$\begin{aligned}
& \rho_p \int_{\Omega_p} d_\tau \dot{U}_h^n \cdot \varphi_{p,h} dx + \rho_p \int_{\Omega_p} (\dot{U}_h^n - d_\tau U_h^n) \cdot \dot{\varphi}_{p,h} dx \\
& + \rho_f \int_{\Omega_f} d_\tau v_h^n \cdot \varphi_{f,h} dx + s_0 \int_{\Omega_p} d_\tau p_{p,h}^n \psi_{p,h} dx + a_s(U_h^n, \varphi_{p,h}) \\
& - b_s(p_{p,h}^n, \varphi_{p,h}) + b_s(\psi_{p,h}, d_\tau U_h^n) + a_p(q_h^n, r_h) - b_p(p_{p,h}^n, r_h) \\
& + b_p(\psi_{p,h}, q_h^n) + a_f(v_h^n, \varphi_{f,h}) - b_f(p_{f,h}^n, \varphi_{f,h}) + b_f(\psi_{f,h}, v_h^n) \\
& - (I_\Gamma^* + S_\Gamma^{*\zeta})(v_h^n, q_h^n, p_{f,h}^n, p_{p,h}^n, U_h^n; \varphi_{f,h}, r_h, \psi_{f,h}, \psi_{p,h}, \varphi_{p,h}) \\
& = F(t_n; \varphi_{f,h}).
\end{aligned} \tag{2.24}$$

We denote problem (2.24) as the (fully) discrete problem with implicit coupling between the fluid and the structure sub-problems.

2.3 NUMERICAL PROCEDURE

The challenges of numerical discretization of the FSI problem in hemodynamics are associated with the added-mass effect and high nonlinearity of the problem. In case of poroelasticity an additional difficulty is with the fluid-porous media coupling. Also these kinds of problems have high computational costs since there are more unknowns; and also more equations are coupled. So we may have memory problems as well. It motivates our numerical work.

The numerical approaches in solving FSI problems are classified into the partitioned and the monolithic approach. Partitioned approach treats the fluid and structure problems as two

computational fields, which can be solved using two distinct solvers. The interface conditions between the fluid and structure are solved through loosely or strongly coupled algorithms. Monolithic approach treats the fluid and the structure as a single system and the interfacial conditions are implicit in the solution procedure.

We have addressed both approaches for solving this problem. Indeed, it is expensive to solve this complex system by using the traditional monolithic methods even though they are usually stable and accurate. Hence, it is important to develop new methods to solve it in decoupled ways. Since splitting of the problem degrades the approximation properties, we first propose a loosely coupled method and then we suggest that the loosely coupled scheme serve as a preconditioner for the global monolithic solution approach. At the best of our knowledge, it is the first time that this approach is adopted for fluid porous structure interaction problems.

2.3.1 Partitioned scheme

When enforced by Nitsche's method, the interface conditions appear in the variational formulation in a *modular* form. As a result, using time lagging, it is straightforward to design various loosely coupled algorithms to solve each equation of the problem independently from the others. If we finally proceed to solve all the problems independently, we obtain the explicit algorithm reported below. We also formulate explicitly the governing and interface conditions that are enforced in practice when each sub-problem is solved. The stability analysis is provide in [27].

Sub-problem 1: given $v_h^{n-1}, p_{f,h}^{n-1}, q_h^{n-1}, p_{p,h}^{n-1}$ find U_h^n, \dot{U}_h^n in Ω_p such that:

$$\begin{aligned}
& \rho_p \int_{\Omega_p} d_\tau \dot{U}_h^n \cdot \varphi_{p,h} + \rho_p \int_{\Omega_p} (\dot{U}_h^n - d_\tau U_h^n) \cdot \dot{\varphi}_{p,h} + a_s(U_h^n, \varphi_{p,h}) + \int_\Gamma \gamma_f \mu_f h^{-1} d_\tau U_h^n \cdot t_p \varphi_{p,h} \\
& \quad \cdot t_p + \int_\Gamma \gamma_f \mu_f h^{-1} d_\tau U_h^n \cdot n_p \varphi_{p,h} \cdot n_p \\
& = b_s(p_{p,h}^{n-1}, \varphi_{p,h}) - \int_\Gamma n_p \cdot \sigma_{f,h}^{n-1} n_p (-\varphi_{p,h}) \cdot n_p - \int_\Gamma t_p \cdot \sigma_{f,h}^{n-1} n_p (-\varphi_{p,h}) \cdot t_p \\
& \quad + \int_\Gamma \gamma_f \mu_f h^{-1} v_h^{n-1} \cdot t_p \varphi_{p,h} \cdot t_p + \int_\Gamma \gamma_f \mu_f h^{-1} (v_h^{n-1} - q_h^{n-1}) \cdot n_p \varphi_{p,h} \cdot n_p.
\end{aligned}$$

This problem is equivalent to solving the elastodynamics equation, namely (2.5), where the pressure term has been time-lagged, complemented with the following Robin-type boundary condition on Γ :

$$n_p \cdot \sigma_p^n n_p = n_p \cdot (\sigma_f)^{n-1} n_p - \gamma_f \mu_f h^{-1} (d_\tau U^n - v^{n-1} + q^{n-1}) \cdot n_p, \text{ on } \Gamma,$$

$$t_p \cdot \sigma_p^n n_p = t_p \cdot (\sigma_f)^{n-1} n_p - \gamma_f \mu_f h^{-1} (d_\tau U^n - v^{n-1}) \cdot t_p, \text{ on } \Gamma.$$

Also the terms involving stress in the fluid are evaluated at the previous time step, to improve the stability of the explicit coupling.

Sub-problem 2: given $v_h^{n-1}, p_{f,h}^{n-1}$ and U_h^n , find $q_h, p_{p,h}^n$ in Ω_p such that:

$$\begin{aligned}
& s_0 \int_{\Omega_p} d_\tau p_{p,h}^n \psi_{p,h} dx + a_p(q_h^n, r_h) - b_p(p_{p,h}^n, r_h) + b_p(\psi_{p,h}, q_h^n) \\
& \quad + s_{f,q} (d_\tau q_h \cdot n_p, r_h \cdot n_p) + \int_\Gamma \gamma_f \mu_f h^{-1} q_h^n \cdot n_p r_h \cdot n_p \\
& = -b_s(\psi_{p,h}, d_\tau U_h^n) + \int_\Gamma \gamma_f \mu_f h^{-1} (v_h^{n-1} - d_\tau U_h^{n-1}) \cdot n_p r_h \cdot n_p \\
& \quad + \int_\Gamma n_p \cdot \sigma_{f,h}^{n-1} n_p r_h \cdot n_p.
\end{aligned}$$

This problem consists of the dual-mixed weak form of Darcy equations (2.6)-(2.7) complemented with the following boundary condition,

$$p_p^n = -n_p \cdot (\sigma_f)^{n-1} n_p - \gamma_f \mu_f h^{-1} (v^{n-1} - d_\tau U^{n-1} - q_h^n) \cdot n_p, \quad \text{on } \Gamma.$$

Sub-problem 3: given $q_h^n, p_{f,h}^n, U_h^n$, find $v_h^n, p_{f,h}^n$ in Ω_f such that:

$$\begin{aligned} & \rho_f \int_{\Omega_f} d_\tau v_h^n \cdot \varphi_{f,h} dx + a_f(v_h^n, \varphi_{f,h}) - b_f(p_{f,h}^n, \varphi_{f,h}) + b_f(\psi_{f,h}, v_h^n) \\ & + s_{f,p}(d_\tau p_{f,h}, \psi_{f,h}) + s_{f,v}(d_\tau v_h^n \cdot n_f, \varphi_{f,h} \cdot n_f) \\ & - \int_\Gamma \sigma_{f,h}(\zeta \varphi_{f,h}, -\psi_{f,h}) n_f \cdot v_h^n + \int_\Gamma \gamma_f \mu_f h^{-1} v_h^n \cdot \varphi_{f,h} \\ & = F(t_n; \varphi_{f,h}) + \int_\Gamma \sigma_{f,h}^{n-1} n_f \cdot \varphi_{f,h} - \int_\Gamma t_f \cdot \sigma_{f,h}(\zeta \varphi_{f,h}, -\psi_{f,h}) n_f d_\tau U_h^n \cdot t_f \\ & - \int_\Gamma n_f \cdot \sigma_{f,h}(\zeta \varphi_{f,h}, -\psi_{f,h}) n_f (q_h^n + d_\tau U_h^n) \cdot n_f + \int_\Gamma \gamma_f \mu_f h^{-1} (q_h^n \\ & + d_\tau U_h^n) \cdot n_f \varphi_{f,h} \cdot n_f + \int_\Gamma \gamma_f \mu_f h^{-1} d_\tau U_h^n \cdot t_f \varphi_{f,h} \cdot t_f. \end{aligned}$$

where $s_{f,p}(d_\tau p_{f,h}, \psi_{f,h})$ is a stabilization term proposed in [37] acting on the free fluid pressure, that helps to restore the stability of the explicit time advancing scheme.

$$s_{f,p}(d_\tau p_{f,h}, \psi_{f,h}) := \gamma_{stab} \frac{h \Delta t}{\gamma_f \mu_f} \int_\Gamma d_\tau p_{f,h}^n \psi_{f,h}.$$

Before time-lagging of the term $\sigma_{f,h}^{n-1} n_f \cdot \varphi_{f,h}$, this problem corresponds to the fluid equations (2.1)-(2.2), where the kinematic conditions (2.25), have been enforced using the classical Nitsche's method formulation for boundary conditions [36].

$$v^n \cdot n_f = (q^n + d_\tau U^n) \cdot n_f, \quad v^n \cdot t_f = d_\tau U^n \cdot t_f \quad \text{on } \Gamma, \quad (2.25)$$

We observe that new stabilization terms $S_{f,v}, S_{f,q}$ have been introduced into the problem formulation. Their role is to control the increment of v_h^n, q_h^n over two subsequent time steps, namely:

$$S_{f,q}(d_\tau q_h^n \cdot n, r_h \cdot n) = \gamma'_{stab} \gamma_f \mu_f \frac{\Delta t}{h} \int_\Gamma d_\tau q_h^n \cdot n r_h \cdot n,$$

$$S_{f,v}(d_\tau v_h^n \cdot n, \varphi_{f,h} \cdot n) = \gamma'_{stab} \gamma_f \mu_f \frac{\Delta t}{h} \int_\Gamma d_\tau v_h^n \cdot n \varphi_{f,h} \cdot n.$$

2.3.2 Monolithic scheme

The main drawback of loosely coupled methods, in spite of their significant advantage in terms of computational efficiency compare to the monolithic scheme, is poor accuracy. So, to improve the accuracy of our solver, we also consider its application as a preconditioner for the solution of the fully coupled (monolithic) FSI problem formulation.

$$\begin{bmatrix} (M_f + A_f + \Gamma_f^\gamma + \Gamma_f^\sigma + \mathfrak{s}(\Gamma_f^\sigma)^T) & (B_{pf} + \Gamma_{pf})^T & \Gamma_{qf}^T & 0 & \Gamma_{sf}^T & 0 \\ (B_{pf} + \Gamma_{pf}) & S_p & \Gamma_{qp}^T & 0 & \Gamma_{sp}^T & 0 \\ \Gamma_{qf} & \Gamma_{qp} & (A_q + \Gamma_q) & -B_{pq}^T & \Gamma_{sq}^T & 0 \\ 0 & 0 & B_{pq} & M_p & B_{sf}^T & 0 \\ \Gamma_{sf} & \Gamma_{sp} & \Gamma_{sq} & B_{sp} & (A_s + \Gamma_s) & M_s \\ 0 & 0 & 0 & 0 & -M_s & M_s \end{bmatrix} \begin{bmatrix} v^n \\ P_f^n \\ q^n \\ P_p^n \\ U^n \\ U^n \end{bmatrix} = \begin{bmatrix} F(t_n) \\ 0 \\ 0 \\ 0 \\ 0 \\ 0 \end{bmatrix} + \begin{bmatrix} (M_f + S_f) & 0 & 0 & 0 & \Gamma_{sf}^T & 0 \\ 0 & S_p & 0 & 0 & \Gamma_{sp}^T & 0 \\ 0 & 0 & S_q & 0 & \Gamma_{sq}^T & 0 \\ 0 & 0 & 0 & M_p & B_{sp}^T & 0 \\ 0 & 0 & 0 & 0 & \Gamma_s & M_s \\ 0 & 0 & 0 & 0 & -M_s & 0 \end{bmatrix} \begin{bmatrix} v^{n-1} \\ P_f^{n-1} \\ q^{n-1} \\ P_p^{n-1} \\ U^{n-1} \\ U^{n-1} \end{bmatrix} \quad (2.26)$$

In this way, we blend the computational efficiency of the loosely couples scheme with the accuracy of the monolithic ones. The block structure of the algebraic monolithic problem is illustrated (2.26).

The loosely coupled scheme is equivalent to the following upper block triangular system (2.27) according to the fact that each sub-problem can be solved independently, but to insure stability they must be addressed in a precise order,

$$\begin{bmatrix} (M_f + A_f + \Gamma_f^v + S_f + \mathfrak{s}(\Gamma_f^\sigma)^T) & (-B_{pf})^T & \Gamma_{qf}^T & 0 & \Gamma_{sf}^T & 0 \\ (B_{pf} + \Gamma_{pf}) & S_p & \Gamma_{qp}^T & 0 & \Gamma_{sp}^T & 0 \\ 0 & 0 & (A_q + \Gamma_q + S_q) & -B_{pq}^T & \Gamma_{sq}^T & 0 \\ 0 & 0 & B_{pq} & M_p & B_{sf}^T & 0 \\ 0 & 0 & 0 & 0 & (A_s + \Gamma_s) & M_s \\ 0 & 0 & 0 & 0 & -M_s & M_s \end{bmatrix} \begin{bmatrix} v^n \\ P_f^n \\ q^n \\ P_p^n \\ U^n \\ U^n \end{bmatrix} = \begin{bmatrix} F(t_n) \\ 0 \\ 0 \\ 0 \\ 0 \\ 0 \end{bmatrix} + \begin{bmatrix} (M_f + S_f) & \Gamma_{pf}^T & 0 & 0 & \Gamma_{sf}^T & 0 \\ 0 & S_p & 0 & 0 & \Gamma_{sp}^T & 0 \\ \Gamma_{qf} & \Gamma_{qp} & S_q & 0 & \Gamma_{sq}^T & 0 \\ 0 & 0 & 0 & M_p & B_{sp}^T & 0 \\ \Gamma_{sf} & \Gamma_{sp} & \Gamma_{sq} & B_{sp} & \Gamma_s & M_s \\ 0 & 0 & 0 & 0 & -M_s & 0 \end{bmatrix} \begin{bmatrix} v^{n-1} \\ P_f^{n-1} \\ q^{n-1} \\ P_p^{n-1} \\ U^{n-1} \\ U^{n-1} \end{bmatrix} \quad (2.27)$$

Now if we consider A as FSI monolithic system matrix from equation (2.26) and P as FSI partitioned system matrix from (2.27), we can use P as a preconditioner for solving system of equations in (2.26) as following:

$$A.X = b \quad \rightarrow \quad P^{-1}.A.X = P^{-1}.b$$

Where:

$$\begin{aligned}
 &P \\
 = &\begin{bmatrix} (M_f + A_f + \Gamma_f^y + S_f + {}^s(\Gamma_f^\sigma)^T) & (-B_{pf})^T & \Gamma_{qf}^T & 0 & \Gamma_{sf}^T & 0 \\ (B_{pf} + \Gamma_{pf}) & S_p & \Gamma_{qp}^T & 0 & \Gamma_{sp}^T & 0 \\ 0 & 0 & (A_q + \Gamma_q + S_q) & -B_{pq}^T & \Gamma_{sq}^T & 0 \\ 0 & 0 & B_{pq} & M_p & B_{sf}^T & 0 \\ 0 & 0 & 0 & 0 & (A_s + \Gamma_s) & M_s \\ 0 & 0 & 0 & 0 & -M_s & M_s \end{bmatrix} \quad (2.28)
 \end{aligned}$$

A

$$\begin{aligned}
 = &\begin{bmatrix} (M_f + A_f + \Gamma_f^y + \Gamma_f^\sigma + {}^s(\Gamma_f^\sigma)^T) & (B_{pf} + \Gamma_{pf})^T & \Gamma_{qf}^T & 0 & \Gamma_{sf}^T & 0 \\ (B_{pf} + \Gamma_{pf}) & S_p & \Gamma_{qp}^T & 0 & \Gamma_{sp}^T & 0 \\ \Gamma_{qf} & \Gamma_{qp} & (A_q + \Gamma_q) & -B_{pq}^T & \Gamma_{sq}^T & 0 \\ 0 & 0 & B_{pq} & M_p & B_{sf}^T & 0 \\ \Gamma_{sf} & \Gamma_{sp} & \Gamma_{sq} & B_{sp} & (A_s + \Gamma_s) & M_s \\ 0 & 0 & 0 & 0 & -M_s & M_s \end{bmatrix} \quad (2.29)
 \end{aligned}$$

The preconditioner divides the problem into 3 sub-problems that can be solved with backward substitution:

$$\begin{bmatrix} FF & FM & FS \\ 0 & MM & MS \\ 0 & 0 & SS \end{bmatrix} \cdot \begin{bmatrix} x_f \\ x_m \\ x_s \end{bmatrix} = \begin{bmatrix} b_f \\ b_m \\ b_s \end{bmatrix} \quad (2.30)$$

$$\text{Step 1} \quad b_s = SS/x_s$$

$$\text{Step 2} \quad b_m = MM * x_m + MS * x_s \quad \rightarrow \quad x_m = (b_m - MS * x_s)/MM$$

$$\text{Step 3} \quad b_f = FF * x_f + FM * x_m + FS * x_s \quad \rightarrow \quad x_f = (b_f - FM * x_m + FS * x_s)/FF$$

2.4 NUMERICAL SIMULATIONS

In this section we present some numerical results with the aim of testing the methodologies proposed in previous section. All simulations are obtained using a fixed mesh algorithm and movement of the fluid domain is not taken into account; but we have performed some additional simulations using a deformable fluid computational domain and the physiological parameters of Table 1. The results (published in [40]), confirm that for the considered test case the deformation of the computational mesh do not play a significant role on the calculated blood flow rate and the arterial wall displacement.

The approximation space for the fluid flow is based on P2-P1 approximations for velocity and pressure respectively that ensures inf-sup stability of the scheme and the same finite element spaces are used for intramural filtration velocity and pressure in the poroelastic wall. We also use P2 finite elements for the discretization of the structure displacement. Time discretization is performed using backward Euler scheme and the time step is 1.e-4 second. Also, we have used the following values: $\gamma_f = 2500$, $\gamma_{stab} = 1$, $\gamma'_{stab} = 0$.

All the numerical computations have been performed using the Finite Element code Freefem++ [41]. For Fluid-Structure Interaction problem in poroelastic media, the solution of equations for general parameters and problem configuration needs advanced computational tools and can hardly be handled by commercial packages. So, we tested different language environment (FEniCS, FreeFem++) and finally we chose FreeFem++ because it has less complication in writing variational formulations and also it is flexible for enforcing interface conditions thanks to automatic interpolation from a mesh to another one. We use this interpolation is for transferring data between fluid and structure grids.

2.4.1 FSI analysis of pulsatile flow in a compliant channel

We consider a classical benchmark problem used for FSI problems problem that has been used in several works [37, 42]. We adopt a geometrical model that consists of a 2D poroelastic structure superposed to a 2D fluid channel. The model represents a straight vessel of radius 0.5 cm, length 6 cm, and the surrounding structure has a thickness of 0.1 cm. This numerical experiment consists in studying the propagation of a single pressure wave with amplitude comparable to the pressure difference between systolic and diastolic phases of a heartbeat.

$$P_{in}(t) = \begin{cases} \frac{p_{max}}{2} \left(1 - \cos\left(\frac{2\pi t}{T_{max}}\right) \right) & \text{if } t \leq T_{max} , \\ 0 & \text{if } t > T_{max} \end{cases} \quad (2.31)$$

Table 1. Fluid and structure parameters

Symbol	Unit	Values
ρ_p	g/cm ³	1.1
λ_p	dyne/cm ²	4.28×10 ⁶
μ_p	dyne/cm ²	1.07×10 ⁶
α	mmHg	1
μ_f	poise	0.035
ρ_f	g/cm ³	1.1
s_0	cm ² /dyne	5×10 ⁻⁶
κ	cm ³ s/g	5×10 ⁻⁹
ξ	dyne / cm ⁴	5×10 ⁷

At the outlet of the channel, we prescribe the stress free boundary condition, and at the inlet pressure boundary condition is applied. The fluid structure interaction in this benchmark problem is excited by a time-dependent pressure function based on (2.31), prescribed at the inflow of the channel, where $p_{\max}= 13334 \text{ dyne/cm}^2$ and $T_{\max}= 0.003\text{s}$; and the propagation of the pressure wave is analyzed over the time interval $[0, 0.006] \text{ s}$.

we also slightly modify the governing equation for elastic skeleton as (2.32), the additional term ξU comes from the axially symmetric formulation, accounting for the recoil due to the circumferential strain. Namely, it acts like a spring term, keeping the top and bottom structure displacements connected in 2D, see,e.g., [33].

$$\rho_p \frac{\partial^2 U}{\partial t^2} + \xi U - \nabla \cdot \sigma_p = 0 \quad (2.32)$$

The physical parameters used in this study fall within the range of physiological values for blood flow and are reported in Table 1. The propagation of the pressure wave is analyzed over the time interval $[0,0.006] \text{ s}$. The final time is selected such that the pressure wave barely reaches the outflow section. In this way, the non-physical reflected waves that will originate at the outflow section for longer simulation times do not pollute the considered results.

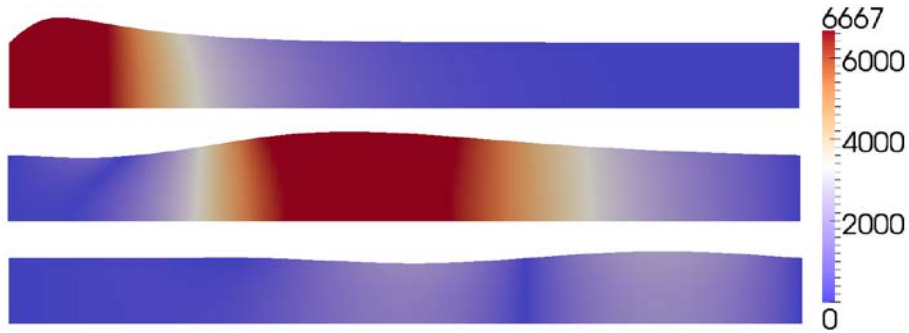


Figure 3. Result for pressure in fluid and displacement in structure

Some visualizations of the solution, calculated using the settings addressed below, are reported in Figure 3, and Figure 4. The former, qualitatively shows the propagation of a pressure wave along the channel, together with the corresponding deformation of the fluid domain at times $t_1 = 1.5$, $t_2 = 3.5$, $t_3 = 5.5$ ms. For visualization purposes, the vertical displacement is magnified 100 times in Figure 3. In Figure 4, top panel, we show the vertical displacement of the interface along the longitudinal axis of the channel. These plots show that the variable inflow pressure combined with the fluid-structure interaction mechanisms, generates a wave in the structure that propagates from left to right.

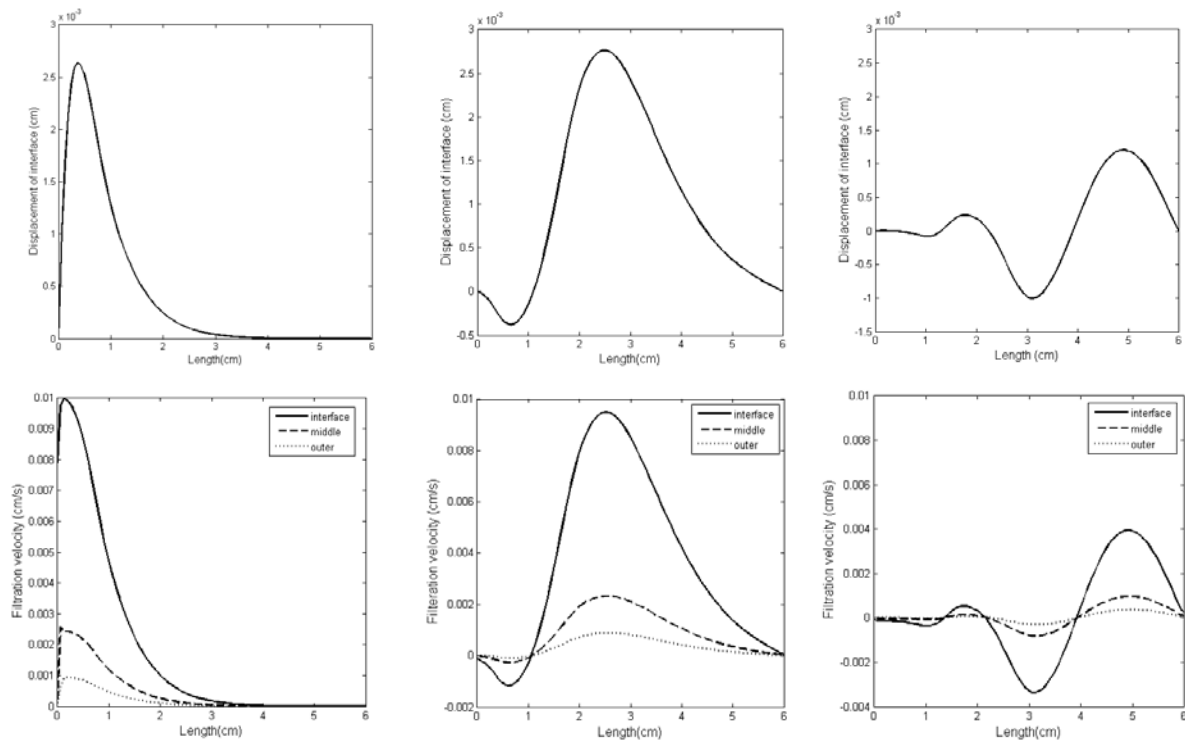


Figure 4. Top panel: displacement of the fluid-structure interface at times 1.5, 3.5 and 5.5 ms from left to right.

Bottom panel: intramural flow $q.n$ at different planes in the arterial wall, located at the interface, at the intermediate section and at the outer layer

On the bottom panel, we show intramural flow $q_h \cdot n$ at different planes cutting the arterial wall in the longitudinal direction. These planes are located at the interface, at the intermediate section and at the outer layer. These plots show that the peaks of the intramural flow coincide with the ones of structure displacement and the corresponding peak of arterial pressure. Furthermore, we notice that the intramural velocity, $q_h \cdot n$, decreases as far as the fluid penetrates further into the wall. This is a consequence of (2.7), which prescribes that $\nabla \cdot q_h$ is not locally preserved, but depends on the rate of change in pressure and volumetric deformation of the structure. Indeed, this is how the poroelastic coupling shows up in the results.

Moreover, the extension to the 3d model is performed in two different geometries: (1) A straight vessel of radius 0.5 cm and length 5 cm, the surrounding structure has a thickness of 0.1 cm; (2) A curved vessel of radius 1.5 cm, the surrounding structure has a thickness of 0.3 cm. The fluid structure interaction in this benchmark problem is excited by pressure profile (2.31), prescribed at the inflow of the channel and the propagation of the pressure wave is analyzed over the time interval $[0, 0.02]$ s.

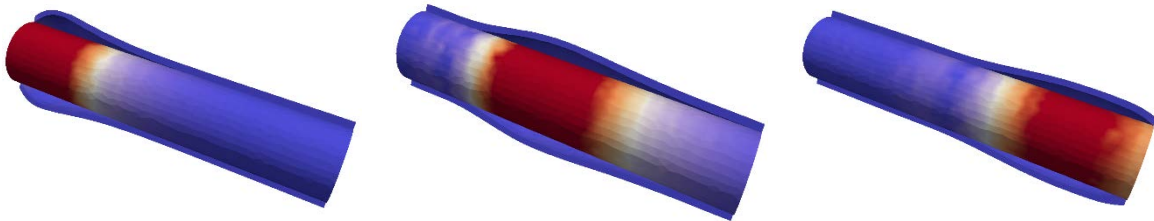


Figure 5. Snapshots of the pressure and solid deformation at 2ms, 4ms, and 6ms from left to right for straight cylinder

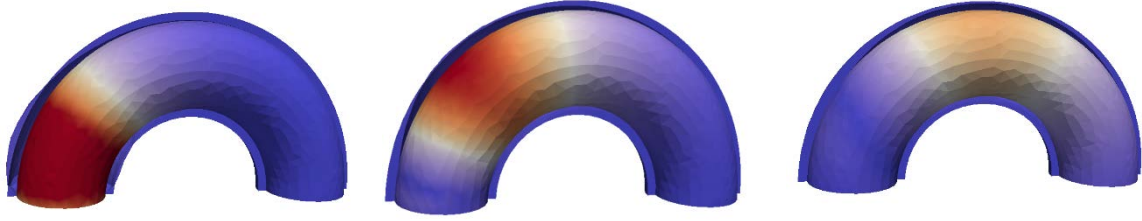


Figure 6. Snapshots of the pressure and solid deformation at 2ms, 4ms, and 6ms from left to right for curved vessel

Figure 5 and Figure 6 show the fluid pressure and solid deformation at the time instants $t = 0.002, 0.004, 0.006$ s. For visualization purpose, the vertical displacement is magnified 100 times. As expected, stable pressure wave propagation along the channel is observed in both problem configurations. We observe that the variable inflow pressure combined with the fluid-structure interaction mechanism generate a wave in the structure that propagates from left to right.

2.4.2 Performance analysis of loosely coupled scheme as a preconditioner

In order to simplify the management of the algebraic degrees of freedom related to the finite element spaces, for this test case we adopt a *PI-PI* approximations for velocity and pressure respectively. It is well known that this choice does not satisfy the inf-sup stability condition [43]. Resorting to a pressure stabilization method on the whole fluid domain is mandatory. Owing to its simplicity of implementation, we opt for the Brezzi-Pitkaranta scheme [44], that is:

$$s_{f,p}(p_{f,h}^n, \psi_{f,h}) := \gamma_p h^2 \int_{\Omega_f} \nabla p_{f,h}^n \cdot \nabla \psi_{f,h} \, dx. \quad (2.33)$$

where the stabilization parameter is selected as $\gamma_p = 10^{-2}$ on the basis of numerical experiments. The same types of spaces are used for the intramural filtration and pressure. Since

(2.7) is not enforcing the divergence-free constraint exactly, but the material turns out to be slightly compressible, equal order approximation is stable. We also use P1 finite elements to approximate the structure velocity and displacement.

The performance of matrix (2.28) used as a preconditioner of (2.29) is quantified by the numerical experiments reported in Table 2. As an indicator of the system conditioning, we look at the number of GMRES iterations required to reduce below a given tolerance the relative residual. The values are calculated on the basis of the first 10 time steps of the simulation.

In the special case of positive definite matrices, the number of iterations (# GMRES) required to reduce the relative residual of a factor 10^P , can be estimated as $\# \text{ GMRES} \simeq p\sqrt{K(P^{-1}A)}$, where $K(\cdot)$ is the spectral condition number. Since the initial relative residual is one, by definition, (# GMRES) is equivalent to the number of iterations performed until the relative residual is less than 10^{-P} . In the experiments that follow, we have used $p = 6$. As a result, knowing that the conditioning of the FEM stiffness matrices scales as the square of the number of degrees of freedom, we expect that # GMRES linearly scales with the number of degrees of freedom in absence of preconditioners. Optimal preconditioners are those where the number of GMRES iterations becomes independent of the dimension of the discrete problem.

The results of Table 2 nicely agree with the general GMRES convergence theory, and confirm that (2.28) behaves as an optimal preconditioner for (2.29). Not only the number of iterations to solve the preconditioned system is nearly insensitive with respect to the mesh characteristic size, and consequently the number of degrees of freedom of the discrete problem, but the number of iterations is significantly smaller than in the non-preconditioned case. Reminding that the inversion of (2.28) is a relatively inexpensive operation, the preconditioned algorithm turns out to be a very effective solution method. Table 2 also suggests that the

conditioning of the monolithic problem slightly increases when the time step is refined, especially for coarse meshes, while the good preconditioner performance seems to be unaffected.

It indeed slightly improves, according to the fact that the loosely coupled scheme, and

the related preconditioner, becomes more accurate and effective when the time discretization step decreases. We have tested this algorithm also using quadratic finite elements, P2, for all velocities and displacement fields. In the case of the coarsest mesh $h = 0.05$ cm, GMRES converges in 613.5 (average) iterations, while solving the preconditioned only requires 11 iterations. The preconditioner seems to scale well also with respect to the FEM polynomial degree. The good results on preconditioner performance also correspond to a decrease in the computational time. For $h = 0.05$, $\Delta t = 10^{-4}$, the calculation of 60 time steps of the monolithic scheme require 4.73 s, while for the preconditioned method the time is 1.85 s. For $\Delta t = 10^{-5}$ and 600 time steps the computational times are respectively, 65.8 and 14.6 s.

Table 2. Average number of GMRES iterations for different time steps

$\Delta t=10^{-4}$	$h=0.05$	$h=0.025$	$h=0.0125$
#GMRES (monolithic)	211.4	446.4	1282.9
#GMRES (preconditioner)	10.9	12	13.9
$\Delta t=10^{-5}$	$h=0.05$	$h=0.025$	$h=0.0125$
#GMRES (monolithic)	362.1	498.3	1194.4
#GMRES (preconditioner)	8	10	12.9

2.4.3 Convergence analysis

In this section, we perform the convergence analysis to support the theoretical results on the accuracy of the numerical scheme provided in section 2.3 . Theoretical results for accuracy of the proposed scheme are given in Theorem 3 in our paper [27] which shows that the main drawback of the scheme is related to the splitting of the equations within each time step that decrease the accuracy. For this purpose, we start our investigation for variation of the time step Δt .

Since the analytical one is not available in this case, we use the numerical solution calculated using the monolithic scheme with a small time step equal to $\Delta t = 10^{-6}$ s, as reference solution. This way, we make sure that the splitting error is not polluting the solution, and the approximation error related to the time discretization scheme is negligible. This solution will be denoted with the subscript *ref*. To guarantee a sufficient spatial resolution as well as *inf-sup* stability, we use *P2-P1* approximations for velocity and pressure in the blood flow, combined with *P2-P1* approximation of Darcy's equation and *P2* approximation of the structure displacement and velocity. We investigate the convergence properties of the scheme in the norm $||| \cdot |||_{\bullet, N}^2$ that is used in Theorem 3 in [27]. More precisely, we split it in four parts:

$$\mathcal{E}_{f,h}^N := \rho_f \| v_h^N - v_h^{N,ref} \|_{L^2(\Omega_f)}^2, \quad (2.34)$$

$$\mathcal{E}_{p,h}^N(a) := \rho_p \| \dot{U}_h^N - \dot{U}_h^{N,ref} \|_{L^2(\Omega_p)}^2,$$

$$\mathcal{E}_{p,h}^N(b) := 2\mu_p \| D(U_h^N - U_h^{N,ref}) \|_{L^2(\Omega_p)}^2 + \lambda_p \| \nabla \cdot (U_h^N - U_h^{N,ref}) \|_{L^2(\Omega_p)}^2,$$

$$\mathcal{E}_{p,h}^N(c) := s_0 \| p_{p,h}^N - p_{p,h}^{N,ref} \|_{L^2(\Omega_p)}^2,$$

corresponding to the fluid kinetic energy, the structure kinetic energy, the structure elastic stored energy and the pressure, respectively. We calculate the error between the reference solution and solutions obtained using $\Delta t, \Delta t/2, \Delta t/4, \Delta t/8$ with $\Delta t = 10^{-4}$ for simulations up to the final time $T = 10^{-3}$ s. The mesh discretization step is $h = 0.05$ cm for all cases.

In Table 3 we show the convergence rate relative to the error indicators above calculated using both the monolithic and the loosely coupled scheme. We observe that, as expected, the error indicators scale as $C\Delta t$ when the monolithic scheme is used. Looking at the error of the loosely coupled scheme, we notice that for each of the indicators the magnitude of the error increases with respect to the monolithic scheme. This is the contribution of the splitting error. However, we observe that the total error of the loosely coupled scheme scales as $C\Delta t$.

Table 3. Convergence in time of the monolithic and the partitioned scheme

Monolithic	$\sqrt{\varepsilon_{f,h}^n}$	Rate	$\sqrt{\varepsilon_{p,h}^n(a)}$	Rate	$\sqrt{\varepsilon_{p,h}^n(b)}$	Rate	$\sqrt{\varepsilon_{p,h}^n(c)}$	Rate
$\Delta t=10^{-4}$	2.14E-01		1.48E-01		5.24E-01		1.96E-02	
$\Delta t/2$	1.05E-01	1.02	7.89E-02	0.91	2.82E-01	0.90	6.95E-03	0.92
$\Delta t/4$	5.13E-02	1.04	4.03E-02	0.97	1.44E-01	0.97	3.53E-03	0.98
$\Delta t/8$	2.45E-02	1.07	1.98E-02	1.03	7.07E-02	1.03	1.72E-03	1.03
Partitioned	$\sqrt{\varepsilon_{f,h}^n}$	Rate	$\sqrt{\varepsilon_{p,h}^n(a)}$	Rate	$\sqrt{\varepsilon_{p,h}^n(b)}$	Rate	$\sqrt{\varepsilon_{p,h}^n(c)}$	Rate
$\Delta t=10^{-4}$	2.87E-01		1.84E-01		7.71E-01		1.96E-02	
$\Delta t/2$	1.49E-01	0.94	9.91E-02	0.89	4.15E-01	0.90	1.01E-02	0.95
$\Delta t/4$	7.58E-02	0.98	5.16E-02	0.94	2.13E-01	0.96	5.09E-03	0.99
$\Delta t/8$	3.75E-02	1.01	2.59E-02	0.99	1.06E-01	1.01	2.49E-03	1.03

2.4.4 Absorbing boundary condition

In this section we want to study the improvements obtained by using absorbing boundary conditions. To this purpose, we apply the absorbing boundary condition to the outflow of the same 3D test case shown in Section 2.4.1 for the straight cylinder. The outflow boundary condition is particularly delicate because it has to accurately capture the propagation of the pressure waves. Inappropriate modeling of the flow at the outlet may generate spurious pressure waves that propagate backwards. For this reason, at the outlet, we will use an absorbing boundary condition, proposed in [45] which relates implicitly the flow rate and the mean pressure. In particular, at the outlet we impose:

$$P_{out} = \left(\left(\frac{2}{2\sqrt{2}} \frac{Q^n}{A^n} + \sqrt{\beta\sqrt{A^0}} \right) - \beta\sqrt{A^0} \right) \quad (2.35)$$

Where Q is the flow rate, A is the cross-sectional area related to the mean pressure P and the parameter β is calculated using the independent ring model as follows,

$$\beta = \frac{h_s E}{1 - \nu^2} \frac{1}{R^2} \quad (2.36)$$

Replacing the values for the artery material properties into (2.36) we obtain $\beta=1.43e6$ dyne/cm. Since flow rate is unknown, we can treat it in an explicit way, interpreting the mean pressure boundary condition (2.35) as a normal stress, constant in space. This leads to the following absorbing Neumann boundary condition at the outlet:

$$\sigma_f^{n+1} n = \left(\left(\left(\frac{2}{2\sqrt{2}} \frac{Q^n}{A^n} + \sqrt{\beta\sqrt{A^0}} \right) - \beta\sqrt{A^0} \right) n \right) \quad (2.37)$$

Imposing condition (2.37) significantly reduces spurious reflections that pollute the solution and makes it possible to solve the problem for long time period over cardiac cycles. It is known that the choice of avoiding any reflection is not physiological, since reflections may be generated by the peripheral system. However, in absence of data concerning the downstream cardiovascular tree, the choice of imposing absorbing boundary conditions seems to be the best available option.

Figure 7 shows the solutions computed with and without prescribing the absorbing boundary condition at the outlet. In particular, in the latter case we have imposed a standard stress free outflow condition. We observe that at $t=2\text{ms}$ the pressure wave has not yet reached the end of the domain and therefore the two solutions coincide, while at $t=8\text{ms}$, the reflection has been started and the two solutions differ significantly. Moreover, Figure 8 shows the mean pressure in two cases. The one with absorbing boundary condition is plotted with the dashed line. We notice a significant reduction of the spurious reflections by imposing the absorbing condition.

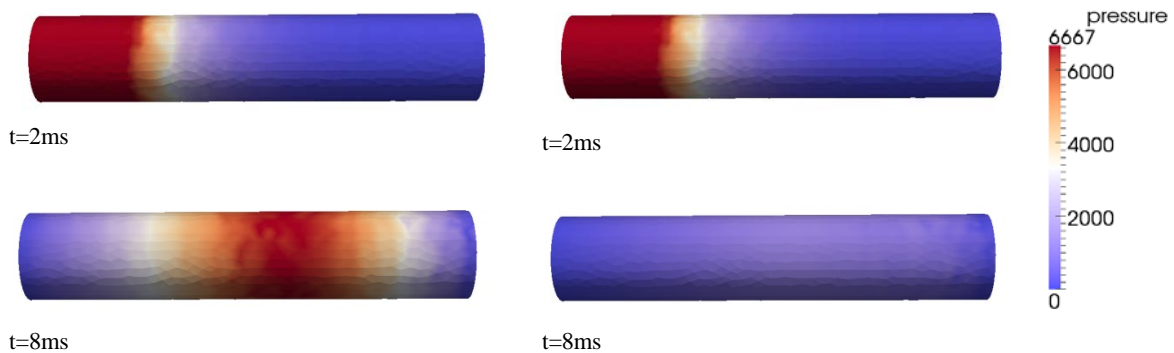


Figure 7. Pressure obtained with (right) and without (left) prescribing absorbing boundary condition for the outflow at $t = 2\text{ms}$ (up) and $t = 8\text{ms}$ (bottom).

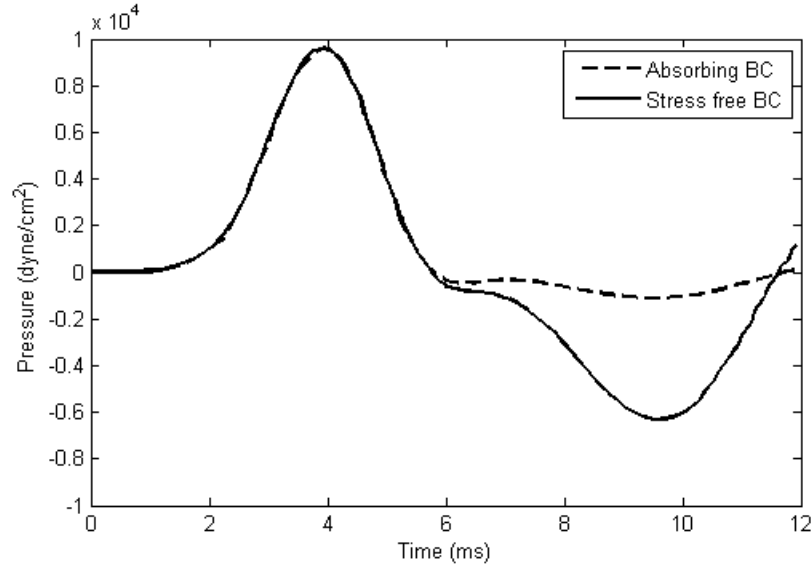


Figure 8. Mean fluid pressure with (dashed line) and without (solid line) absorbing boundary condition for outflow

2.4.5 Sensitivity analysis of poroelastic parameters

The aim of this section is assessing the influence of poroelasticity using the algorithm developed in Section 2.3.1. From the inspection of the Biot model, we observe that k and s_0 are the parameters that describe the influence of poroelasticity on the mechanical behavior of the poroelastic media. Using the available algorithm, we perform a sensitivity analysis of the effects of these parameters on FSI results. In particular, we are interested to qualitatively characterize how the presence of intramural flow coupled to the wall deformation affects the displacement field as well as the propagation of pressure waves. More precisely, by means of a collection of numerical experiments, we qualitatively analyze how the poroelastic phenomena affect the propagation of pressure waves and the poroelastic wall displacement.

The numerical results, obtained for a slightly different test problem than the one considered in Section 2.4.1, including the effect of an elastic membrane at the interface of the

fluid with the thick poroelastic structure. The volume of the thin elastic membrane is negligible and cannot store fluid, but allows the flow through it in the normal direction. The details for the problem formulation including an elastic membrane are provided in our paper [8].

A theoretical analysis complements the numerical investigation. This analysis arises from the qualitative comparison of the governing equations for a poroelastic material with the ones for pure linear elasticity. In particular, the Biot model, namely equations (2.5), (2.6), (2.7) can be reformulated as a one single equation (2.41) below. As a result, we will be able to compare this equivalent representation of Biot model with a simple elasticity equation (2.42).

To manipulate Biot model such that it can be represented into the one single expression, we multiply (2.5) by the operator $s_0 D(\cdot)/Dt$ and we V as the velocity of the poroelastic wall, namely we have $V := D(U)/Dt$.

We obtain,

$$s_0 \rho_p \frac{D^2 V}{Dt^2} - s_0 \mu_p \nabla \cdot D(V) - s_0 \lambda_p \nabla (\nabla \cdot V) + s_0 \alpha \frac{D}{Dt} (\nabla p_p) = 0 \quad (2.38)$$

Then, we apply the operator $\alpha \nabla$ to (2.7):

$$\alpha \nabla \frac{D}{Dt} (s_0 p_p) + \alpha \cdot \alpha \nabla (\nabla \cdot U) + \alpha \nabla (\nabla \cdot q) = 0 \quad (2.39)$$

Also, since based on (2.6), $k^{-1}q = -\nabla p_p$ and k is assumed to be a scalar function, we observe that $\nabla \times \nabla \times q = 0$ and therefore we have:

$$\nabla (\nabla \cdot q) = \Delta q + \nabla \times \nabla \times q = \Delta q \quad (2.40)$$

By replacing (2.40) and (2.39) into (2.38) and dividing by s_0 , we obtain (2.41), which can be compared term by term to the following equivalent expression of the standard elastodynamic equation (2.42), for a material characterized by the same Lamé parameters as the ones used for the poroelastic model.

$$\frac{D^2V}{Dt^2} - \mu_p \nabla \cdot D(V) - \left(\lambda_p + \frac{\alpha^2}{s_0}\right) \nabla(\nabla \cdot V) = \frac{\alpha}{s_0} \Delta q \quad (2.41)$$

$$\rho_p \frac{D^2V}{Dt^2} - \mu \nabla \cdot D(V) - \lambda \nabla(\nabla \cdot V) = 0 \quad (2.42)$$

Two major considerations emerge: First, by comparing equations (2.41) and (2.42) we can see that, poroelasticity introduces an additional term Δq on the right hand side of (2.41), which breaks the energy conservation principle relative to the standard elastodynamic equation. We also remark that the magnitude of Δq is proportional to the hydraulic conductivity k . Therefore, this term affects the energy, at a rate which is directly proportional to k . Second, by comparing equations (2.41) and (2.42) we observe that poroelasticity affects the phenomena that are governed by the second Lamé constant of the material, λ and this effect is related to the magnitude of s_0 in the poroelastic model. More precisely, the poroelastic material is equivalent to a purely elastic one with an augmented second Lamé parameter (2.43).

$$\lambda = \lambda_p + \frac{\alpha^2}{s_0} \quad (2.43)$$

We explain and support these qualitative conclusions on the basis of numerical simulations. More precisely, we discuss a collection of numerical experiments aiming at clarifying and supporting the qualitative considerations on the role of poroelasticity on FSI.

We compare the results obtained using three exponentially increasing values of the hydraulic conductivity $k=5 \times 10^{-9}, 5 \times 10^{-7}, 5 \times 10^{-5}$, starting from the reference values of Table 1. In Figure 9, we analyze the displacement of the fluid-wall interface at the intermediate time $t = 3.5\text{ms}$ when the peak of the pressure wave is located almost at the center of the arterial segment. The results show that the amplitude of the pressure wave inversely depends on the hydraulic conductivity. Based on this observation, we can also conclude that the forcing term Δq

dissipates energy, at a rate which is directly proportional to k , and as a result, we conclude that increasing the hydraulic conductivity decreases the amplitude of pressure wave in the domain.

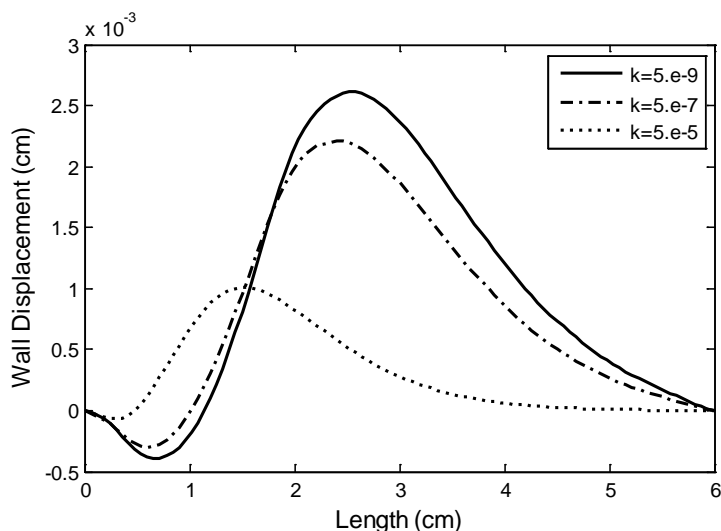


Figure 9. Displacement of the fluid-wall interface for different k values at $t=3.5$ ms

Moreover, as it has been discussed in (2.43), we expect that changing s_0 corresponds to modifying the second Lamé parameter characterizing the poroelastic wall. However, it is not straightforward to determine what the role of λ is, on the fluid-structure interaction. The numerical simulations based on the proposed FSI scheme turn out to be effective also in this respect. More precisely, we have simplified the discrete scheme (2.24) in order to model the interaction of a viscous fluid with a purely elastic impermeable structure. We notice that the resulting scheme is exactly the one proposed in [37]. Using this tool, we have performed a simple sensitivity analysis of the parameter λ on a model that describes the interaction of a viscous fluid with an elastic impermeable structure. We observe that decreasing λ slightly slows down the propagation of the pressure waves (Figure 10). Using this result, we can then proceed to test the validity of our hypothesis on the effect of s_0 . To this purpose, we now use the FSI scheme for the poroelastic model where λ is set to the reference value of Table 1, but the value

of the mass storativity is varied as $s_0 = 5 \times 10^{-7}, 5 \times 10^{-6}, 10^{-5}$. The results shown in Figure 11, shows that increasing s_0 has similar effect on wave speed, since it corresponds to decreasing the second Lamé constant. More precisely, increasing s_0 from 5×10^{-6} to 10^{-5} corresponds to decrease λ , which in turn slows down the pressure wave propagation. Conversely, decreasing the mass storativity corresponds to increase the equivalent second Lamé parameter. As a result, the pressure wave speeds up.

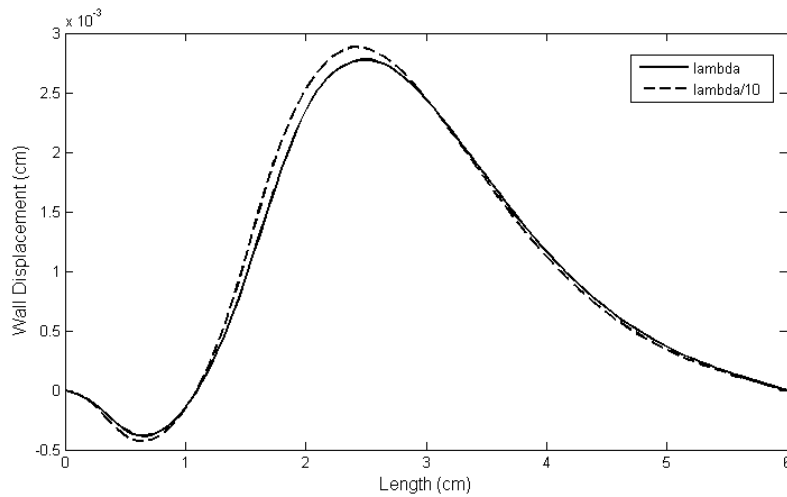


Figure 10. Displacement of the fluid-wall interface at $t=3.5\text{ms}$ for $\lambda = 4.28 \times 10^6$ and $\lambda = 4.28 \times 10^5$

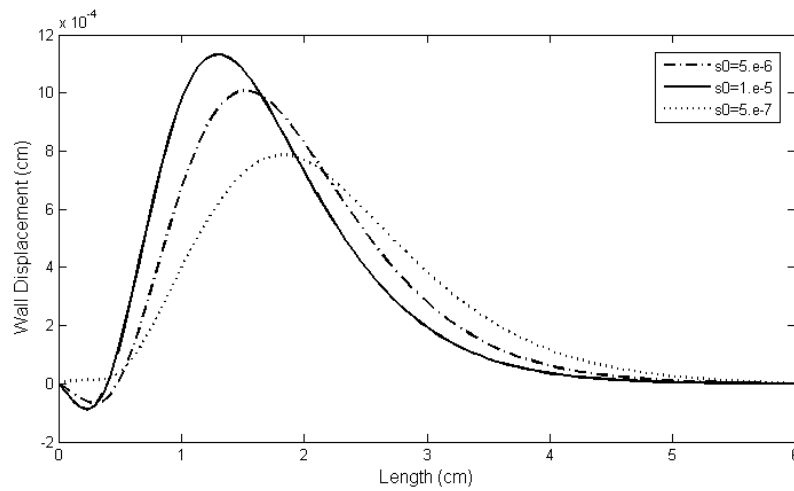


Figure 11. Displacement of the fluid-wall interface at $t=3.5\text{ms}$ for different values of storativity

2.5 SUMMARY

We have studied the interaction of a free fluid with a poroelastic material with the assumption of having small deformations. After setting appropriate governing equations on adjacent domains and discussing the corresponding interface conditions, we have considered the discretization of the problem in the framework of the finite element method. Particular attention must be devoted to the approximation of the interface conditions, which are non-standard with respect to the ones that arise in the coupling of homogenous partial differential equations. We have shown that the Nitsche's method, used for the weak approximation of boundary and interface conditions for elliptic or parabolic problems, is appropriate to enforce the interface constraints in the variational formulation. Since all the interface conditions correspond to suitable operators in the variational problem, time-lagging allows to split the fully coupled problem into subproblems, relative to the main governing equations, such as free fluid flow, Darcy filtration and elastodynamics. Also the resulting loosely coupled problem formulation turns out to be stable, provided that it is combined with suitable stabilization operators. This solution approach is very effective from the computational standpoint, but suffers from low accuracy. In order to merge the computational efficiency of the loosely coupled scheme with the good accuracy and stability properties of the monolithic formulation, we develop a numerical solver where the former scheme acts as a preconditioner for the latter. The theory and the numerical results suggest that this approach is very effective because the loosely coupled scheme behaves as an optimal preconditioner for the monolithic formulation. This solution algorithm turns out to be very robust with respect to the characteristic physical parameters of the problem. Indeed, we have successfully applied it to the analysis of a problem related to blood flow in arteries as well as to the study of subsurface flow and deformation of a fractured reservoir [27].

3.0 ENERGY DISTRIBUTION IN THE COUPLED FSI PROBLEMS

The present chapter analyzes the distribution and dissipation of the energy in the coupling between the pulsatile flow and a deformable structure. The objective is to determine new criteria, based on the energy distribution, for the assessment of constitutive models of the structure part in a fluid-structure interaction framework. A computational model of blood flow and arterial deformation is used to examine the behavior of different constitutive models of the arterial wall. In particular, we consider poroelastic and viscoelastic descriptions of the artery. Energy estimates are derived for each constitutive model of the arterial wall from the weak formulation of the fluid/solid coupled problem and are applied to assess energy exchange between different compartments of the model. Two-dimensional numerical experiments are presented to illustrate the energy distribution within the fluid and solid model compartments. Results highlight the importance of including both poroelasticity and viscoelasticity in modeling fluid-structure interaction in large arteries. Our results show that both viscoelastic and poroelastic models for the arterial walls absorb part of the input energy flowing to the artery, but the underlying mechanisms are substantially different.

3.1 BACKGROUND

A comprehensive understanding of pressure and flow pulse wave propagation in the cardiovascular system can provide valuable information for clinical diagnosis and treatment. Computational models of arteries play a significant role in current vascular research as they can predict properties of the cardiovascular system that cannot be measured in vivo [46]. Moreover, in vivo measurements of hemodynamic parameters are expensive and limited to easily accessible arteries. However, due to the complexity of the cardiovascular system, simplifying assumptions need to be taken into account when studying the interaction between blood flow and vessel wall. Assuming that the arterial wall is an elastic structure is a common assumption in FSI modeling. However, arterial walls, like other soft tissues, consist primarily of water [47]. They exhibit both viscoelastic and poroelastic behavior. In particular, poroelasticity plays an important role in the regulation of plasma and solute transport across the wall.

Viscoelasticity is the major mechanical characteristic of soft tissue. It accounts for a combined fluid like (viscous) and solid like (elastic) behavior. Due to its role in physiological and pathophysiological function of soft tissues, important information can be obtained by using computational methods that characterize these phenomena and model their underlying mechanisms. In [48] two different microscopic mechanisms responsible for macroscopic viscoelastic effects have been considered, one is the intrinsic viscoelasticity of the collagen matrix and the other is due to the interphase drag between extracellular matrix and fluid phase, better known as poroelasticity. Considering poroelasticity is important because almost all biological tissues contain connective tissues and cells surrounded by fluid-filled extracellular space and both components consist primarily of water [49]. Poroelastic phenomena become

crucial when modeling the mass transport in arteries, which is a mechanism that provides nourishment, removes waste and delivers drugs to the inner layers of large arteries [50].

Earlier numerical models used to predict blood flow are based on rigid geometries [13] in which only the arterial lumen needs to be reconstructed and discretized, yielding results in a relatively short time. However, the rigid wall assumption precludes pressure wave propagation and overestimates the wall shear stress. There exist a variety of methods to include the effects of the moving wall in computations, the most prevalent being the arbitrary Lagrangian–Eulerian (ALE) approach. Applications of the ALE to hemodynamics are discussed in [51-53] and references therein. For example, the work in [14] focuses on developing FSI numerical methods for the interaction between incompressible fluids and non-linear elastic solids, with application to the arterial blood flow. The new approach is evaluated on a patient specific abdominal aorta. The paper proposes that future developments should address extensions to hyperelastic materials with viscoelasticity, which represent more accurately the behavior of the arterial wall.

Energy distribution in one heart cycle has been studied in the seminal works by Skalak [54, 55] for pulmonary artery at rest and in exercise conditions. Also, Bertram [56] presented methods using Womersley's theory for calculating viscous and viscoelastic energy dissipation as a function of time for a segment of canine carotid artery in-vivo. However, their work does not account for the poroelasticity of the arterial wall. Tsaturyan et al. [57] suggested that extracellular fluid flow dominates the apparent viscoelastic properties of passive cardiac muscle. The authors claimed that actual tissue viscoelasticity plays a relatively minor role. The dominant role of poroelasticity in the mechanics of articular cartilage is generally accepted in [57], constructing a relatively strong case for the same being true for myocardium [49, 58, 59]. In [59] Taber discussed the viscoelastic type effect due to nonlinear poroelasticity and examined the role

of extracellular fluid flow in the apparent viscoelastic behavior of cardiac muscle. In [59] comparison of theoretical and published experimental results showed that poroelasticity can account for several measured myocardial features; including the relative insensitivity of the stress strain curve to loading rate and of the stress relation curve to the muscle stretch. The study by Taber also compared the experimental and computed hysteresis loops and observed that they differ significantly, concluding that poroelastic effects alone cannot justify hysteresis. Thus, it was suggested that both poroelastic and viscoelastic effects must be considered in biomechanical studies of passive cardiac muscle.

Modeling fluid-structure interaction in porous media is a challenging and computationally demanding task. The coupling between a fluid and a single layer poroelastic structure has been previously studied in [4, 33]. In particular, the work in [4] develops a computational model of the interaction between an incompressible, Newtonian fluid, described using the Navier-Stokes equations, and a poroelastic structure modeled as a Biot system. The problem was solved using both a monolithic and a partitioned approach. In [35] a new partitioned strategy for the solution of coupled Navier-Stokes and Biot systems is presented. This approach is based on Nitsche's method for enforcing fluid/solid interface conditions and provides an efficient solution method for these complex equations. In [29] the results were extended to idealized 3D models of arteries, such as straight and bent cylinders.

Experimental measurements of arterial wall indicate that arteries exhibit a viscoelastic behavior [60, 61]. Canic et al. [17, 62] modeled blood flow in compliant artery using linear viscoelastic membrane equations to model mechanical properties of arterial walls and compared theoretical results obtained from Kelvin-Voigt model with experimental results in Armentano et al. [16]; however those results were obtained under the assumption that the model is one

dimensional. Bukac et al. [63] extended the work of [17, 62] by presenting a two dimensional model capturing the radial and longitudinal displacement of the linearly viscoelastic Koiter shell for the underlying fluid structure interaction problem. The results were comparable with the monolithic scheme proposed in [64] as well as viscoelastic model in [65]. In particular, the effect of aging on the phase difference between the pressure and flow-rate waveforms in the carotid artery was studied in [65].

In the present work we pursue two general objectives. Firstly, we develop a computational model of pulsatile blood flow in large arteries that embraces different constitutive models for the arterial wall. In particular, we focus on a poro-viscoelastic description of the arterial tissue. Secondly, we apply the model to compare poroelastic and viscoelastic behaviors on the basis of energetic criteria derived from the energy balance of fluid-structure interaction. In particular, we aim to identify and compare the sources of energy dissipation in the arterial wall. Determining the nature of this dissipation mechanism is important for understanding how well viscoelasticity and poroelasticity capture the natural behavior of the artery. More precisely, we pursue the following quantitative objectives. One is to quantify the dissipative behavior of a linear viscoelastic model for arterial wall on the fluid structure interaction under pulsatile blood flow in arteries. The other is to evaluate the role of the extracellular fluid flow in the apparent viscoelastic behavior of arterial wall.

3.2 FORMULATION

We consider the blood flow in a compliant channel bounded by a thick material representing the arterial wall, with a two way coupling between the fluid and the structure. We assume that the

vessel is sufficiently large so that the non-Newtonian effects can be neglected. The fluid is modeled as an incompressible, viscous, Newtonian fluid using the Navier-Stokes equations in a deformable domain $\Omega_f(t)$:

$$\rho_f \left(\frac{\partial v}{\partial t} + v \cdot \nabla v \right) = \nabla \cdot \sigma_f \quad \text{in } \Omega_f(t) \quad (3.1)$$

$$\nabla \cdot v = 0 \quad \text{in } \Omega_f(t) \quad (3.2)$$

Here v and ρ_f stand for fluid velocity vector field and fluid density, respectively, and $\sigma_f = -p_f I + 2\mu_f D(v)$ is the fluid Cauchy stress tensor where p_f is fluid pressure, μ_f is fluid dynamic viscosity and the symmetric part of fluid velocity gradient is defined as $D(v) = \frac{1}{2}(\nabla v + \nabla v^T)$.

We model the arterial wall as a thick structure, which accounts for the media and the adventitia. We consider different constitutive models for the wall: elastic, viscoelastic and poroelastic. Even though these models will be used separately, for the sake of generality we present here the description of a poro-visco-elastic arterial wall. We assume that the arterial wall is incompressible and isotropic. To model the poroelastic properties of the arterial wall, we use the Biot system [24, 35] that describes the mechanical behavior of a homogeneous and isotropic elastic skeleton, and connecting pores filled with fluid. We assume that the fluid flow through the porous medium is modeled using the Darcy equation. Hence; the Biot system for a poroelastic material consists of the momentum equation for balance of total forces (3.3), Darcy's law (3.4) and the storage equation (3.5) for the fluid mass conservation in the pores of the matrix:

$$\rho_s \frac{D^2 U}{Dt^2} - \nabla \cdot (\sigma^S - \alpha p_p I) = 0 \quad \text{in } \Omega_p(t) \quad (3.3)$$

$$k^{-1}q = -\nabla p_p \quad \text{in } \Omega_p(t) \quad (3.4)$$

$$\frac{D}{Dt}(s_0 p_p + \alpha \nabla \cdot U) + \nabla \cdot q = 0 \quad \text{in } \Omega_p(t) \quad (3.5)$$

In equation (3.4), the relative velocity of the fluid within the porous wall is denoted by q and p_p is the fluid pressure. Hydraulic conductivity of the porous matrix is denoted by k , the coefficient s_0 is the storage coefficient, and the Biot-Willis constant α is the pressure-storage coupling coefficient. In equation (3.5), D/Dt is material derivative, ρ_s is arterial wall density and σ denotes the visco-elasticity stress tensor. In the general viscoelastic formulation for the arterial wall, it is assumed that the stress tensor consists of two parts, σ^E and σ^{visco} :

$$\sigma^E = 2\mu_p D(U) + \lambda_p \nabla \cdot U I \quad (3.6)$$

$$\sigma^{visco} = \eta D(\dot{U}) + \frac{\eta}{2} (\nabla \cdot \dot{U}) \quad (3.7)$$

In (3.6), σ^E describes the purely elastic stress that is given by the linear elasticity model, where λ_p and μ_p are the Lamé coefficients of the wall. The symmetric part of deformation gradient for the structure is denoted by $D(U)$. Under the hypothesis of small deformations, we define $D(U) = \frac{1}{2}(\nabla U + \nabla U^T)$. The second part of the Cauchy stress tensor, namely σ^{visco} , accounts for the viscoelastic properties of the vessel walls. It is obtained by utilizing a simple linear viscoelastic model based on the Kelvin-Voigt viscoelasticity model where a dashpot is arranged in parallel with a spring. We denote $\dot{U} = \frac{DU}{Dt}$. The constitutive model for the viscoelastic case can be written as (where variable η is the viscous modulus of the arterial wall:

$$\sigma^S = \sigma^E + \sigma^{visco} = 2\mu_p D(U) + \lambda_p \nabla \cdot U I + \eta D(\dot{U}) + \frac{\eta}{2} (\nabla \cdot \dot{U}) \quad (3.8)$$

and the poro-visco-elastic stress is defined as:

$$\sigma_p = \sigma^S - \alpha p_p I \quad (3.9)$$

With the assumption of axial symmetry, we use the model for the arterial wall in cylindrical coordinates (r, Θ, z) , with z being the distance on the longitudinal axis. The displacement vector is written in the form of $U = [U_r, U_\theta, U_z]$ and tensor D becomes:

$$D(U) = \begin{bmatrix} \frac{\partial U_r}{\partial r} & 0 & \frac{1}{2} \left(\frac{\partial U_z}{\partial r} + \frac{\partial U_r}{\partial z} \right) \\ 0 & \frac{U_r}{r} & 0 \\ \frac{1}{2} \left(\frac{\partial U_z}{\partial r} + \frac{\partial U_r}{\partial z} \right) & 0 & \frac{\partial U_z}{\partial z} \end{bmatrix} \quad (3.10)$$

At the inlet and outlet boundaries of the fluid domain, we use the Neumann boundary conditions provided in (3.11) and (3.12) using values of static pressure:

$$\sigma_f n_f = -p_{in}(t) n_f \quad \text{on } \Gamma_f^{in} \times (0, T) \quad (3.11)$$

$$\sigma_f n_f = -p_{out}(t) n_f \quad \text{on } \Gamma_f^{out} \times (0, T) \quad (3.12)$$

The challenges of the numerical discretization of FSI problems in hemodynamics are associated with the added-mass effect and the high nonlinearity of the problem [66]. In the case when the structure is poroelastic, one encounters an additional difficulty due to the fluid-porous media coupling.

The Biot system is coupled to the fluid by prescribing coupling conditions at the interface Γ . In particular, we impose the continuity of the velocity and of the normal stress at the interface via the kinematic (no-slip and conservation of mass) and dynamic (conservation of momentum) interface conditions. Denoting by n_f the outward normal to the fluid domain and by t_f the corresponding tangential vector, the coupling conditions read as follows:

$$v \cdot t_f = \frac{DU}{Dt} \cdot t_f \quad \text{on } \Gamma(t) \quad (3.13)$$

$$v \cdot n_f = \left(\frac{DU}{Dt} + q \right) \cdot n_f \quad \text{on } \Gamma(t) \quad (3.14)$$

$$n_f \cdot \sigma_f n_f = -p_p \quad \text{on } \Gamma(t) \quad (3.15)$$

$$n_f \cdot \sigma_f n_f - n_f \cdot \sigma_p n_f = 0 \quad \text{on } \Gamma(t) \quad (3.16)$$

$$t_f \cdot \sigma_f n_f - t_f \cdot \sigma_p n_f = 0 \quad \text{on } \Gamma(t) \quad (3.17)$$

3.2.1 Energy estimation

In order to obtain the energy estimation, we proceed as in [35, 67, 68]. In particular, for blood flow, we multiply equations (3.1) and (3.2) by v and, pf , respectively. The energy of the Biot system is obtained by multiplying equation (3.3) by \dot{U} , equation (3.4) by q and equation (3.5) by p_p . The algebraic identity (3.18) will be systematically used in the derivations. As a result, we derive the following energy equality (3.19) for the coupled problem.

$$\begin{aligned} & \int_{\Omega} u \, d_t u = \frac{1}{2} d_t \|u\|_{\Omega}^2 \quad (3.18) \\ & \underbrace{\int_{\Omega_f(t)} \frac{\rho_f}{2} \|v\|^2}_{\text{Fluid kinetic energy}} + \underbrace{\int_{\Omega_p(t)} \frac{1}{2} (\rho_p \|\dot{U}\|^2 + 2 \mu_p \|D(U)\|^2 + \lambda_p (\nabla \cdot U)^2)}_{\text{wall kinetic and stored energy}} \\ & + \underbrace{\int_0^t \int_{\Omega_f(s)} 2\mu_f \|D(v)\|^2}_{\text{viscous dissipation}} + \underbrace{\int_0^t \int_{\Omega_p(s)} \eta \|D(\dot{U})\|^2 + \int_0^t \int_{\Omega_p(s)} \frac{\eta}{2} \|\nabla \cdot \dot{U}\|^2}_{\text{wall dissipation}} \\ & + \underbrace{\int_{\Omega_p(t)} \frac{1}{2} (S_0(p_p)^2)}_{\text{poroelastic storage term}} + \underbrace{\int_0^t \int_{\Omega_p(s)} k^{-1} \|q\|^2}_{\text{intramural flow energy}} = \underbrace{E_f(0)}_{\text{fluid initial energy}} \quad (3.19) \\ & + \underbrace{E_s(0)}_{\text{wall initial energy}} - \underbrace{\int_0^t \int_{\Gamma_f^{in}} p_{in}(t) v \cdot n_f - \int_0^t \int_{\Gamma_f^{out}} p_{out}(t) v \cdot n_f}_{\text{net power of input pressure wave}} \\ & + \underbrace{\left\{ - \int_0^t \int_{\Gamma_f^{in}} \rho_f \frac{\|v\|^2}{2} v \cdot n_f - \int_0^t \int_{\Gamma_f^{out}} \rho_f \frac{\|v\|^2}{2} v \cdot n_f \right\}}_{\text{kinetic energy exchange with the exterior}} \end{aligned}$$

Where $\|\cdot\|$ denotes the Euclidean norm when applied to a vector or the Frobenius norm when applied to a tensor.

We define E_f as the fluid kinetic energy and E_s as the structure kinetic and stored energy given by (3.20).

$$E_f = \int_{\Omega_f(t)} \frac{\rho_f}{2} \|v\|^2 \quad (3.20)$$

$$E_s = \int_{\Omega_p(t)} \frac{1}{2} \left(\rho_p \|\dot{U}\|^2 + 2 \mu_p \|D(U)\|^2 + \lambda_p (\nabla \cdot U)^2 \right)$$

The right hand side of (3.19) represents the kinetic and stored energy of the initial state and the power of external forces. The left hand side of (3.19) represents the different forms of the system internal energy. On the left hand side of (3.19), we identify the following expressions, which define the total energy in the elastic, viscoelastic and poroelastic cases respectively.

$$E_{total_{Elastic}}(t) = E_f(t) + E_s(t) + \int_0^t \int_{\Omega_f(s)} 2\mu_f \|D(v)\|^2 \quad (3.21)$$

$$E_{total_{viscoelastic}}(t) \quad (3.22)$$

$$= E_{total_{Elastic}}(t) + \int_0^t \int_{\Omega_p(s)} \eta \|D(\dot{U})\|^2$$

$$+ \int_0^t \int_{\Omega_p(s)} \frac{\eta}{2} \|\nabla \cdot \dot{U}\|^2$$

$$E_{total_{poroelastic}}(t)$$

$$= E_{total_{Elastic}}(t) + E_{storage}(t) + \int_0^t \int_{\Omega_p(s)} k^{-1} \|q\|^2 \quad (3.23)$$

Where $E_{storage}$ is the energy stored into the porous matrix because of pore deformation.

$$E_{storage} = \int_{\Omega_p(t)} \frac{1}{2} \left(S_0(p_p)^2 \right) \quad (3.24)$$

In the case when a fluid is coupled with an “elastic” structure, (3.21) shows that the only dissipative mechanism is viscous dissipation of the fluid. For the viscoelastic model we have additional energy damping due to the viscoelasticity of the wall. For the poroelastic model, in addition to the dissipation due to the fluid viscosity, another energy exchange mechanism appears due to the permeability of the porous matrix and corresponding filtration velocity.

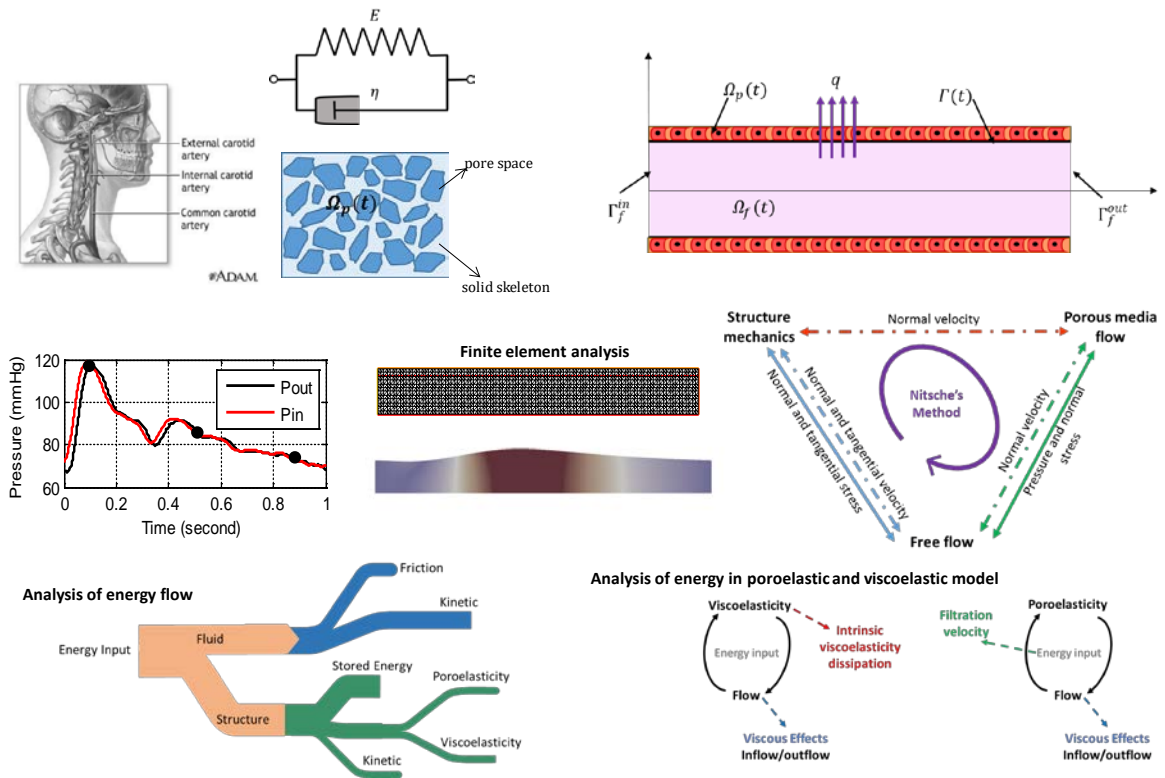


Figure 12. Computational approach; (a) poro-viscoelastic model of the arterial wall (left), schematic of the fluid and structure domains (right); (b) inflow/outflow pressure waves and choice of snapshot times (left); computational mesh (middle), Coupling conditions in Fluid-poroviscoelastic structure interaction (right).

3.3 NUMERICAL PROCEDURE

We have adopted the partitioned, loosely coupled algorithm that we developed in Section 2.3.1 . The partitioned solve is based on weak enforcement of interface conditions using Nitsche's method , and allows us to independently solve the equations for each problem, at each time step. Namely, structure mechanics, the intramural filtration and the blood flow problem are solved separately, once at each time step, denoted with the generic index n . The stability of the partitioned algorithm is a very delicate question. Stability is guaranteed for our solver thanks to the introduction of the pressure stabilization operator proposed in [37] and provided that several penalty parameters are appropriately selected [69]. Here the steps are explained for poroelastic model. Similar approach for viscoelastic model is performed. The only difference is that steps 1,2,3 are solved when the poroelastic model is adopted; in the elastic and viscoelastic cases only step 1 (solving for the displacement solely) and 3 are necessary because the arterial wall is considered to be impermeable.

Step1: We first solve the elastodynamics equation for the structure, where the pressure term has been time-lagged.

$$\rho_p \frac{D^2 U}{Dt^2} - \nabla \cdot (\sigma^s - \alpha p_p^{n-1} I) = 0 \quad \text{in } \Omega_p$$

This equation is complemented with the following Robin-type boundary condition on Γ , where γ_f is a parameter that should be chosen sufficiently large to guarantee stability and it is inversely proportional to the space discretization mesh characteristic size h ,

$$\begin{aligned} n_p \sigma_p n_p &= n_p \sigma_f^{n-1} n_p - \gamma_f (h^{-1}) \mu_f \left(\frac{DU}{Dt} - v^{n-1} + q^{n-1} \right) \cdot n_p \\ t_p \sigma_p n_p &= t_p \sigma_f^{n-1} n_p - \gamma_f (h^{-1}) \mu_f \left(\frac{DU}{Dt} - v^{n-1} \right) \cdot t_p \end{aligned} \tag{3.25}$$

Step 2: The second problem consists of Darcy equations, Complemented with the boundary condition (3.26):

$$\begin{aligned}
k^{-1}q &= -\nabla p_p && \text{in } \Omega_p \\
\frac{D}{Dt}(s_0 p_p + \alpha \nabla \cdot U) + \nabla \cdot q &= 0 && \text{in } \Omega_p \\
p_p &= -n_p \sigma_f^{n-1} n_p - \gamma_f (h^{-1}) \mu_f \left(v^{n-1} - \left(\frac{DU}{Dt} \right)^{n-1} - q \right) \cdot n_p && (3.26)
\end{aligned}$$

Step 3: Finally, the third problem corresponds to the fluid equations:

$$\begin{aligned}
\rho_f \left(\frac{\partial v}{\partial t} + v \cdot \nabla v \right) &= \nabla \cdot \sigma_f && \text{in } \Omega_f \\
\nabla \cdot v &= 0 && \text{in } \Omega_f \\
v \cdot n_f &= \left(\frac{DU}{\partial t} + q \right) \cdot n_f, \quad v \cdot t_f = \frac{DU}{\partial t} \cdot t_f && \text{on } \Gamma && (3.27)
\end{aligned}$$

where the kinematic conditions (26) have been enforced using the classical Nitsche's method formulation for the boundary conditions.

The non-linearity in the Navier-Stokes equations due to the convective term has been linearized using the Picard method, namely, $v^{n+1} \cdot \nabla v^{n+1} \approx v^n \cdot \nabla v^{n+1}$. Moreover, Streamline Upwind/Petrov-Galerkin (SUPG) formulation is used to stabilize the convection term [70]. To minimize the numerical dissipation, we adopt the Newmark scheme for the wall discretization. The continuity equation for the poroelastic pressure is discretized using the Backward Euler scheme. For the discretization of the blood flow equations we adopt $P2 - P1$ approximations for velocity and pressure, respectively, which ensures *inf-sup* stability of the scheme. The same types of spaces are used for the intramural filtration and pressure. In addition, we use P2 finite elements for the discretization of the structure displacement field.

3.4 NUMERICAL SIMULATIONS

In this section, we perform numerical experiments on the simplified 2D/axial symmetric problems representing blood-vessel systems. Our aim is to clarify the importance of including arterial wall poroelastic and viscoelastic behaviors in the vascular FSI. The analysis of simulations will be performed using the general energy estimation (3.19). Namely, we analyze the energy exchange between different compartments of the elastic, poroelastic and viscoelastic model. To illustrate the behavior of the models, we consider two examples. The first test, corresponds to the benchmark problem that has been used in several works [35, 37, 42] for testing the results of fluid-structure interaction algorithms for blood flow. The flow is driven by a pressure wave imposed at the inlet boundary for a short amount of time, which then propagates through the domain. The viscoelasticity modulus in this problem is small compared to its physiological value [71]. Choosing viscous modulus in this range allows reasonable wave propagation in the channel and avoids backflow from inlet boundary. The second test problem concerns a healthy common carotid artery. Model parameters are centered in the range relevant to cardiovascular applications. The viscoelasticity coefficient is physiologically reasonable, and higher than in the previous example. In this example, we show that our computational model gives rise to physiologically reasonable solutions by comparing our results with experimental data. In both numerical examples, the initial energy of the fluid and structure is defined to be zero; namely both are at rest. $E_f(0) = E_s(0) = 0$.

3.4.1 Benchmark 1: FSI analysis for short pressure wave

Benchmark problem described in detail in Section 2.4.1, is employed. The thick structure equations are written in cylindrical coordinates to naturally account for the circumferential strains, and coupled with Cartesian equations for the fluid. Model dimension and physical parameters for this example are provided in Table 4. The problem domain is discretized with a mesh of 7200 triangles and the propagation of the pressure wave is analyzed over the time interval $[0, 0.005]$ sec. The final time is smaller than the time necessary for the pressure wave to reach the outflow. In this way, the unphysical reflected waves that may originate at the outflow because of homogeneous Neumann conditions do not pollute the considered results. Also, the velocity at the outlet remains small for the entire simulation time. For this reason, energy loss to the exterior is minimized. Figure 13 shows a snapshot of the pressure wave moving along the channel, together with the contour plot of the radial displacement of the artery. The visualization clearly shows the coupling between the two domains. More precisely, the pressure wave, travels from left to right, displacing the thick structure.

Table 4. Physical and numerical parameters for benchmark problem 1

Parameters	values	Parameters	values
Radius (cm)	0.5	Lame coeff. μ_p (dyne/cm ²)	1.07×10^6
Length (cm)	15	Mass storativity, s_0 (cm ² /dyne)	5×10^{-6}
Wall thickness (cm)	0.1	Hydraulic conductivity, k (cm ³ s/g)	5×10^{-9}
Wall density (g/cm ³)	1.1	Biot-Willis constant, α	1
Fluid density (g/cm ³)	1	γ_f, γ_s	2500
Dynamic viscosity (poise)	0.035	Viscous modulus η (dyne.s/cm ²)	100
Lame coeff. λ_p (dyne/cm ²)	4.28×10^6	Time step Δt	10^{-5} sec

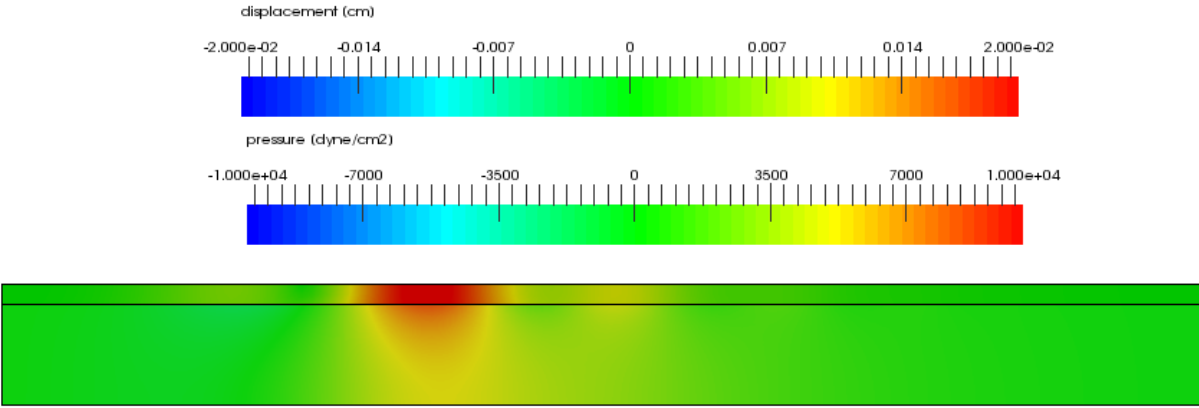


Figure 13. A snapshot of the pressure wave traveling from left to right coupled with the radial component of the structure displacement. The legend shows the values for the pressure (bottom scale) and displacement (top scale)

For this test case, we also compare the results obtained using the proposed FSI scheme with other results available in literature. In particular we refer to the simulations of [72, 73] obtained using the data of Table II in [38]. Excellent agreement is observed among the results of the tree methods, reported in Figure 14. This test serves as verification of the software used for the simulations and as validation of the method.

Figure 15 shows time evolution of the energy components of the system for elastic, viscoelastic and poroelastic structures; precisely: E_f^N, E_s^N and E_{loss}^N for $n = 1, \dots, N$ where N is the number of time steps. E_{loss} corresponds to the viscous loss in fluid, the loss due to the viscoelasticity of the arterial wall and the filtration velocity in the poroelastic model. We observe that the total energy (sum of fluid kinetic energy and elastic kinetic and stored energy, including viscous energy loss) reaches a constant plateau equal to the total energy input. This indicates that the mass balance is accurately satisfied.

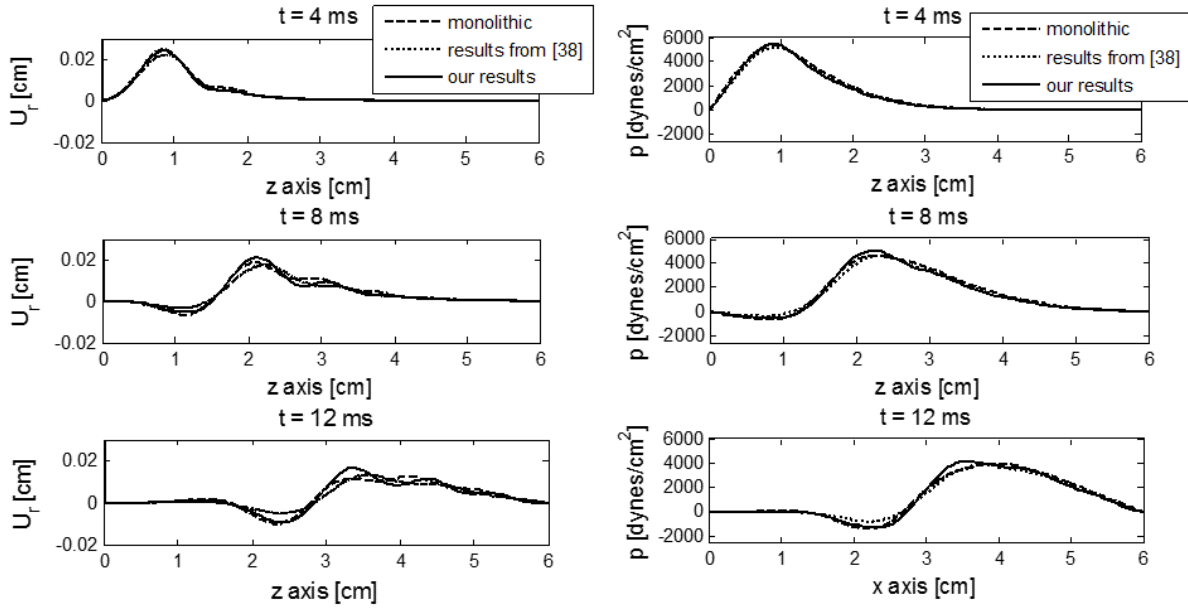


Figure 14. Fluid–structure interface displacement (left panel) and mean pressure (right panel) versus z , at $t = 4, 8, 12$ ms, computed with the monolithic scheme by Quaini [73] (time step $=e-4$; dashed line) and with operator-splitting scheme [72] (time step $=5e-5$; dotted line). Our result is plotted using a solid line.

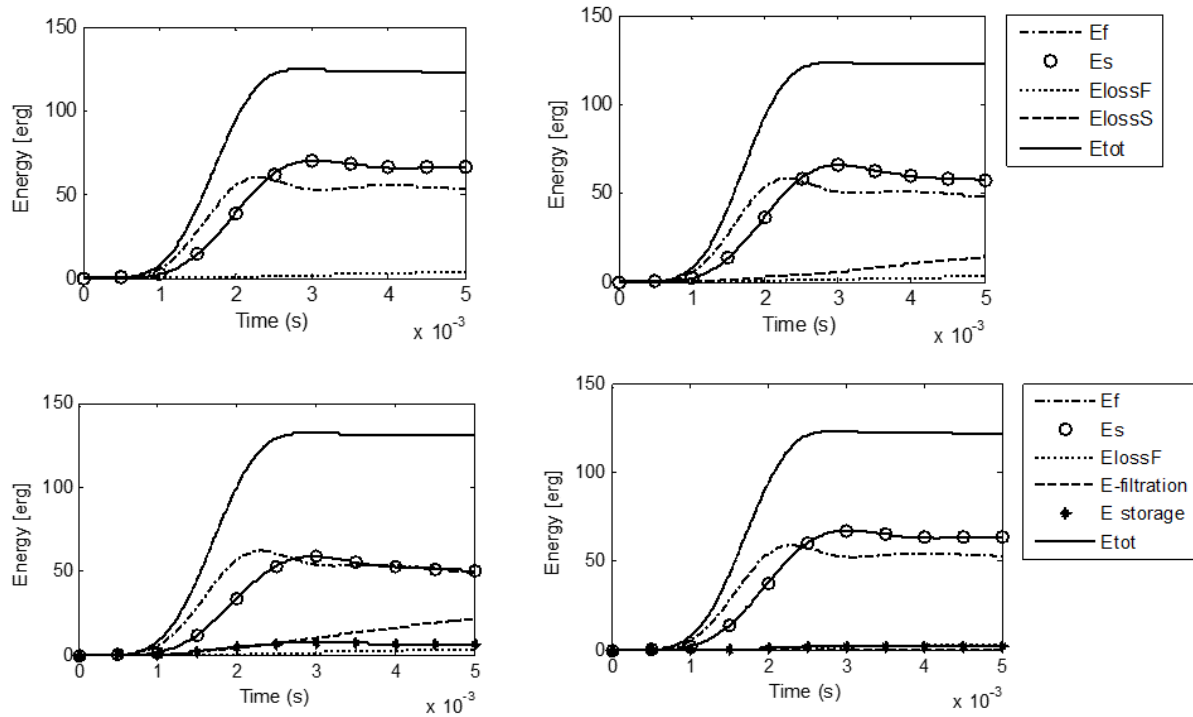


Figure 15. Time evolution of the energy in each component for elastic (top, left), viscoelastic (top, right) and poroelastic cases with $k = 5 \times 10^{-6} \text{ cm}^3/\text{s/g}$ (left) and $k = 5 \times 10^{-9} \text{ cm}^3/\text{s/g}$ (right) in benchmark problem 1.

The first plot in Figure 17 shows the available energy distributed in different components for each poroelastic, viscoelastic and elastic cases at final time $t=0.005$ sec. The results confirm that for the pressure impulse problem, characterized by high wall accelerations, viscoelastic losses dominate. The pressure peak is too short to generate a significant intramural flow. The percentage of fluid viscous dissipation in all cases is almost the same. The stored energy (E_s) in the elastic case is slightly larger than in the other cases since it has no other way for being dissipated.

3.4.2 Benchmark 2: FSI analysis under physiological condition

In this case, we apply our scheme to model blood flow under physiological conditions. We consider blood flow in a 2D straight, uniform channel representing a section of a common carotid artery, and with the assumption of axial symmetry, we solve for upper half of the domain. For the inflow and outflow boundary conditions we use physiological pressure waves taken from [65], assuming that the pressure waveform is periodic. We perform computations for several cardiac cycles starting from the homogeneous initial conditions, until a time-periodic solution is achieved. A mesh consisting of 4800 tetrahedral cells was created for the fluid and structure domains.

Our choice of parameters used in this example falls within the range of physiological values for blood flow and is reported in Table 5. The wall viscosity constant obtained from [71] for carotid artery was used for viscoelastic model simulations. This choice of viscoelastic parameters has also been used in other references [65, 74] and is well within the range of measured viscous moduli of blood vessels reported in [60]. In order to assess the impact of

viscous modulus on the energy dissipation and compare our work with [54, 55], we perform an additional simulation using $\eta = 1 \times 10^4$ dyne.s/cm² for pulmonary artery obtained from [75].

Table 5. Physical and numerical parameters for benchmark problem 2

Parameters	values	Parameters	values
Radius (cm)	0.3	storativity , s_0 (cm ² /dyne)	5×10^{-6} [24, 35]
Length (cm)	10	Hydraulic cond., k (cm ³ s/g)	5×10^{-12} - 5×10^{-9} [76]
Wall thickness (cm)	0.07		
Wall density(g/cm ³)	1.1	Biot-Willis constant, α	1
Fluid density (g/cm ³)	1	γ_f, γ_s	2500
Dynamic viscosity (poise)	0.035	η (dyne.s/cm ²)	$10^4 - 3 \times 10^4$
Lame coeff. λ_p (dyne/cm ²)	4.28×10^6	Final time	1sec(each cycle)
Lame coeff. μ_p (dyne/cm ²)	1.07×10^6	Time step Δt	10^{-4} sec

For the hydraulic conductivity we consider a range of admissible values. The lower bound represents the behavior of a healthy artery, while the upper bound is applicable to the case of injured endothelium, since the dilated, damaged or inflamed arterial wall has higher permeability (and therefore higher hydraulic conductivity) [77, 78]. More precisely, the value of the hydraulic conductivity $k = 5 \times 10^{-12}$ cm³ s/g has been used in several publications [76, 79-81] for modeling the arterial wall, but we have also tested the higher value for hydraulic conductivity $k = 5 \times 10^{-9}$ cm³ s/g, obtained from [76], which corresponds to intraluminal thrombosis .

3.4.3 Energy balance analysis

Figure 16 shows the distribution of the total input energy of the viscoelastic model in the second and third cycle, with viscous coefficient $\eta=3 \times 10^4$ dyne.s/cm². The analysis of Figure 16 shows that the periodicity of blood flow is verified, because elastic and kinetic energies initial and final values at each cycle almost coincide. In addition, it shows that the energy estimate (3.19) is accurately satisfied in the computations, because the right hand side of (3.19) denoted by E_{tot} and the total energy input to the system, namely, the left hand side of (3.19) are almost equivalent. More precisely, energy balance for a periodic cycle states that the net input work done on the system is equal to the energy losses for each constitutive model. Losses arise from the action of energy dissipation, due either to blood viscosity, filtration exchange, or wall viscoelasticity. Namely at the end of each cycle, (3.19) can be written as:

$$\begin{aligned}
& \int_0^t \int_{\Omega_f(s)} 2\mu_f \|D(v)\|^2 + \int_0^t \int_{\Omega_p(s)} \eta \|D(\dot{U})\|^2 + \int_0^t \int_{\Omega_p(s)} \frac{\eta}{2} \|\nabla \cdot \dot{U}\|^2 \\
& + \int_0^t \int_{\Omega_p(s)} k^{-1} \|q\|^2 \\
& = - \int_{\Gamma_f^{in}} p_{in}(t) v_f \cdot n_f - \int_{\Gamma_f^{in}} p_{out}(t) v_f \cdot n_f \\
& + \left\{ - \int_0^t \int_{\Gamma_f^{in}} \rho_f \frac{\|v\|^2}{2} v \cdot n_f - \int_0^t \int_{\Gamma_f^{out}} \rho_f \frac{\|v\|^2}{2} v \cdot n_f \right\}
\end{aligned} \tag{3.28}$$

We observe from Figure 16 that, for the viscoelastic model, there is only 2.5% discrepancy between the left and right hand sides of (3.28). This confirms the accuracy of our numerical scheme in approximating the energy balance.

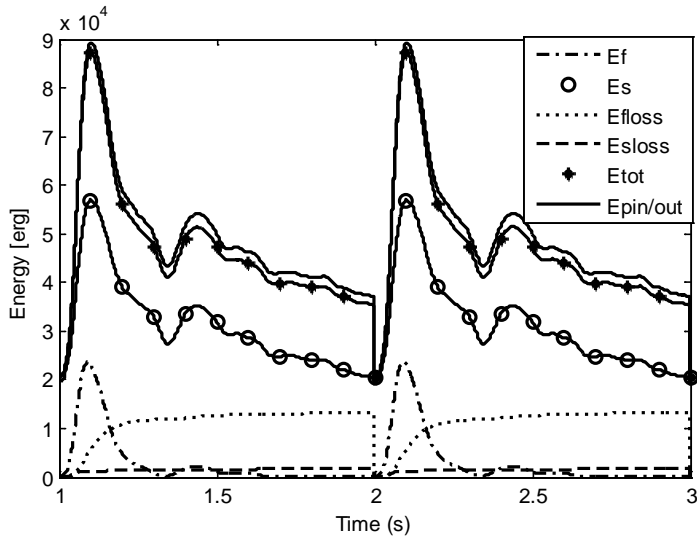
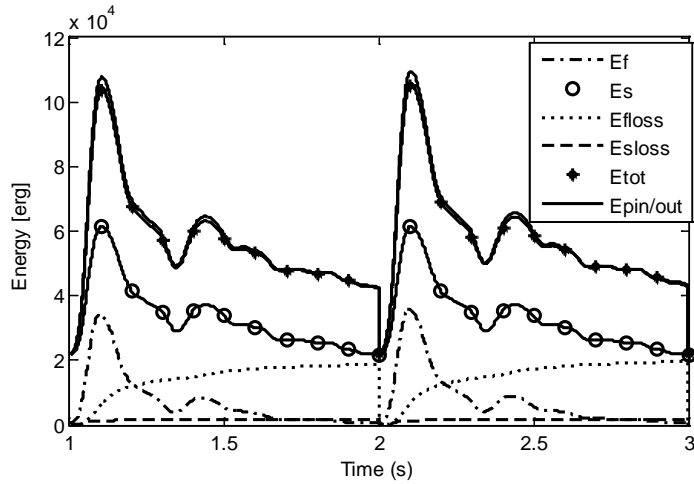


Figure 16. Time evolution of energy components for viscoelastic case with $\eta = 3 \times 10^4$ dyne.s/cm²; The plot shows kinetic and stored energy in wall (circle), fluid kinetic energy (dash-dot line), fluid viscous dissipation (dotted line), wall viscoelastic loss (dashed line), total energy (star), and total input energy to the system (solid line); for the straight tube (top panel) and stenosed tube (bottom panel)

Using energy data obtained similarly for elastic and poroelastic model simulations, we calculate the different energy components for the poroelastic, viscoelastic and elastic cases at three different times. The choice of the snapshot times is shown in Figure 12. The first time interval, from [0-0.1] sec, is called systole phase. The second phase, called early diastole, is between [0.1-0.5] sec, and the last interval, from [0.5-0.9] sec, is called late diastole.

Plots in Figure 17 compare the energy distribution among kinetic energy, stored energy and losses for the elastic, viscoelastic and poroelastic models at these three snapshot times. The results in Figure 17 show that at systole all losses are small and the artery behaves nearly as an elastic structure for all models. The wall elastic energy stored in the arterial walls is the predominant component of the energy in the system, which drives blood flow during diastole. In early diastole phase, energy losses in fluid are significant. The viscoelastic loss is small compared to the flow, while intramural flow is non non-negligible for the higher hydraulic conductivity value. In the late diastole phase, the dissipation predominates and most of the energy is dissipated in overcoming the viscous resistance of blood flow. For small permeability values, we barely notice any contribution related to intramural filtration. We also observe that the energy dissipated in the wall is a small fraction of that dissipated by the blood. Our results for predicted energy distribution are coherent to those of [54]. By defining total dissipation as the sum of fluid the viscous dissipation and the viscoelastic loss at the end of one cycle, our calculations show that 93% of total dissipation takes place in the in blood flow and only 7% of it is related to the vascular wall.

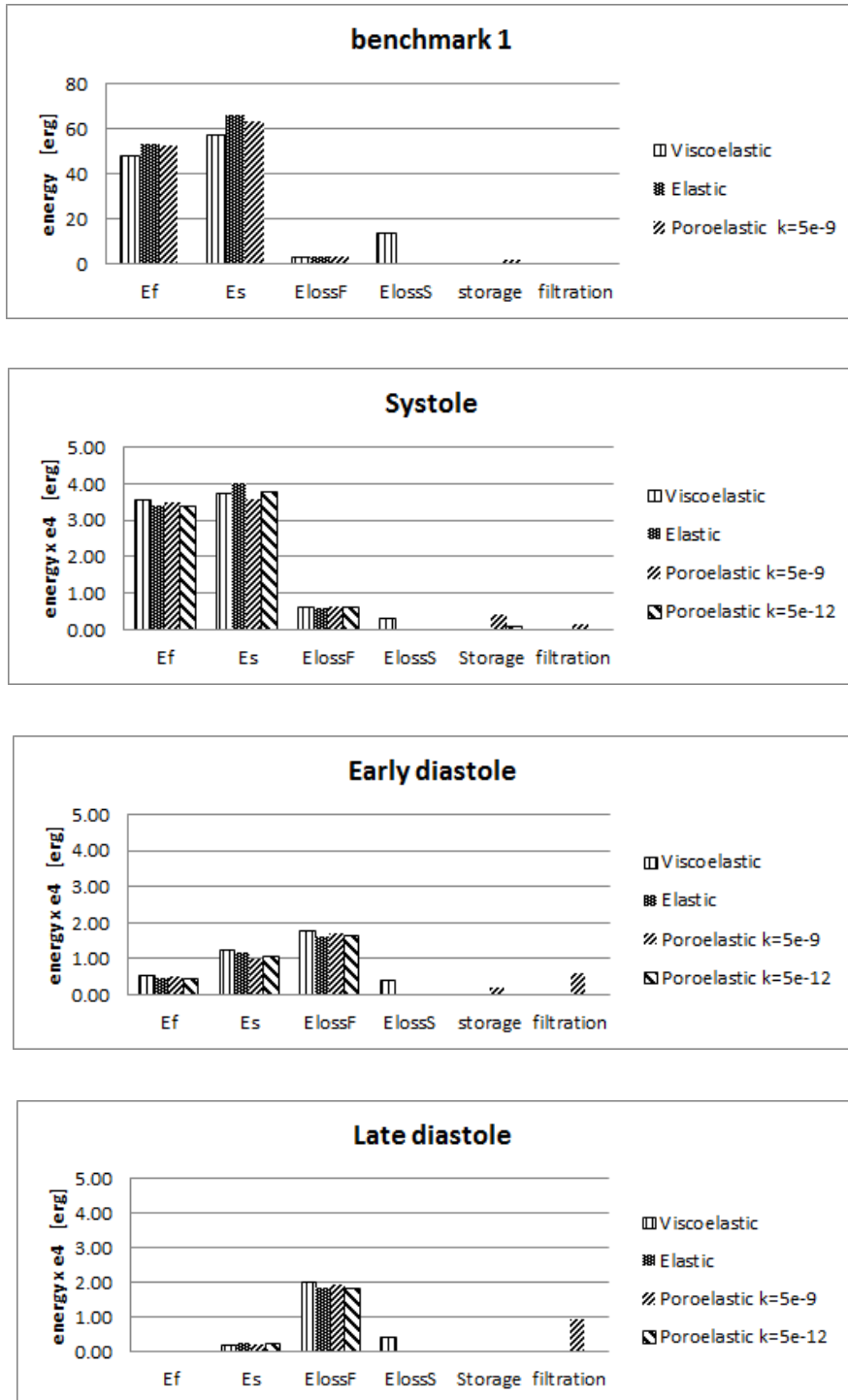


Figure 17. Available energy at the final time (5ms) in each component for different constitutive models in benchmark problem 1 (first plot from top); energy distribution at the snapshot times for elastic, viscoelastic ($\eta=3 \times 10^4$ dyne.s/cm²) and poroelastic models.

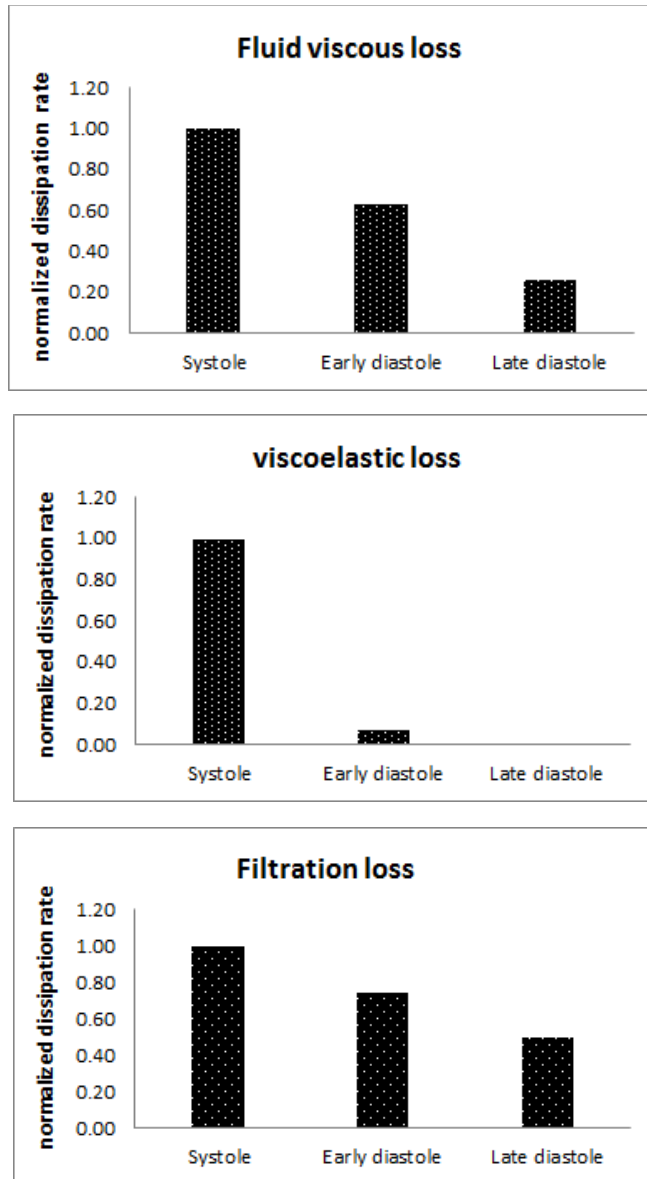


Figure 18. Energy dissipation rate (relative to systole) for viscous loss (top), viscoelastic loss (middle) and filtration energy loss (bottom) during one heart cycle.

In [54] it is estimated that 97% of dissipation relates to the blood flow and 3% to the vascular wall. The discrepancy between our results and the ones in [11] might be due to the difference in geometry or in the pressure drop. Since we use a smaller pressure drop and a smaller artery than in [54] we expect that in our case the arterial wall will weigh more in the

energy balance. To validate the robustness of the method with respect to geometries different than a straight tube, we consider a variation of this benchmark case consisting of a mildly stenosed artery (see Figure 16 for a representation of the domain). For this case, the results of simulation for time evolution of energy components is shown in bottom panel of Figure 16. The similarity of these results with the ones obtained in the case of straight tube suggests that the conclusions of this work remain qualitatively valid also for more general configurations of the computational domain.

Starting from the data of Figure 16, we quantify the rates of energy dissipation. Figure 18 informs us about the rate of energy loss in one heartbeat. For each source of energy dissipation (e.g. viscous dissipation in Figure 18(a), viscoelastic dissipation (b) and intramural filtration (c)), we define rate of energy loss as the total amount of dissipation over a period of time, divided by the time interval. Furthermore, we renormalize the dissipation rates by the value obtained in systole.

In Figure 18 we see that for fluid viscous dissipation rate, the major contribution is in systole. The contributions of the second and third interval are less significant, because fluid velocity and velocity gradient are small. Since the highest acceleration of the arterial wall take place in systole, it plays a key role also in generating viscoelastic loss (middle plot), while the contributions of two other intervals are almost negligible. The results in Figure 18 (bottom plot) show that energy flow to intramural filtration is more uniformly distributed among the heartbeat phases. This behavior can be interpreted observing that the intramural flow energy depends on the filtration velocity (q), which is more persistent during the cardiac cycle. It should be noted that in the energy distribution plots the total amount of energy dissipation in systole is the smallest with respect to the other parts of the heart cycle. The discrepancy between energy

dissipation and its rate of variation can be explained observing that the energy dissipation is cumulative and results from a gradual building up proportional to the total duration of each phase. As a result, it is lower at systole (the shortest time interval) compared to diastole.

3.4.4 Viscoelastic model analysis

Viscoelasticity causes time lag between pressure wave and arterial wall displacement. When a cyclically varying stress is applied to a material, the resulting strain stays in phase if the material is purely elastic. However, if it has viscoelastic properties the strain lags behind the stress. This lag corresponds to generating a hysteresis loop, which is the indicator of the energy loss. The area between ascending and descending parts of the loop quantifies the magnitude of hysteresis and corresponds to the energy dissipation due to the viscous properties of the arterial wall.

Figure 19 (left panel) shows time lag between normalized pressure and radial displacement for different values of the wall viscous modulus in the viscoelastic model. The phase lag is a measure of the amount of viscous damping that takes place in the vessel wall during each cycle. The viscoelastic effect is also visible in the pressure-displacement relationship of the arterial wall shown in Figure 19 (right panel). This plot visualizes the hysteresis effects related to the viscoelastic behavior of the artery. The viscoelastic hysteresis loop obtained by our numerical simulations is in reasonable quantitative agreement with the published in-vivo data of the human common carotid artery [65, 74]. To quantify the hysteresis behavior one can calculate the Energy Dissipation Ratio (EDR), which is a measure of the area inside the pressure-displacement loop relative to the measure of areas inside and under the loop (see [65] for details).

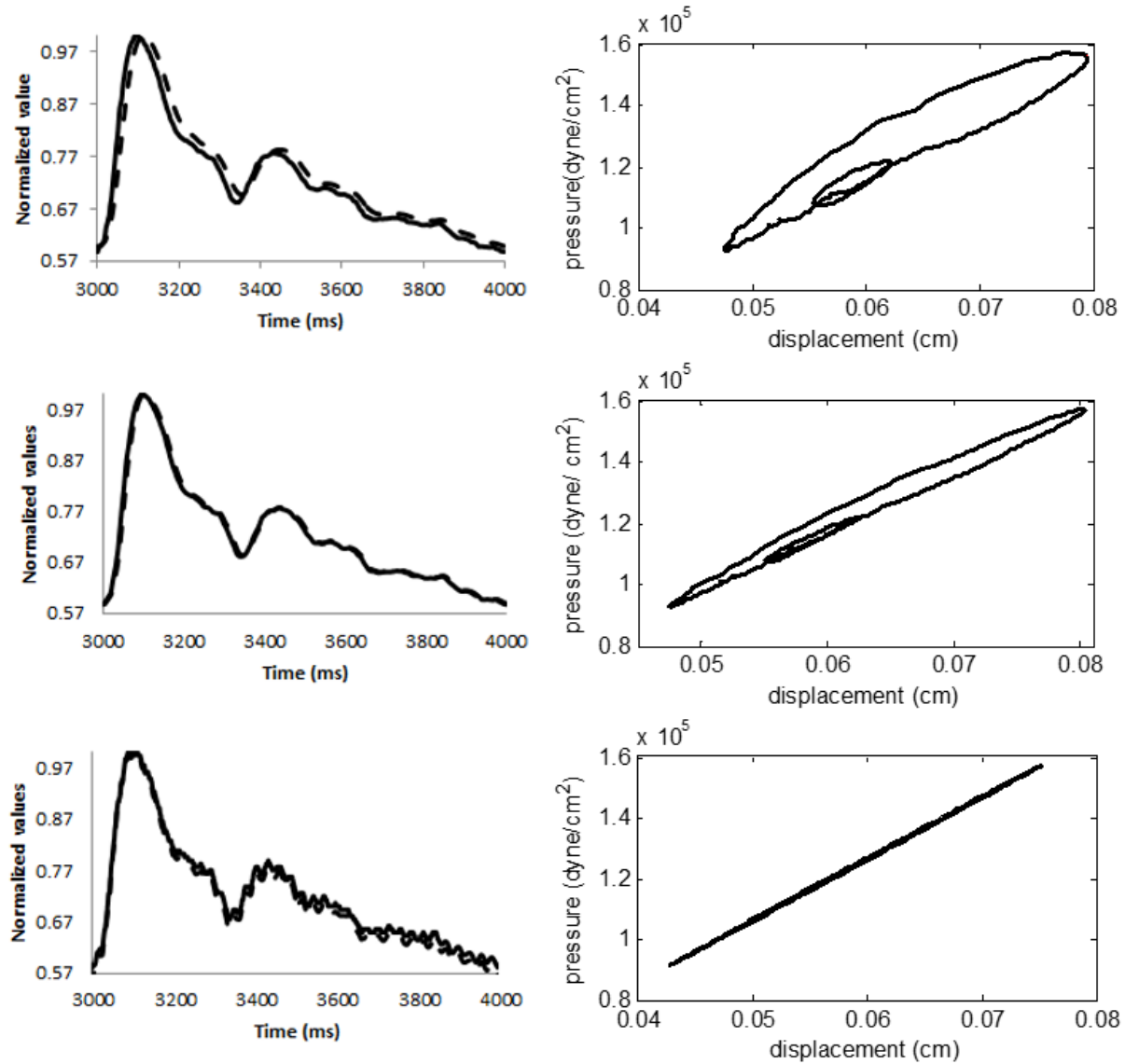


Figure 19. Time lag in viscoelastic model between normalized pressure in the channel (solid line) and normalized wall radial displacement (dashed line) at the midpoint of the channel for different values of wall viscous modulus , $\eta = 3 \times 10^4$ dyne.s/cm² (top), $\eta = 1 \times 10^4$ dyne.s/cm² (middle), and poroelastic model (bottom) are shown in left panel, corresponding hysteresis plots for each case obtained by plotting the fluid pressure at the center of the channel versus the radial wall displacement are provided in right panel.

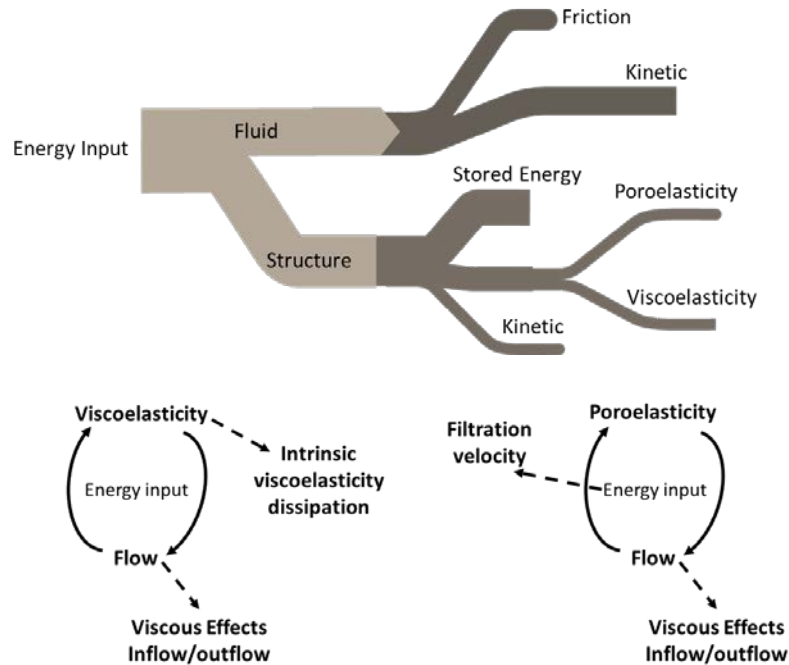


Figure 20. Analysis of energy flow (top); Energy diagram in poroelastic and viscoelastic models (bottom)

From the data reported in Figure 19, we calculated wall energy dissipation rate of 9.4% compared to 8.5% in [74] and 7.8% in [65] for $\eta=3\times 10^4$ dyne.s/cm², suggesting an slightly overestimation in our calculated dissipation rate. These effects are compared to the hysteresis of the poroelastic model (bottom right). Our model suggests that poroelasticity does not generate any hysteresis, under physiological conditions. On one hand, this analysis confirms that incorporating the viscoelastic effects into the model is necessary for the accurate representation of the phase delay between the pressure and radial wall displacement. Moreover, it shows that walls with higher viscoelasticity have larger hysteresis loop. On the other hand, we observe that poroelasticity does not introduce any hysteresis effects.

3.4.5 Poroelastic Model Analysis

The poroelastic model enables us to study the filtration velocity and therefore coupling blood flow with mass transport is a potential application of this model. However, we should consider that for the range of permeability values of healthy arteries, considering intramural filtration is significant only when we look at the problem over long time scales. Indeed, in benchmark problem 2 we barely see any effect for poroelasticity when comparing it to the elastic one. For larger values of permeability, our results confirm that the poroelastic model appreciably changes the displacement and wave propagation speed in structure as well as the energy distribution. Figure 15 reports the results of a simulation is performed using $k=5\times 10^{-6}$ cm³/s/g which is 1000 times larger than its value provided in Table 4. We observe that increasing hydraulic conductivity for short time simulation (benchmark problem 1) affects energy exchange. Our results show that we do not observe hysteresis loops when a poroelastic constitutive law is applied to the artery. Hysteresis is an outcome of the fact that some part of the stored energy gets dissipated into a change of natural configuration of the material and cannot be recovered. Our results confirm that, since for small deformations poroelasticity is a linear model, it only transforms energy from one kind to another, which is in particular the term related to intramural flow. Hence, poroelasticity does not contribute to hysteresis in the pressure-diameter relationship. A sketch of the different behavior of poroelastic and viscoelastic models is shown in Figure 20. The results by Taber in [59] stated that theoretical hysteresis loop for poroelastic materials exist, although they are small. However it should be noted that the results in [59] are based on a nonlinear elasticity formulation for large deformations. Hence, we hypothesize that large deformations and nonlinear material behavior enhance the effect of poroelasticity. Also Taber's results are based on strain dependent permeability. Thus, another possible explanation is

that since during large deformation the tissue permeability changes significantly, poroelastic effects are playing a more relevant role, while at low strain the elastic response dominates.

3.5 SUMMARY

The assumption of negligible viscoelastic and poroelastic response has been routinely made in the analysis of cardiovascular fluid dynamics. This paper presents fluid–structure interaction simulations incorporating different constitutive models for vascular tissue to assess the importance of this simplification. By applying the fluid–structure interaction model to an idealized (carotid) artery under pulsatile flow, we have demonstrated its capability of predicting the poroelastic and viscoelastic wall behaviors. The results indicate that in physiological conditions poroelasticity barely affects the energy distribution of an arterial segment. Since soft tissues are biphasic materials, with water comprising the majority of the weight, poroelasticity may be an important mechanism at longer time scales. Poroelasticity cannot reproduce hysteresis, but it transforms energy of the fluid into intramural flow. Viscoelasticity is responsible for hysteresis and changes the pressure wave propagation. Being directly derived from the fundamental laws of flow and energy, the model relies on general foundations and it is prone to be extended in different directions. For example, we are currently generalizing the problem formulation based on linear elasticity to finite elasticity, which enables us to account for large deformations. This improvement will be also combined with the application of patient specific geometries to this analysis. I extracted this chapter with permission of Springer from the paper: " computational analysis of energy distribution of coupled blood flow and arterial deformation ", and my collaborators for this paper were M. Bukac and P. Zunino.

4.0 NONLINEAR MODEL FOR FPSI

The main contribution of this chapter is the development of a nonlinear poroelastic structural model in the context of fluid-porous structure interaction. The general idea is to use this model to study the influence of different parameters on energy dissipation in a poroelastic medium.

Most of the papers focused on nonlinear elasticity for FSI problems, have used monolithic scheme for solving FSI system in nonlinear case, with some kinds of preconditioners [82, 83]. In [82] the authors studied finite elasticity for interaction between blood flow and elastic arterial wall using a monolithic approach. The design of partitioned algorithms for uncoupling the solution of the three sub-problems in the interaction between pulsatile flow and poroelastic material (FPSI) is still partially unexplored. In [84], the authors investigate the FPSI problem for a viscous fluid and a thick poroelastic structure with small displacement. In our previous works [8, 27-30] a loosely coupled scheme have been successfully developed and analyzed for this problem.

To the best of our knowledge, the only previous work in the direction of modeling fluid-porohyperelastic structure interaction can be found in [5], where the interaction between blood flow and porohyperelastic arterial model is coupled with mass transport analysis. The present study attempts to investigate the interaction of blood flow with a porohyperelastic vessel wall and analyze the role of extracellular fluid flow in the apparent viscoelastic behavior of the arterial wall. The main novelties are in the design of a Nitsche's splitting strategy, which

separates the fluid from the structure sub-problems for FPSI system undergoing large deformations, and in the fact that we also study a new benchmark test specifically designed to investigate the effect of poroelasticity on large deformations.

Many modeling and computational difficulties arise in the numerical simulation of an incompressible fluid interacting with a poroelastic structure featuring possibly large deformations. The complex interplay among large solid deformations and fluid flow in a dynamic setting have been addressed in this study by using porous media theory combined with advanced computational tool for FSI. We use finite elements for the spatial approximation and Backward Euler time stepping for time discretization. Since the model is complex, efficiency of the scheme is a fundamental issue. To reduce the computational cost, the coupled problem is split among its components and solved using a partitioned approach. We adopt a moving mesh algorithm, based on Arbitrary Lagrangian Eulerian (ALE) method. There exist a variety of methods to include the effect of the moving wall in computations, the most prevalent being the arbitrary Lagrangian–Eulerian (ALE) approach. Applications of ALE method to hemodynamics are discussed in [51-53] and references therein. Discretization using finite elements leads to a system of non-linear equations. For this reason, we also discuss the strategy of linearizing such system of equations by the Newton’s method. In summary, the general objective can be split into two specific aims: (1) Developing a mathematical model for FPSI with large deformations and (2) Defining a numerical approximation scheme for the problem at hand.

We use the computational model to perform numerical experiments of FPSI. The numerical experiments are designed to elucidate the dynamic response of a poroelastic material under a variety of loading conditions. Our objective is exploring in what condition poroelastic model is dissipative and examining the range of model parameters that generate a pressure

relaxation loop in FPSI. In our previous paper [30] we suggested that poroelastic effects alone cannot justify hysteresis. More precisely, we observed that poroelasticity does not contribute to any loop in pressure-diameter relation for small deformation model. However, In [59] Taber examined the role of extracellular fluid flow in the apparent viscoelastic behavior of cardiac muscle and results by Taber stated that theoretical hysteresis loop for poroelastic material in myocardium exists, although they are small. Taber extended the formulation based on consolidation theory in [85], to study deformation of porous elastic plates and shells saturated with a viscous fluid, undergoing large axisymmetric deformation. The results in Taber's paper are based on finite elasticity formulation for large deformation. So we hypothesize that large deformation behavior or loading conditions may enhance the effect of poroelasticity.

There is very little information on how energy loss (hysteresis etc.) depends on the rate of loading or of deformation. The relative contributions of the fluid-solid phase effects (poroelasticity) and intrinsic solid phase viscoelasticity to this behavior are not known. An understanding of the nature of these contributions may be used to design implants that behave more physiologically over a broad range of applied frequencies. One good example is the intervertebral disc. In [86], the authors measured the frequency-dependent stiffness and energy absorption of human lumbar intervertebral discs to determine whether these properties differ due to fluid-flow dependent behavior.

This chapter is organized as follows. Section 4.1 deals with the description of constitutive framework for FSI problem at finite strains, namely we first consider the fluid and the structure as a continuous medium and discuss the governing equations in the fixed configuration. Then we split the domain into two parts and explore the structure domain in a Lagrangian description by imposing the conservation laws in the reference configuration and using an arbitrary Lagrangian

Eulerian (ALE) formulation to describe the fluid domain. In Section 4.2, the partitioned algorithm used to solve the fully discrete FSI problem is presented. In Section 4.3, we propose numerical simulations on two benchmark problems and discuss the relevant numerical results obtained.

4.1 FORMULATION

We consider a continuous medium, which occupies a moving domain $\Omega(t)$ in its current configuration. It is made of a fluid in motion in the region $\Omega_f(t)$ and a deformable structure $\Omega_s(t)$ and we have $\Omega_f(t) \cup \Omega_s(t) = \Omega(t)$. The problem consists in finding the time evolution of the domain and the velocity fields within the fluid and the structure.

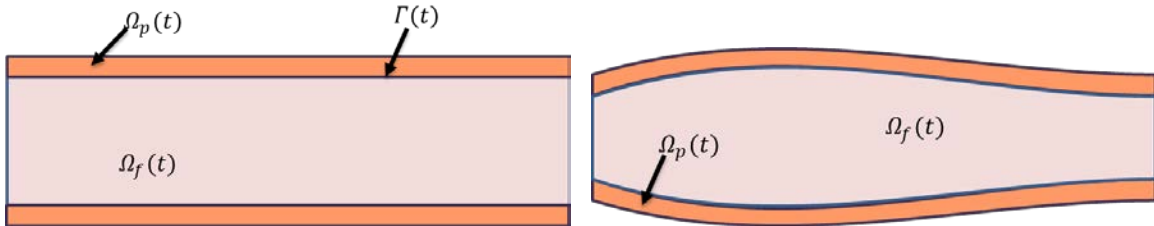


Figure 21. Geometric configuration, reference (left) and present (right)

For this purpose, we use the fundamental conservation laws of continuum mechanics written on the present configuration $\Omega(t)$, namely conservation of mass and conservation of linear momentum. Here in these equations, U_D is the velocity field at any point of the continuum, $\int_{\Omega(t)} \rho b \, dv$ defines net body forces and $\int_{\partial\Omega(t)} t \, da$ is the net surface forces on the surface $\partial\Omega(t)$.

We set the following equations for mass and momentum balance:

$$\begin{aligned} \frac{d}{dt} \int_{\Omega(t)} \rho \, dv &= 0 \\ \frac{d}{dt} \int_{\Omega(t)} \rho U_D \, dv &= \int_{\Omega(t)} \rho b \, dv + \int_{\partial\Omega(t)} t \, da \end{aligned} \tag{4.1}$$

For conservation of momentum it can be written using Cauchy stress definition and divergence theorem as:

$$\frac{d}{dt} \int_{\Omega(t)} \rho U_D \, dv = \int_{\Omega(t)} \rho b \, dv + \int_{\Omega(t)} \nabla \cdot (\sigma) \, da$$

If we ignore body forces and by using Reynolds transport theorem:

$$\frac{d}{dt} \int_{\Omega_f(t)} f \, dv = \int_{\Omega_f(t)} \left(\frac{\partial f}{\partial t} + \nabla \cdot (f U_D) \right) \, dv$$

We can write conservation equations as following:

$$\begin{aligned} \int_{\Omega(t)} \frac{\partial \rho}{\partial t} + \nabla \cdot (\rho U_D) &= 0 \\ \int_{\Omega(t)} \frac{\partial \rho U_D}{\partial t} + \nabla \cdot (\rho U_D \otimes U_D) - \int_{\Omega(t)} \nabla \cdot \sigma &= 0 \end{aligned} \tag{4.2}$$

Where \otimes is the tensor product or the dyad of vectors u and v denoted by $u \otimes v$. Because of the large displacements, the configuration $\Omega(t)$ is time dependent. To overcome this difficulty, and to evaluate the strain field or write the elastic constitutive laws inside the structure, it is very convenient to transport the conservation laws on a fixed configuration $\hat{\Omega}$. For this purpose, one must introduce a continuous mapping T which maps any point x_0 of the fixed configuration $\hat{\Omega}$ to its image $x(x_0, t)$ in the present configuration $\Omega(t)$. The choice of the configuration Ω_0 and the map T may be arbitrary; hence the name of ALE formulation is given to the resulting equations. To simplify the calculation, it is advisable to choose a material configuration for the structural

part of the domain. In other words, on Ω_s the point $x(x_0, t)$ corresponds to the present position of the material point which was located in x_0 at time t . this implies then that the configuration (or grid) velocity is always equal to the real velocity of the structure in any point of Ω_s .

$$\frac{\partial x}{\partial t} |_{x_0} = w$$

The conservation laws on $\Omega(t)$ can now be directly transported on the fixed domain by Piola identity and with Reynolds transport theorem using the following transport equations [87]:

$$\begin{aligned} \int_{\Omega(t)} \nabla \cdot (A \otimes U_D) d\Omega &= \int_{\hat{\Omega}} \hat{\nabla} \cdot (JA \otimes U_D \cdot F^{-T}) d\hat{\Omega} \\ \int_{\Omega(t)} \frac{\partial A}{\partial t} d\Omega &= \int_{\hat{\Omega}} \frac{\partial AJ}{\partial t} - \hat{\nabla} \cdot (J \cdot A \otimes U_D \cdot F^{-T}) d\hat{\Omega} \end{aligned} \quad (4.3)$$

Here, F is the deformation gradient and $J = \det(F)$. Applying formulas (4.3) that is also provided in [4], to the original conservation laws (mass and momentum) reduces them to the global ALE conservation laws, written on the fixed configuration Ω_0 . It should be noted that if $w = U_D$ we get the Eulerian description and if $w = 0$ we get the Lagrangian description.

$$\begin{aligned} \int_{\hat{\Omega}} \frac{\partial \rho_0}{\partial t} |_{x_0} + \hat{\nabla} \cdot (\rho_0 (U_D - w)) \cdot F^{-T} &= 0 \quad \text{mass} \\ \int_{\hat{\Omega}} \frac{\partial \rho_0 U_D}{\partial t} |_{x_0} + \hat{\nabla} \cdot (\rho_0 U_D \otimes (U_D - w)) \cdot F^{-T} - \int_{\Omega_0} \hat{\nabla} \cdot P &= 0 \quad (4.4) \\ \int_{\hat{\Omega}} \frac{\partial \rho_0 U_D}{\partial t} |_{x_0} + \hat{\nabla} \cdot (\rho_0 U_D \otimes (U_D - w)) \cdot F^{-T} - \int_{\hat{\Omega}} \hat{\nabla} \cdot (J \sigma F^{-T}) &= 0 \quad LM \end{aligned}$$

In this chapter, we consider the flow in a compliant channel bounded by a thick wall, with a two way coupling between the fluid and the structure. In the next section, we describe the governing equations for each domain.

4.1.1 Fluid model in the ALE form

We assume that the vessel is sufficiently large so that the non-Newtonian effects can be neglected. The fluid is modeled as an incompressible, viscous, Newtonian fluid using the Navier-Stokes equations, i.e., the equations describing conservation of mass and momentum.

$$\int_{\hat{\Omega}} \frac{\partial \rho_0}{\partial t} |_{x_0} + \widehat{\nabla} \cdot (\rho_0 (v - w)) \cdot F^{-T} = 0$$

$$\int_{\hat{\Omega}} \frac{\partial \rho_0 v}{\partial t} |_{x_0} + \widehat{\nabla} \cdot (\rho_0 v \otimes (v - w)) \cdot F^{-T} - \int_{\hat{\Omega}} \widehat{\nabla} \cdot (J \sigma F^{-T}) = 0$$
(4.5)

In these expressions it is simpler to compute the partial time derivatives on the fixed reference configuration and all other stress terms on the present configuration. These equations are a particular case of the ones presented in section 2.1. They are obtained by replacing U_D by v , that denotes here the velocity of the fluid.

We recall that $\rho_0 = J \rho_f$,

Therefore, we can write the first equation in (4.5) as:

$$\int_{\hat{\Omega}} \frac{\partial J \rho_f}{\partial t} |_{x_0} + \widehat{\nabla} \cdot (J \rho_f (v - w)) \cdot F^{-T} = 0$$

We compute the partial time derivative on the fixed reference configuration. Using transport equations (4.3), and since $J = dx/d\hat{x}$:

$$\begin{aligned} \int_{\hat{\Omega}} \frac{\partial J \rho_f}{\partial t} |_{x_0} + \widehat{\nabla} \cdot (J \rho_f (v - w)) \cdot F^{-T} &= \int_{\hat{\Omega}} \frac{\partial J \rho_f}{\partial t} |_{x_0} + \int_{\hat{\Omega}} \widehat{\nabla} \cdot (J \rho_f (v - w)) \cdot F^{-T} \\ &= \int_{\hat{\Omega}} \frac{\partial J \rho_f}{\partial t} |_{x_0} + \int_{\Omega_f(t)} \nabla \cdot (\rho_f (v - w)) \\ &= \int_{\Omega_f(t)} J^{-1} \frac{\partial J \rho_f}{\partial t} |_{x_0} + \int_{\Omega_f(t)} \nabla \cdot (\rho_f (v - w)) \end{aligned}$$

By applying same procedure to the second equation in (4.5) ,we finally have:

$$\int_{\Omega_f(t)} J^{-1} \frac{\partial J \rho_f}{\partial t} |_{x_0} + \nabla \cdot (\rho_f (v - w)) = 0 \quad (4.6)$$

$$\int_{\Omega_f(t)} J^{-1} \frac{\partial J \rho_f v}{\partial t} |_{x_0} + \nabla \cdot (\rho_f v \otimes (v - w)) - \int_{\Omega_f(t)} \nabla \cdot (\sigma_f) = 0$$

Here w is the velocity of the mesh, required to deform the fluid mesh in a way that it matches structure mesh always. After integration by part, the above ALE formulation of the fluid problem takes the form of the following PDE:

$$J^{-1} \frac{\partial J \rho_f v}{\partial t} |_{x_0} + \nabla \cdot (\rho_f v \otimes (v - w) - \sigma_f) = 0 \quad in \Omega_f(t)$$

Taking into account mass conservation, one can also reduce this equation to the non-conservative form. This is the fluid model, namely the Navier-Stokes equation in ALE form, is written as:

$$\rho_f \left(\frac{\partial v}{\partial t} + (v - w) \cdot \nabla v \right) = \nabla \cdot \sigma_f \quad in \Omega_f(t) \quad (4.7)$$

$$\nabla \cdot v = 0 \quad in \Omega_f(t) \quad (4.8)$$

Here v and ρ_f stand for fluid velocity vector field and fluid density, respectively, and $\sigma_f = -p_f I + 2\mu_f D(v)$ is the fluid Cauchy stress tensor where p_f is fluid pressure, μ_f is fluid dynamic viscosity and the symmetric part of fluid velocity gradient is defined as $D(v) = \frac{1}{2}(\nabla v + \nabla v^T)$.

4.1.2 Lagrangian formulation of the structure model

Since the fixed configuration $\hat{\Omega}$ is also the fixed configuration for structure, the structure velocity is equal to the material velocity on the structure domain and we have $\dot{U} = w$ on $\hat{\Omega}_s$

Based on this result, the conservation laws for structure part of the domain simply reduce to the following:

$$\begin{aligned} \frac{\partial \rho_0}{\partial t} |_{x_0} &= 0 \quad \text{on } \hat{\Omega}_s \\ \rho_s \frac{\partial^2 U}{\partial t^2} - \widehat{\nabla} \cdot (P) &= 0 \quad \text{in } \hat{\Omega}_s \end{aligned}$$

Here, σ is the Cauchy stress tensor, F is the deformation gradient and “ $\widehat{\nabla}$ ” is the nabla operator with respect to the material with respect to the material coordinates in the reference domain. P is the first Piola stress defined as $P = J\sigma F^{-T}$. Using the relationship $\sigma = J^{-1}FSF^T$ between Cauchy stress and 2nd Piola stress tensor S , the model for elastic wall in Lagrangian/reference configuration $\hat{\Omega}_s$ is:

$$\begin{aligned} \rho_s \frac{\partial^2 U}{\partial t^2} - \nabla \cdot (J\sigma F^{-T}) &= 0 \\ \rho_s \frac{\partial^2 U}{\partial t^2} - \nabla \cdot (J(J^{-1}FSF^T)F^{-T}) &= 0 \\ \rho_s \frac{\partial^2 U}{\partial t^2} - \nabla \cdot (FS) &= 0 \quad \text{on } \hat{\Omega}_s \end{aligned}$$

We use the St. Venant-Kirchhoff hyperelastic constitutive model for the solid matrix for which the strain energy function is:

$$W = \frac{\lambda_p}{2} \text{tr}(E^2) + \mu_p E:E \quad (4.9)$$

This yields following expression for 2nd Piola stress tensor, where second order tensor I is the Kronecker delta function and $E(U)$ denotes Green strain tensor.

$$S = 2\mu_p E(U) + \lambda_p \nabla \cdot U I \quad , \quad E(U) = \frac{1}{2} (\nabla U + \nabla U^T + (\nabla U) \nabla U^T)$$

To express the filtration flow as well as pressure gradient in the wall, we model the structure as a saturated porohyperelastic material according to the mixture theory. To model the poroelastic properties of the structure domain, Biot's theory [24, 35] is employed. This formulation assumes that the porous material is constructed so that the solid phase forms an elastic structure that contains statistically distributed small pores filled with a Newtonian-viscous compressible fluid. The bulk material is assumed to be homogeneous on a macroscopic scale, and the pores to be interconnected. This model has also been used in [88], [84] and [89].

We assume that the fluid flow through the porous medium is modeled using the Darcy equation. Hence; the Biot system for a poroelastic material consists of the momentum equation for balance of total forces, Darcy's law and the storage equation for the fluid mass conservation in the pores of the matrix. Therefore, the equations governing the deformation of the saturated poroelastic material are defined as:

$$\rho_p \frac{\partial^2 U}{\partial t^2} - \nabla \cdot (FS - J p_p F^{-T}) = 0 \quad \text{in } \hat{\Omega}_p \quad (4.10)$$

$$k^{-1} q = -\nabla p_p \quad \text{in } \Omega_p(t) \quad (4.11)$$

$$\frac{D}{Dt} (s_0 p_p + \alpha \nabla \cdot U) + \nabla \cdot q = 0 \quad \text{in } \Omega_p(t) \quad (4.12)$$

In equation (4.11), the relative velocity of the fluid within the porous wall is denoted by q and p_p is the fluid pressure. More precisely, q is the relative volumetric flux to the skeleton defined as the velocity of the pore fluid minus velocity of the skeleton, which is termed filtration velocity in the following text. We define ρ_p as the poroelastic structure density. Hydraulic

conductivity of the porous matrix is denoted by k , the coefficient s_0 is the storage coefficient, and the Biot-Willis constant α is the pressure-storage coupling coefficient.

We also use a consistent ‘effective stress’ measure for the solid matrix response where σ^{Sk} is the Cauchy stress tensor of the skeleton, and p_p is the mean pore pressure. σ^P denotes the elasticity stress tensor which is defined as $\sigma^P = \sigma^{Sk} - \alpha p_p I$. The Cauchy effective stress tensor of the skeleton is transformed to the 2nd Piola-Kirchhoff stress tensor S as $S^P = S^{Sk} - J p_p C^{-1}$, where $C = F^T F$.

4.1.3 Coupling conditions over the interface

The fluid and poroelastic structure problems must be coupled by imposing three interface coupling conditions: on velocity, stress, and geometry. Denoting by n_f the outward normal to the fluid domain and by t_f the corresponding tangential vector, the requirements for compatibility and the no-slip condition require the following:

$$v \cdot t_f = \frac{DU}{Dt} \cdot t_f \quad \text{on } \Gamma(t) \quad (4.13)$$

$$v \cdot n_f = \left(\frac{DU}{Dt} + q \right) \cdot n_f \quad \text{on } \Gamma(t) \quad (4.14)$$

$$n_f \cdot \sigma_f n_f = -p_p \quad \text{on } \Gamma(t) \quad (4.15)$$

$$n_f \cdot \sigma_f n_f - n_f \cdot \sigma_p n_f = 0 \quad \text{on } \Gamma(t) \quad (4.16)$$

$$t_f \cdot \sigma_f n_f - t_f \cdot \sigma_p n_f = 0 \quad \text{on } \Gamma(t) \quad (4.17)$$

In Equation (4.13) and (4.14) velocity continuity is enforced across the fluid-solid interface, in particular equation (4.14) describes the continuity of normal flux over the interface, which corresponds to the conservation of mass principle. Balance of the normal components of

stress in the fluid phase gives Equation (4.15). Moreover, for traction continuity, we need to ensure the balance of stresses on the interface. Considering continuity of the both normal and tangential components of stress, is served by conservation of momentum in (4.17) and (4.16).

We also have the kinematic constraint between solid and mesh displacements. It means the velocity of the mesh is able to deform the fluid mesh in a way that it matches structure mesh always.

$$\dot{U} = \frac{DU}{Dt} = w \quad \text{on } \Gamma(t) \quad (4.18)$$

4.2 NUMERICAL PROCEDURE

For fluid-porous-solid interaction, a two-way coupled model must be used, wherein the fluid flow and the solid deformations mutually affect each other. A common approach to dealing with this problem is to separate the two models and solve each one independently by means of an iterative loop. The two algorithms communicate through the coupling conditions on the interface. Solving the separated problems serially multiple times is referred to as a “partitioned approach”. Nitsche’s method has been used for enforcing the interface conditions between non-conforming meshes in the fluid and structure domains. Formulation of Nitsche’s method for a “FSI only” system is provided in [37] and has been applied in a similar manner for FPSI system in [27] for enforcing interface conditions, where the interface conditions (4.13)-(4.17) appear in the variational formulation in a modular form. Therefore, it is straightforward to design a partitioned algorithm to solve each equation of the problem independently using time lagging.

The use of an ALE formulation for the fluid, together with a Lagrangian frame for the structure, yields an FPSI problem that is composed by four subproblems, namely the fluid problem, which allows for the computation of the velocity and pressure inside the fluid domain, the elasticity problem, which describes the deformation of the vessel wall, the Darcy problem, which allows for the computation of the velocity and pressure inside the porous medium and the ALE map update, which accounts for the change in time of the computational fluid domain. The numerical approach is described below in details.

4.2.1 Spatial discretization using finite elements

The coupled fluid/ poroelastic structure problem consists of finding the solution for the velocity and pressure field in fluid domain denoted by (v, p_f) and also the velocity and pressure field in the porous media defined by (q, p_p) as well as displacement and velocity of the wall (U, \dot{U}) . The finite element method (FEM) was applied to solve the coupled system of equations.

We denote with V_h^f, Q_h^f the finite element spaces for the velocity and pressure approximation on the fluid domain Ω_f , with V_h^p, Q_h^p the spaces for velocity and pressure approximation of the porous domain Ω_p and with X_h^p, \dot{X}_h^p the approximation spaces for the structure displacement and velocity, respectively. We assume that all the finite element approximation spaces comply with the prescribed Dirichlet conditions on external boundaries $\partial\Omega_f, \partial\Omega_p$.

Then we define the bilinear forms for each for each sub-problem. To obtain the bilinear form for nonlinear elasticity equation, we use the principle of minimum potential energy. The bilinear form relative to the pure elastic behavior of the structure, namely equation (4.10), is:

$$\begin{aligned}
a_s(U_h, \varphi_{p,h}) &:= \int_{\hat{\Omega}_p} \varphi_{p,h} (-\nabla \cdot (FS)) = \int_{\hat{\Omega}_p} FS : \nabla \varphi_{p,h} = \int_{\hat{\Omega}_p} (I + \nabla U_h) S : \nabla \varphi_{p,h} \\
&= \int_{\hat{\Omega}_p} S : D\varepsilon(U_h)[\varphi_{p,h}] d\hat{x}
\end{aligned} \tag{4.19}$$

Where $D\varepsilon(U_h)[\varphi_{p,h}]$ is the Gateaux derivative of ε at U in the direction of φ_p .

$$D\varepsilon(U_h)[\varphi_{p,h}] = \lim_{\Delta t \rightarrow 0} \frac{\varepsilon(U_h + \Delta t \varphi_{p,h}) - \varepsilon(U_h)}{\Delta t} \tag{4.20}$$

$$D\varepsilon(U_h)[\varphi_{p,h}] = \frac{1}{2} (\nabla \varphi_{p,h} + \nabla \varphi_{p,h}^T + \nabla \varphi_{p,h} \nabla U_h^T + \nabla U_h \nabla \varphi_{p,h}^T)$$

Also we also have:

$$b_s(p_{p,h}, \varphi_{p,h}) := \alpha \int_{\hat{\Omega}_p} J p_{p,h} F^{-T} : (\nabla \varphi_{p,h}) d\hat{x} \tag{4.21}$$

For the Darcy problem in a poroelastic medium we have two other terms, which account for the filtration through the porous matrix, equations (4.11)-(4.12), defined as:

$$a_p(q_h, r_h) := \int_{\Omega_p} \kappa^{-1} q_h \cdot r_h dx, \quad b_p(p_{p,h}, r_h) := \int_{\Omega_p} p_{p,h} \nabla \cdot r_h dx$$

For the flow equations (4.7)-(4.8), the trilinear and bilinear forms are:

$$\begin{aligned}
a_f(v_h, v_h, \varphi_{f,h}) &:= 2\mu_f \int_{\Omega_f} D(v_h) : D(\varphi_{f,h}) dx + \rho_f \int_{\Omega_f} (v_h \cdot \nabla) v_h \cdot \varphi_{f,h} dx, \\
b_f(p_{f,h}, \varphi_{f,h}) &:= \int_{\Omega_f} p_{f,h} \nabla \cdot \varphi_{f,h} dx,
\end{aligned}$$

The forcing term for boundary conditions is:

$$F(t; \varphi_{f,h}) = - \int_{\Gamma_f^{in}} p_{in}(t) \varphi_{f,h} \cdot n_f$$

And finally, the following interface terms appear in the variational equations,

$$I_\Gamma = \int_\Gamma (\sigma_{f,h} n \cdot \varphi_{f,h} - \sigma_{p,h} n \cdot \varphi_{p,h} + p_{p,h} r_h \cdot n) \tag{4.22}$$

Starting from the expression of I_Γ , Nitsche's method allows us to weakly enforce the interface conditions (4.13)-(4.17). Details for interface bilinear form can be found in [35]. Based on the assumption that the solution of the system and the chosen test functions are regular enough, for any $t \in (0, T)$, we have semi-discrete coupled fluid/solid problem as the following equation, considering that $\dot{U}_h^n = d_\tau U_h^n$.

$$\begin{aligned}
& \rho_p \int_{\hat{\Omega}_p} d_\tau \dot{U}_h \cdot \varphi_{p,h} d\hat{x} + \rho_p \int_{\hat{\Omega}_p} (\dot{U}_h - d_\tau U_h) \cdot \dot{\varphi}_{p,h} d\hat{x} + a_s(U_h, \varphi_{p,h}) \\
& + \rho_f \int_{\Omega_f} \partial_t v_h \cdot \varphi_{f,h} dx + s_0 \int_{\Omega_p} D_t p_{p,h} \psi_{p,h} dx - b_s(p_{p,h}, \varphi_{p,h}) \\
& + b_s(\psi_{p,h}, D_t U_h) + a_p(q_h, r_h) - b_p(p_{p,h}, r_h) + b_p(\psi_{p,h}, q_h) \\
& + a_f(v_h, v_h, \varphi_{f,h}) - b_f(p_{f,h}, \varphi_{f,h}) + b_f(\psi_{f,h}, v_h) - \int_\Gamma (\sigma_{f,h} n \\
& \cdot \varphi_{f,h} - \sigma_{p,h} n \cdot \varphi_{p,h} + p_{p,h} r_h \cdot n) = F(t; \varphi_{f,h})
\end{aligned} \tag{4.23}$$

4.2.2 Time discretization

We now address the time discretization. Let Δt denote the time step, $t_n = n\Delta t$, $0 \leq n \leq N$, and let the first order (backward) discrete time derivative be defined as:

$$d_\tau U^n := \frac{U^n - U^{n-1}}{\Delta t}.$$

It should be noted that the difference approximation for time derivative of the wall velocity is obtained using the common three-point second-derivative approximation for the uniform time grid:

$$d_\tau \dot{U}^n := \frac{U^n - 2U^{n-1} + U^{n-2}}{\Delta t^2}.$$

Using the Backward Euler (BE) method for the time discretization of both the flow and the structure problem, the fully discrete coupled fluid-solid problem consists of finding $v_h^n, p_{f,h}^n, q_h^n, p_{p,h}^n \in V_h^f \times Q_h^f \times V_h^p \times Q_h^p$ and $U_h^n \in X_h^p$, at each t_n , such that for any $\varphi_{f,h}, \psi_{f,h}, r_h, \psi_{p,h} \in V_h^f \times Q_h^f \times V_h^p \times Q_h^p$ and $\varphi_{p,h} \in X_h^p$ we have,

$$\begin{aligned}
& \frac{\rho_p}{\Delta t^2} \int_{\hat{\Omega}_p} (U_h^n - 2U_h^{n-1} + U_h^{n-2}) \cdot \varphi_{p,h} \, d\hat{x} + a_s(U_h^n, \varphi_{p,h}) + \rho_f \int_{\Omega_f} \partial_t v_h^n \cdot \varphi_{f,h} \, dx \\
& + s_0 \int_{\Omega_p} D_t p_{p,h}^n \psi_{p,h} \, dx - b_s(p_{p,h}^n, \varphi_{p,h}) + b_s(\psi_{p,h}, D_t U_h^n) \\
& + a_p(q_h^n, r_h) - b_p(p_{p,h}^n, r_h) + b_p(\psi_{p,h}, q_h^n) + a_f(v_h^n, v_h^n, \varphi_{f,h}) \\
& - b_f(p_{f,h}^n, \varphi_{f,h}) + b_f(\psi_{f,h}, v_h^n) - \int_{\Gamma} (\sigma_{f,h}^n n \cdot \varphi_{f,h} - \sigma_{p,h}^n n \cdot \varphi_{p,h} \\
& + p_{p,h}^n r_h \cdot n) = F(t; \varphi_{f,h})
\end{aligned} \tag{4.24}$$

Since both the deformation gradient F and the 2nd Piola stress tensor S in the bilinear form a_s depend on the displacement of the structure U , the finite element discretization leads to a system of non-linear equations. At each iteration, the coupled FSI problem needs to be linearized. The linearization is performed iteratively by the Newton method (similar to the approach used in [90], [7] and [91]).

4.2.3 Structure problem

Given $v_h^{n-1}, p_{f,h}^{n-1}, q_h^{n-1}, p_{p,h}^{n-1}$ find U_h^n in $\hat{\Omega}_s$ such that (4.25):

It should be noted that by considering the equilibrium of stress over the interface namely conditions (4.16) and (4.17), we can replace σ_p with σ_f . Therefore, normal stresses computed

from the fluid iterate at the previous time step will be used to obtain the structure displacement from (4.25).

$$\begin{aligned}
& \frac{\rho_p}{\Delta t^2} \int_{\hat{\Omega}_p} (U_h^n - 2U_h^{n-1} + U_h^{n-2}) \cdot \varphi_{p,h} + \int_{\hat{\Omega}_p} S(\varepsilon(U_h^n)) : D\varepsilon(U_h^n) [\varphi_{p,h}] \\
& + \int_{\hat{\Omega}_p} \xi U_h^n \cdot \varphi_{p,h} + \int_{\hat{\Gamma}} \gamma_f \mu_f h^{-1} d_\tau U_h^n \cdot t_p \varphi_{p,h} \cdot t_p \\
& + \int_{\hat{\Gamma}} \gamma_f \mu_f h^{-1} d_\tau U_h^n \cdot n_p \varphi_{p,h} \cdot n_p - \int_{\hat{\Gamma}} \hat{J}_s \sigma_{f,h}^{n-1} \hat{F}_s^{-T} n_p(\varphi_{p,h}) \\
& = b_s(p_{p,h}^{n-1}, \varphi_{p,h}) + \int_{\hat{\Gamma}} \gamma_f \mu_f h^{-1} v_h^{n-1} \cdot t_p \varphi_{p,h} \cdot t_p \\
& + \int_{\hat{\Gamma}} \gamma_f \mu_f h^{-1} (v_h^{n-1} - q_h^{n-1}) \cdot n_p \varphi_{p,h} \cdot n_p.
\end{aligned} \tag{4.25}$$

This problem is equivalent to solving the elastodynamics equation, where the pressure term has been time-lagged, complemented with the following Robin-type boundary condition on the interface:

$$\sigma_p n_p = \sigma_f^{n-1} n_p - \gamma_f \mu_f h^{-1} \left(\frac{DU}{Dt} - v^{n-1} + q^{n-1} \right) \quad \text{on } \Gamma$$

Or equivalently:

$$\hat{F}_s S \cdot N_p = \hat{J}_s \sigma_f^{n-1} \hat{F}_s^{-T} N_p - \gamma_f (h^{-1}) \mu_f \left(\frac{\partial U}{\partial t} - v^{n-1} + q^{n-1} \right) \quad \text{on } \hat{\Gamma}$$

Where N_p is defined as the normal vector to the structure domain in the reference configuration and, n_p is the equivalent vector in the current configuration.

4.2.3.1 Newton's method

A Newton–Raphson iterative strategy has been adopted here to solve the residual equation through consistent linearization at each time step. In newton method for solving nonlinear elasticity, we define residual as $R = a_s(U, \varphi_p) - L(\varphi_p)$.

$$J \Delta U^k = -f(x^k) \quad \text{where } J = \frac{\partial f^T}{\partial x^k}$$

$$f(x^k) = a_s(U^k, \varphi_p) - L(\varphi_p)$$

$$\frac{\partial f^T}{\partial x^k} \Delta U^k = L[f] = a^*(U^k, \Delta U^k, \varphi_p) \rightarrow U^{k+1} = U^k - \Delta U^k$$

Also we denote the linearization of $a_s(U, \varphi_p)$ as $a_s^*(U, \Delta U, \varphi_p)$:

$$\begin{aligned} a_s^*(U, \Delta U, \varphi_p) &= \int_{\hat{\Omega}_p} \mathcal{C} : D\varepsilon(U)[\varphi_p] : D\varepsilon(U)[\Delta U] \\ &+ S(\varepsilon(U)) : D^2\varepsilon(U)[\varphi_p, \Delta U] \\ &= \int_{\hat{\Omega}_p} \mathcal{C} : D\varepsilon(U)[\varphi_p] : D\varepsilon(U)[\Delta U] \\ &+ \mathcal{C} : \varepsilon(U) : D^2\varepsilon(U)[\varphi_p, \Delta U] \end{aligned} \quad (4.26)$$

The coefficients of the Lagrangian elasticity tensor emerges as:

$$\mathcal{C}_{ijkl} = \lambda_p \delta_{ij} \delta_{kl} + \mu_p (\delta_{ik} \delta_{jl} + \delta_{il} \delta_{jk})$$

In the context of hyper elasticity, by defining W as stored energy density function, we can write:

$$\begin{aligned} S &= \frac{\partial W}{\partial \varepsilon} & \pi(u) &= \int_{\hat{\Omega}_p} W(\varepsilon(U)) \\ D\pi(U)[\varphi_p] &= \int_{\hat{\Omega}_p} \frac{\partial W}{\partial \varepsilon} : D\varepsilon(U)[\varphi_p] \end{aligned} \quad (4.27)$$

$$\begin{aligned}
D^2\pi(U)[\varphi_p, \Delta U] &= \int_{\hat{\Omega}_p} \frac{\partial^2 W}{\partial \varepsilon^2} : D\varepsilon(U)[\varphi_p] : D\varepsilon(U)[\Delta U] \\
&+ \frac{\partial W}{\partial \varepsilon} : D^2\varepsilon(U)[\varphi_p, \Delta U] \\
&= \int_{\hat{\Omega}_p} \mathcal{C} : D\varepsilon(U)[\varphi_p] : D\varepsilon(U)[\Delta U] \\
&+ S(\varepsilon(U)) : D^2\varepsilon(U)[\varphi_p, \Delta U]
\end{aligned} \tag{4.28}$$

$$\mathcal{C} = \begin{bmatrix} 2\mu_p + \lambda_p & 0 & \lambda_p \\ 0 & \mu_p & 0 \\ \lambda_p & 0 & 2\mu_p + \lambda_p \end{bmatrix}$$

$$D^2\varepsilon(U)[\varphi_p, \Delta U] = \frac{1}{2} (\nabla\varphi_p \nabla U^T + \nabla U \nabla\varphi_p^T) \tag{4.29}$$

$$D^2\varepsilon(U)[\varphi_p, \Delta U] = \lim_{\Delta t \rightarrow 0} \frac{D\varepsilon(U + \Delta t \Delta U)[\varphi_p] - D\varepsilon(U)[\varphi_p]}{\Delta t}$$

We solve the solution satisfying:

$$a_s^*(U^k, \Delta u^k, \varphi_p) = R(U^k, \varphi_p)$$

Update the displacement $U^{k+1} = U^k - \Delta U^k$

Break the loop if $\|\Delta u^k\| \leq \textit{epsilon}$

Therefore, the set of linearized residual equations are written as:

$$a^*(U^k, \Delta U^k, \varphi_p) - a(U, \varphi_p) + L(\varphi_p) = 0$$

$$\begin{aligned}
& \frac{\rho_p}{\Delta t^2} \int_{\hat{\Omega}_p} \Delta U^k \cdot \varphi_{p,h} + \int_{\hat{\Omega}_p} \mathcal{C} : D\varepsilon(U_h^{n^k})[\varphi_{p,h}] : D\varepsilon(U_h^{n^k})[\Delta U^k] + \int_{\hat{\Omega}_p} \xi \Delta U^k \\
& \quad \cdot \varphi_{p,h} + \int_{\hat{\Omega}_p} S(\varepsilon(U_h^{n^k})) : D^2\varepsilon(U_h^{n^k})[\varphi_{p,h}, \Delta U^k] \\
& \quad - \frac{\rho_p}{\Delta t^2} \int_{\hat{\Omega}_p} (U_h^{n^k} - 2U_h^{n-1} + U_h^{n-2}) \cdot \varphi_{p,h} - \int_{\hat{\Omega}_p} \xi U_h^{n^k} \cdot \varphi_{p,h} \\
& \quad - \int_{\hat{\Omega}_p} S(\varepsilon(U_h^{n^k})) : D\varepsilon(U_h^{n^k})[\varphi_s] - \int_{\hat{\Gamma}} \gamma_f \mu_f h^{-1} d_\tau U_h^{n^k} \cdot (\varphi_{p,h}) \quad (4.30) \\
& \quad + \int_{\hat{\Gamma}} \hat{J}_s \sigma_{f,h}^{n-1} \hat{F}_s^{-T} n_p(\varphi_{p,h}) + \int_{\hat{\Gamma}} \gamma_f \mu_f h^{-1} v_h^{n-1} \varphi_{p,h} \\
& \quad + b_s(p_{p,h}^{n-1}, \varphi_{p,h}) + \int_{\hat{\Gamma}} \gamma_f \mu_f h^{-1} v_h^{n-1} \cdot t_p \varphi_{p,h} \cdot t_p \\
& \quad + \int_{\hat{\Gamma}} \gamma_f \mu_f h^{-1} (v_h^{n-1} - q_h^{n-1}) \cdot n_p \varphi_{p,h} \cdot n_p = 0
\end{aligned}$$

4.2.4 Darcy problem

Given v_h^{n-1} , $p_{f,h}^{n-1}$ and U_h^n , find $q_h^n, p_{p,h}^n$ in Ω_p such that:

$$\begin{aligned}
& s_0 \int_{\Omega_p} D_t p_{p,h}^n \psi_{p,h} dx + a_p(q_h^n, r_h) - b_p(p_{p,h}^n, r_h) + b_p(\psi_{p,h}, q_h^n) \\
& \quad + \int_{\Gamma} \gamma_f \mu_f h^{-1} q_h^n \cdot n_p r_h \cdot n_p + s_{f,q}(d_\tau q_h \cdot n_p, r_h \cdot n_p) \quad (4.31) \\
& = -b_s(\psi_{p,h}, D_t U_h^n) + \int_{\Gamma} \gamma_f \mu_f h^{-1} (v_h^{n-1} - D_t U_h^{n-1}) \cdot n_p r_h \\
& \quad \cdot n_p + \int_{\Gamma} n_p \cdot \sigma_{f,h}^{n-1} n_p r_h \cdot n_p.
\end{aligned}$$

This problem consists of the dual-mixed weak form of Darcy equations complemented with the following interface condition:

$$p_p^n = -n_p \cdot \sigma_{f,h}^{n-1} n_p - \gamma_f \mu_f h^{-1} (v^{n-1} - D_t U^{n-1} - q_h^n) \cdot n_p, \quad \text{on } \Gamma$$

Based on conditions (4.16), the pressure in the porous media p_p^n has been replaced by the normal component of stress in the fluid phase $\sigma_{f,h}^{n-1}$, computed at the previous time step to improve stability.

4.2.5 Fluid problem

Given $q_h^n, p_{p,h}^n, U_h^n$, find $v_h^n, p_{f,h}^n$ in Ω_f such that:

$$\begin{aligned} & \rho_f \int_{\Omega_f} d_\tau v_h^n \cdot \varphi_{f,h} dx + a_f(v_h^{n-1}, v_h^n, \varphi_{f,h}) - b_f(p_{f,h}^n, \varphi_{f,h}) + b_f(\psi_{f,h}, v_h^n) + s_{f,p}(d_\tau p_{f,h}, \psi_{f,h}) \\ & + s_{f,v}(d_\tau v_h^n \cdot n_f, \varphi_{f,h} \cdot n_f) - \int_\Gamma \sigma_{f,h}(\varsigma \varphi_{f,h}, -\psi_{f,h}) n_f \cdot v_h^n + \int_\Gamma \gamma_f \mu_f h^{-1} v_h^n \cdot \varphi_{f,h} \\ & = - \int_{\Gamma_f^{in}} p_{in}(t) \varphi_f \cdot n_f + \int_\Gamma \sigma_{f,h}^{n-1} n_f \cdot \varphi_{f,h} - \int_\Gamma t_f \cdot \sigma_{f,h}(\varsigma \varphi_{f,h}, -\psi_{f,h}) n_f d_\tau U_h^n \cdot t_f \\ & - \int_\Gamma n_f \cdot \sigma_{f,h}(\varsigma \varphi_{f,h}, -\psi_{f,h}) n_f (q_h^n + d_\tau U_h^n) \cdot n_f + \int_\Gamma \gamma_f \mu_f h^{-1} (q_h^n + d_\tau U_h^n) \\ & \cdot n_f \varphi_{f,h} \cdot n_f + \int_\Gamma \gamma_f \mu_f h^{-1} d_\tau U_h^n \cdot t_f \varphi_{f,h} \cdot t_f. \end{aligned}$$

Here $s_{f,p}(d_\tau p_{f,h}, \psi_{f,h})$ is a stabilization term proposed in [7] acting on the free fluid pressure, that helps to restore the stability of the explicit time advancing scheme, and the role of $s_{f,v}$ is to control the increment of v_h^n over two subsequent time steps, namely we have:

$$s_{f,p}(d_\tau p_{f,h}, \psi_{f,h}) := \gamma_{stab} \frac{h\Delta t}{\gamma_f \mu_f} \int_\Gamma d_\tau p_{f,h}^n \psi_{f,h} \quad (4.32)$$

$$s_{f,v}(d_\tau v_h^n \cdot n, \varphi_{f,h} \cdot n) = \gamma'_{stab} \gamma_f \mu_f \frac{\Delta t}{h} \int_\Gamma d_\tau v_h^n \cdot n \varphi_{f,h} \cdot n \quad (4.33)$$

4.2.6 Mesh movement

Knowing the displacement of the structure interface, classical harmonic extension approach has been proposed to update the fluid mesh in fluid–structure interaction problem. Harmonic extension is explained in [92].

We employ solving diffusion of the interface displacements into the mesh by solving the Laplace equation for each component of the node position in the undeformed configuration $\hat{\Omega}_f$. Where w is the mesh deformation velocity from the original position and γ is a variable diffusion coefficient [6]. The idea is to harmonically expand the evolution of the boundary onto the whole of $\hat{\Omega}_f$. Here basically the fluid field is taken as solution of a homogeneous Laplace problem with boundary conditions imposed by the real solid displacement.

$$\nabla \cdot (\gamma \nabla w) = 0 \quad \text{in } \hat{\Omega}_f \quad (4.34)$$

It is common to consider diffusion coefficient as a constant [9]. In the numerical tests of this chapter, we assume $\gamma=1$ and we solve for (4.35):

$$\begin{aligned} \nabla^2 w &= 0 & \text{in } \hat{\Omega}_f \\ w \cdot n &= 0 & \text{on } \partial \hat{\Omega}_f \setminus \hat{\Gamma}^{\text{in}}, \hat{\Gamma}_f^{\text{in}} \text{ and } \hat{\Gamma}_f^{\text{out}} \\ w &= dU/dt & \text{on } \hat{\Gamma} = \hat{\Omega}_f \cap \hat{\Omega}_p \end{aligned} \quad (4.35)$$

Remark: what is the role of γ ? With the Laplacian method, mesh lines cross and negative volumes occur so the problem cannot be completed. To fix this problem, several authors have proposed a modification to the Laplace method in which a variable diffusivity is introduced [5]. Near the interface the diffusivity is increased making the mesh stiffer. It was found that increasing the diffusivity as the inverse of the square of the mesh length scale was the most effective method.

4.3 NUMERICAL SIMULATIONS

In this section we discuss some numerical experiments aiming at supporting the FPSI algorithm addressed in the previous section. We have implemented the mathematical methods previously described into a numerical solver. For the spatial approximation of the fluid and structure equations we exploit the finite element method. In order to achieve a stable discretization of the divergence-free constraint, we use inf-sup stable mixed finite elements, i.e. *P2-P1* approximation of the velocity and pressure fields, respectively. The system of algebraic equations arising from the finite element method is solved by means of a direct method, which is convenient since the number of degrees of freedom is not exceedingly large. In the stopping criterion for the Newton's method, tolerance of $1e-5$ is adopted. For the time discretization, we use Backward Euler finite difference method. Due to the fast dynamics of the solution and semi-explicit treatment of the fluid convective term ($v^{n+1} \cdot \nabla v^{n+1} \approx v^n \cdot \nabla v^{n+1}$), we have to use very small time step ($\Delta t = 1.e-5$ sec, is used). All computations have been performed using an in house finite element solver written in Freefem++ [41]. For stabilization, the SUPG method is employed [70], discussed also in [93].

We perform numerical experiments on the idealized geometries that can represent blood-tissue systems. Benchmark problem 1 shows the ability of our proposed methodology to capture large deformations in the FPSI problem and is motivated by FSI problems between blood flow and the arterial walls. Next, the proposed methodology is used in benchmark problem 2 to study energy dissipation in the FPSI framework. The geometrical model in this example can resemble 2D model of the left ventricle (LV), similar to the presented LV model in [94].

4.3.1 Benchmark 1: FSI analysis of pulsatile flow in a compliant channel

Our first test case is a variant of the 2D benchmark problem for the flow in a straight tube presented in detail in Section 2.4.1.

In order to assess the impact of extending the study to finite elasticity we have performed two simulations, using hyperelastic model and linear elasticity model for the elastic skeleton of the porous media in the arterial wall. More precisely, in one simulation we simplify the Green strain tensor to its linear part as $E(U) = \frac{1}{2}(\nabla U + \nabla U^T)$ for the structure; and the second one we use the complete Green strain tensor, $E(U) = \frac{1}{2}(\nabla U + \nabla U^T + (\nabla U) \nabla U^T)$. For each model (linear and nonlinear) we study the propagation of a single pressure wave following pressure profile, with 2 different values for P_{\max} ; one using reference value for $P_{\max} = 13334 \text{ dyne/cm}^2$ which generates small deformation in the structure called the “weak” wave, and the other one using $10 \times P_{\max}$ that can produce large deformation in the wall.

$$p_{in}(t) = \begin{cases} \frac{p_{max}}{2} \left(1 - \cos\left(\frac{2\pi t}{T_{max}}\right) \right) & \text{if } t \leq T_{max} \\ 0 & \text{if } t > T_{max} \end{cases} \quad (4.36)$$

The inlet pressure pulse generates a wave that inflates the channel near the inlet, travels through the channel, and hits the outlet of the tube. We consider a point at the middle of the wall and plot displacement of this point vs. time, depicted in the upper panel of the plots in Figure 22. The lower panel shows magnified displacement of the wall at $t=3\text{ms}$; when the pressure wave is almost at the middle of the channel, for a qualitative comparison that illustrates the differences between the two cases. When the applied pressure and the strains are small (left panel of Figure 22), the linear and nonlinear solutions nearly coincide and we have one to one match for the displacement. However, when the strains become large (right panel), nonlinear effects become significant and we notice observable differences in the displacement magnitude. We observe that the amplitudes of the displacement predicted by the small deformation model is consistently smaller than that predicted by the finite deformation model.

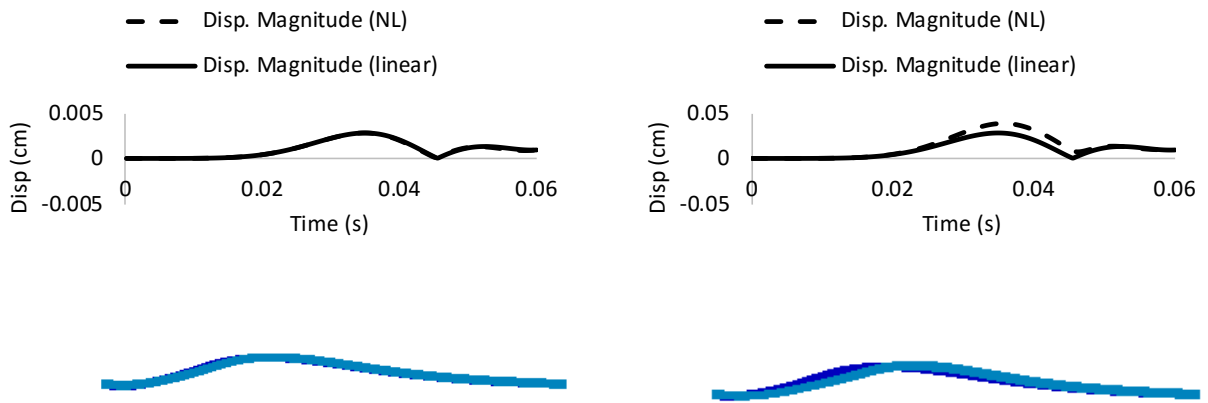


Figure 22. Left (weak pressure wave), right (strong pressure wave), Attached plots shows comparison for displacement at the middle of the wall for linear (dashed) and nonlinear (solid line) elasticity.

4.3.2 Benchmark 2: FSI analysis of the flow in a cross-section model

In this example the dynamical behavior of a poroelastic material subjected to a time dependent loading from the fluid, is investigated. We describe new benchmark settings for the evaluation of the energy loss in FPSI problems. We consider the problem of injecting an incompressible fluid in a poroelastic medium with a uniform cross-section, which results in expansion of the structure. We identify the area occupied by the fluid region, and the structure region as depicted in Figure 23. The cross section is considered to be a circular sector made of nonlinear, poroelastic, isotropic, and nearly incompressible material with the following dimensions: inner radius R_i , outer radius equal to R_o . The fluid and structure regions are separated by an interface. The geometry dimensions are provided in Table 6.

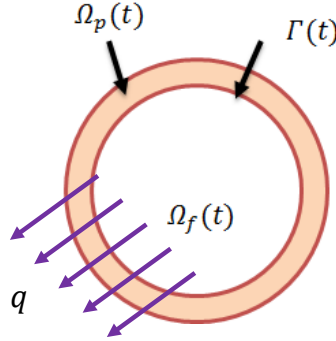


Figure 23. Schematic of the geometrical model for benchmark problem 2.

A source term g will be considered in (4.38) to model the injection. This injection phase is needed in order to inflate/deflate the geometry.

$$\rho_f \left(\frac{\partial v}{\partial t} + v \cdot \nabla v \right) = \nabla \cdot \sigma_f \quad \text{in } \Omega_f(t) \quad (4.37)$$

$$\nabla \cdot v = g \quad \text{in } \Omega_f(t) \quad (4.38)$$

The flow is driven by the injection of the fluid into a circle (2D) that represents the fluid domain. Then fluid is drained out of the media. All presented simulations in this part have been performed using a sine-type source term with the amplitude of 30 s^{-1} . We choose a simple sine function according to:

$$g(t) = g_{max} \left(\sin \left(\frac{\pi t}{T_{max}} \right) \right) \quad \text{if } t \leq T_{max} \quad (4.39)$$

$$g_{max} = 30 \text{ s}^{-1} \quad T_{max} = 0.003 \text{ s} \quad Q(t) = Area(t) \times g(t) \quad \rightarrow \quad g = \frac{Q(t)}{Area(t)}$$

Table 6. Physical and numerical parameters for benchmark problem 1

Parameters	values	Parameters	values
R_i (cm)	0.5	Lame coeff. μ_p (dyne/cm ²)	1.07×10^6
R_o (cm)	0.4	Lame coeff. λ_p (dyne/cm ²)	4.28×10^6
wall thickness (cm)	0.1	k (cm ³ s/g)	5×10^{-9}
wall density (g/cm ³)	1.1	s_0 (cm ² /dyne)	5×10^{-6}
Fluid density (g/cm ³)	1	γ_f, γ_s	2500
Dynamic viscosity (poise)	0.035	Final time	6ms

The formulation also accounts for detailed variations in fluid pressure and flow across the thickness. Plots in Figure 25 show the filtration velocity and porous media pressure through the thickness of the wall, due to steadily increasing internal pressure. Since fluid pressure is constrained to be zero at the outer radial surface, Darcy pressure starts from zero at exterior and reaches its maximum at interior (inside channel), as expected.

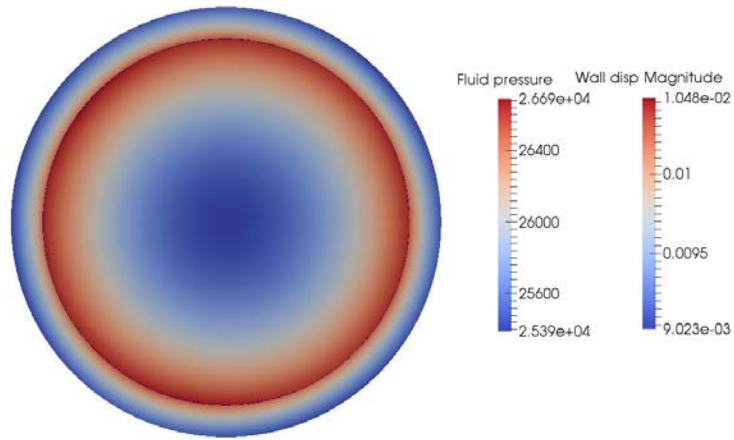


Figure 24. Snapshot for fluid and wall during expansion phase in the model at 2ms; colors represent fluid pressure and wall displacement

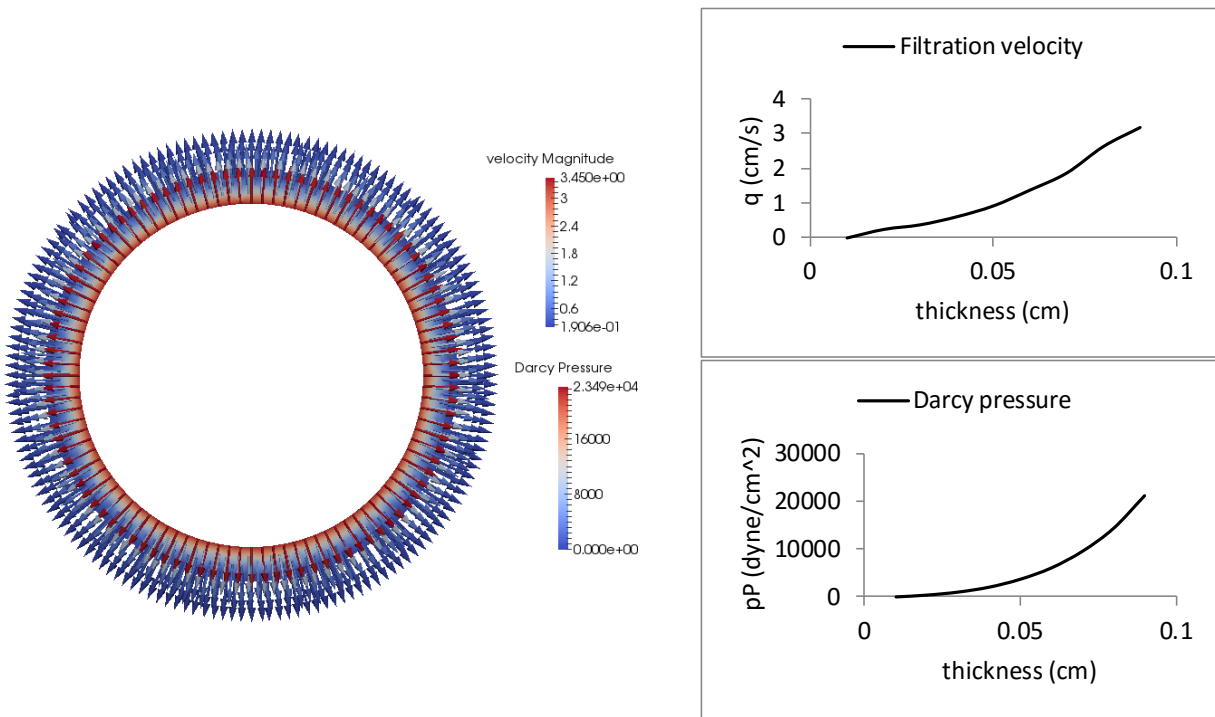


Figure 25. Filtration velocity through the wall and Darcy pressure at $t=2\text{ms}$ for the test case with loading rate= 6ms and $k=5\times 10^{-6}$

In order to determine the optimal mesh size to use, a mesh sensitivity analysis has been carried out on the 2D cross sectional model. We solved several test cases with different mesh sizes of the structure using the reference values provided in Table 6.

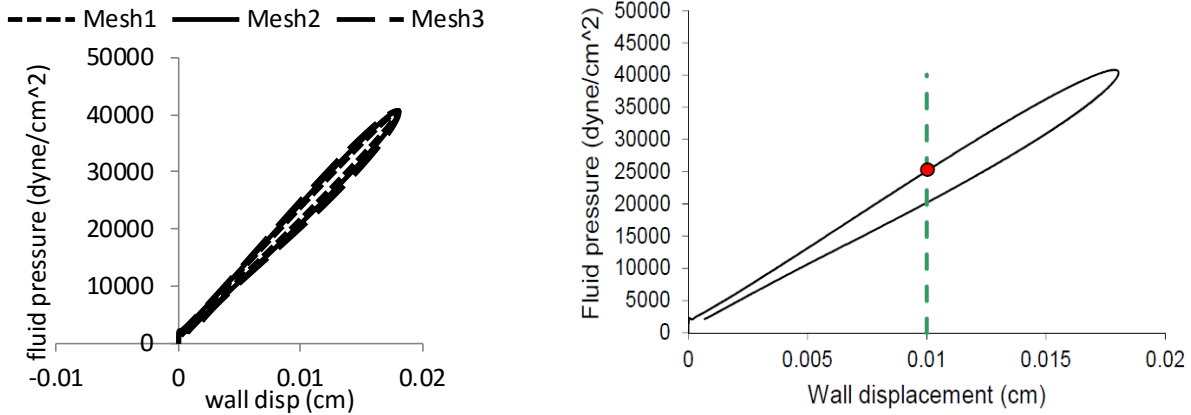


Figure 26. Hysteresis loop for different mesh size (left), Schematic of the measuring indicator used in the sensitivity analysis (right)

Table 7. Mesh sensitivity results

	# of cell in Ω_s	$P_f \times 10^4$ (dyne/cm ²)	Time step size	$P_f \times 10^4$ (dyne/cm ²)
Mesh 1	1788	2.40	Δt	2.48
Mesh 2	3992	2.48	$\Delta t/2$	2.49
Mesh 3	9194	2.51		

We compared the difference in the hysteresis loop between the three different mesh sizes presented in the left panel of Figure 26. To this purpose, we define an indicator as the pressure in the loading curve at 0.01 cm value for the displacement (right panel of Figure 26). The results are provided in Table 7 and Figure 27. The mesh sensitivity analysis shows that after Mesh2 results are almost insensitive to increasing the number of nodes. For this reason, we conclude

that Mesh 2 has an optimal size to evaluate the hysteresis loop with good accuracy. Therefore, this mesh density has been used for all the following tests.

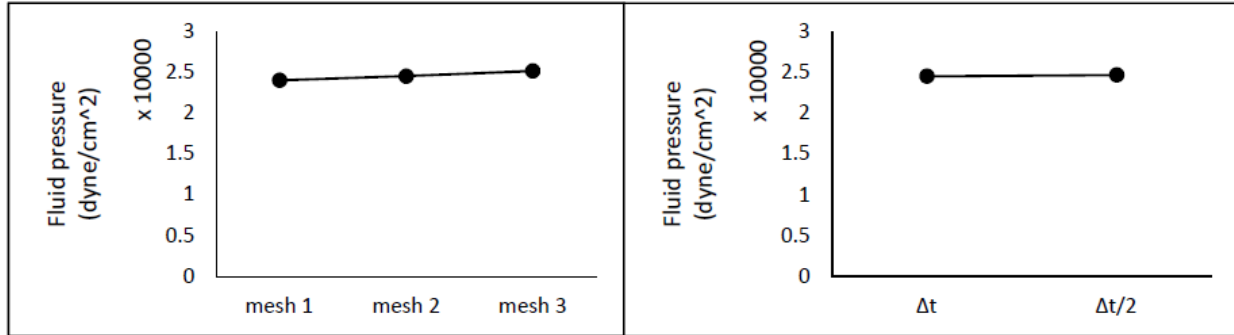


Figure 27. Mesh sensitivity analysis plots for different mesh sizes (left) and time steps (right)

4.3.3 Sensitivity analysis of model parameters

In order to show the importance of including the poroelastic model for the structure region, we investigate the effects of the material properties of the poroelastic region on the fluid pressure vs the structure deformation loop; called hysteresis loop in this study, when porous media characteristics depart from the values reported in Table 6. We show that different values of the storativity coefficient and permeability lead to differences in the hysteresis loop. We also look at the dependence hysteresis loop on the stiffness of the poroelastic skeleton and loading rate.

4.3.3.1 Loading rate and source term amplitude

We consider three different amplitude of the sine-type source term. We change amplitude such that we inject same amount of fluid at different loading rates. That is, T_{\max} assumes the following values 3ms, 6ms, 12ms in order to study the sensitivity.

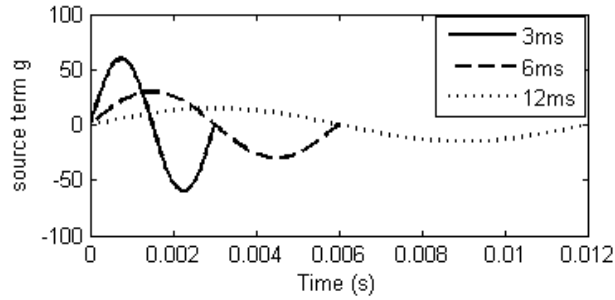


Figure 28. Different source terms g

In Figure 29 and Figure 30, the hysteresis loop for different loading rate values and different amplitudes of the source term are analyzed. In these simulations the hydraulic conductivity has been set to the value of $k=5\times 10^{-6}$. We observe that the fluid pressure dissipates more in the high loading regime i.e by increasing g the size of hysteresis loop increases significantly.

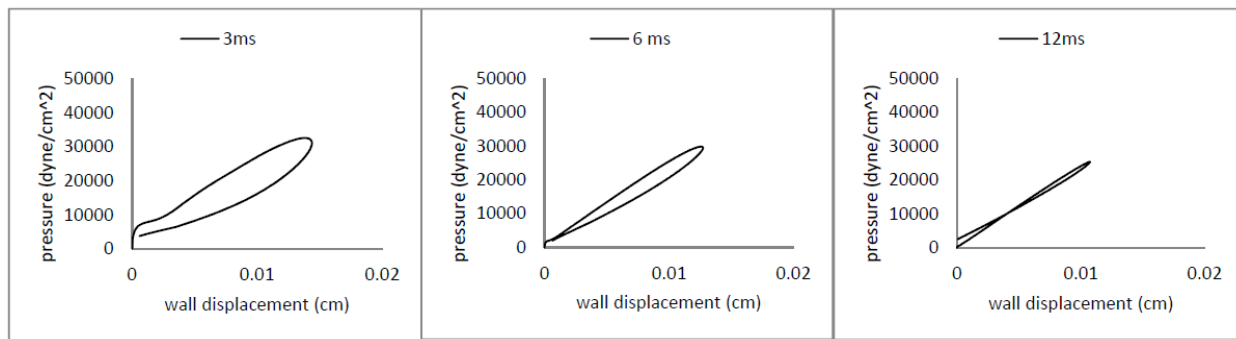


Figure 29. Comparing loops for different values of loading rate, with $k=5e-6$

Figure 31 shows the comparison of the fluid and Darcy pressure as well as the displacement and filtration velocity vectors obtained in different loading rate regimes. In the case of high loading rate (3ms), plots in Figure 31 show that time variation of Darcy pressure, namely dPp/dt , is bigger and so there exists large pore pressure gradient (dPp/dx) from the beginning as

well. Hence, the filtration velocity can attain high velocity quickly; as thus the energy loss occurs much quicker than small loading rate (12 ms) due to the rapid fluid flow. When there is small pressure gradient (dPp/dx), the filtration fluid flow (q) is not able to achieve a high velocity in the short time due to the high damping.

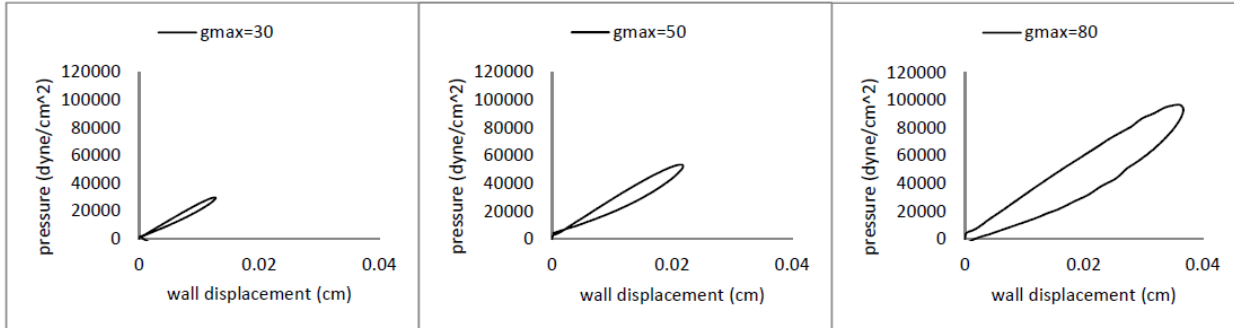


Figure 30. Comparing hysteresis loop for different values of the source term g

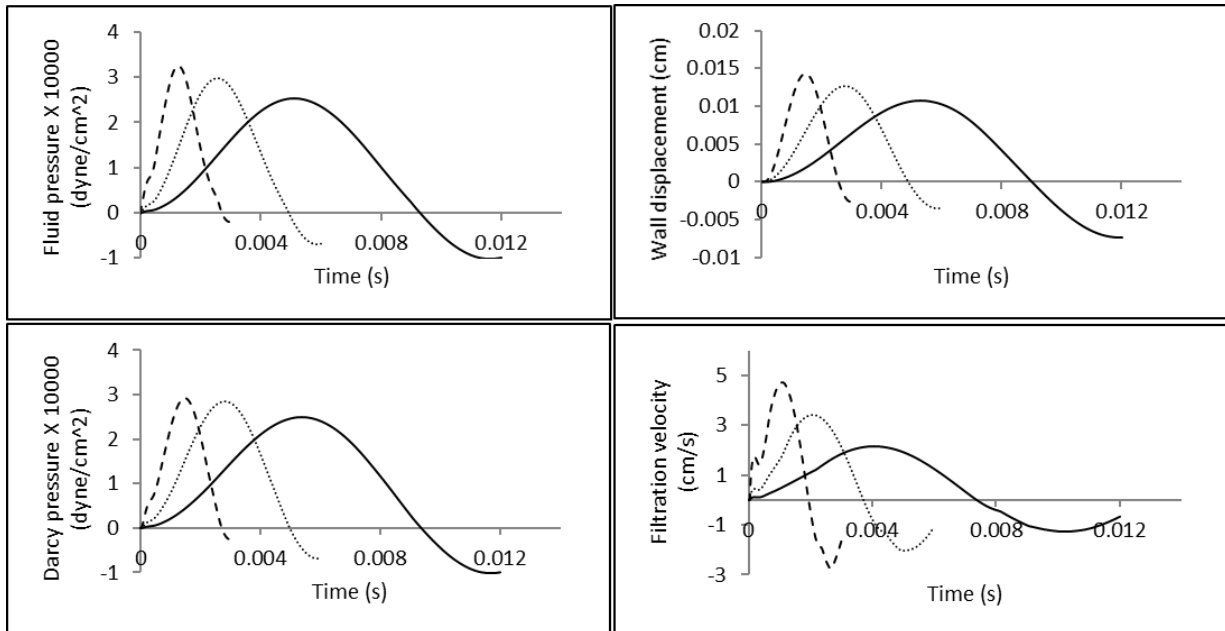


Figure 31. Comparing fluid pressure, wall displacement, Darcy pressure and filtration velocity for different values of loading rate, 3ms (dashed), 6ms (dotted), and 12ms (solid) lines

4.3.3.2 Young's modulus

We investigate the influence of Young's modulus E on the pressure relaxation loop. We use $k=5 \times 10^{-6}$ and the loading rate of 6ms for these simulations. Then, we study the behavior of the system when we increase and decrease the Young modulus 10 times from its reference value.

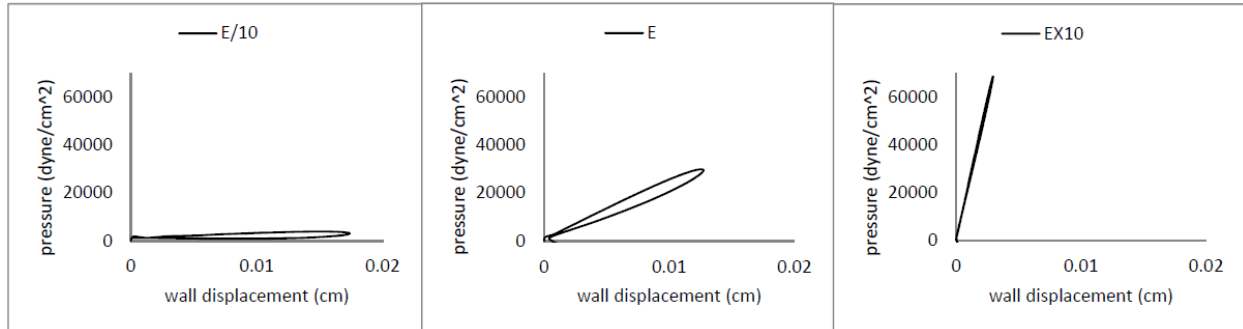


Figure 32. Comparing hysteresis loop for different values of Young's modulus

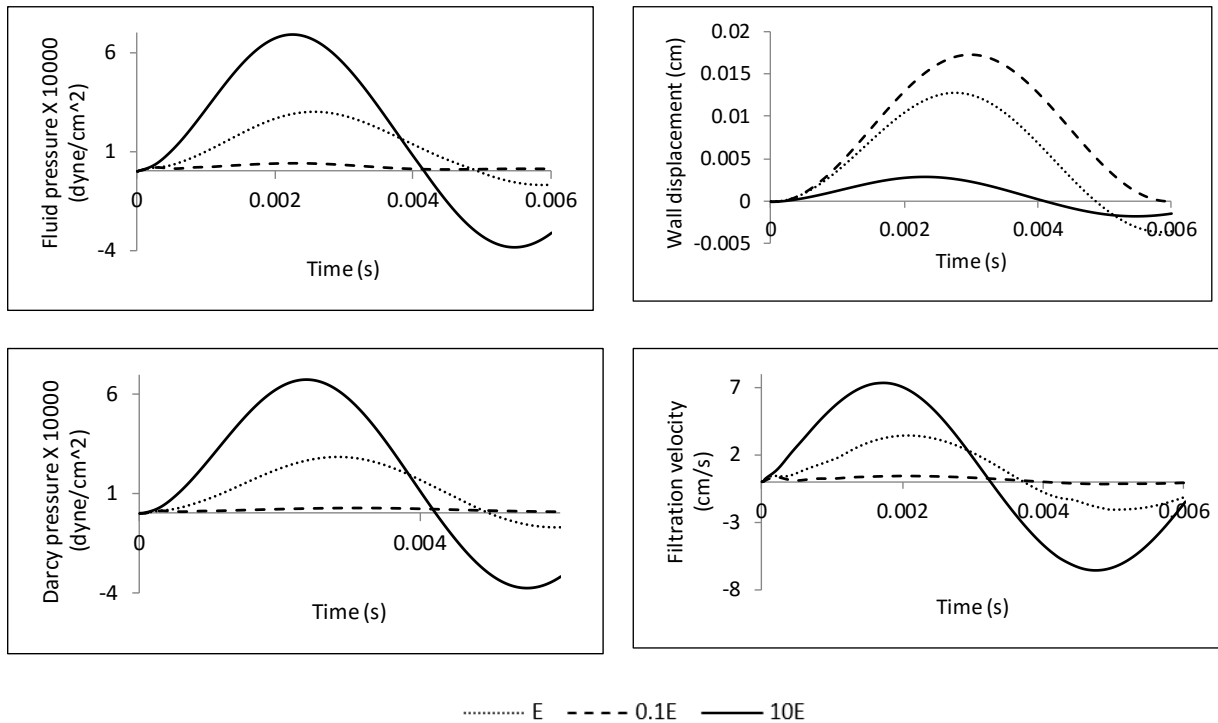


Figure 33. Comparing fluid pressure, wall displacement, Darcy pressure and filtration velocity for different values of Young's modulus, $0.1 \times E$ (dashed), E (dotted), and $10 \times E$ (solid) lines

In Figure 32, we analyze the effect of changing Young modulus of the elastic skeleton on energy dissipation. For the same simulations, pressure values in the fluid and porous media as well as velocity and displacement fields are shown in Figure 33. Results clearly show that for very stiff material, the intramural flow squeezes out so hard and quick that the material behaves as in a single phase elastic material.

4.3.3.3 Storage coefficient

To complete the description of elastic response under fluid infiltration, we also need to specify how the storage of fluid within material elements changes due to stressing and pressurization. We assume full saturation of all connected pore space. We observe that changing the storativity coefficient, which is related to the compressibility of the poroelastic system, causes a significant difference in the hysteresis loop. In other words, increasing s_0 leads to increase in the fluid mass content by changing the porosity and pressure, which results in more dissipation.

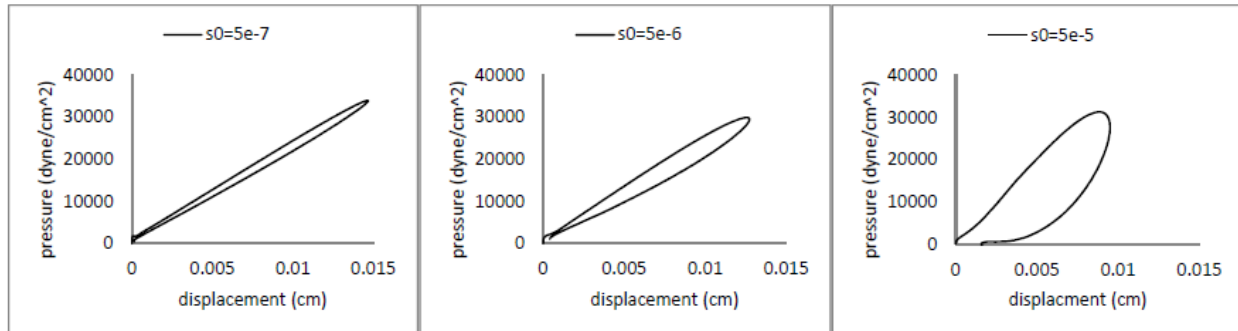


Figure 34. Comparing hysteresis loop for different values of storage coefficient s_0

4.3.3.4 Hydraulic conductivity

Figure 35 informs us about the sensitivity of hysteresis loop with respect to hydraulic conductivity. We observe that, as expected; increasing hydraulic conductivity, increases the dissipation and we have bigger loop.

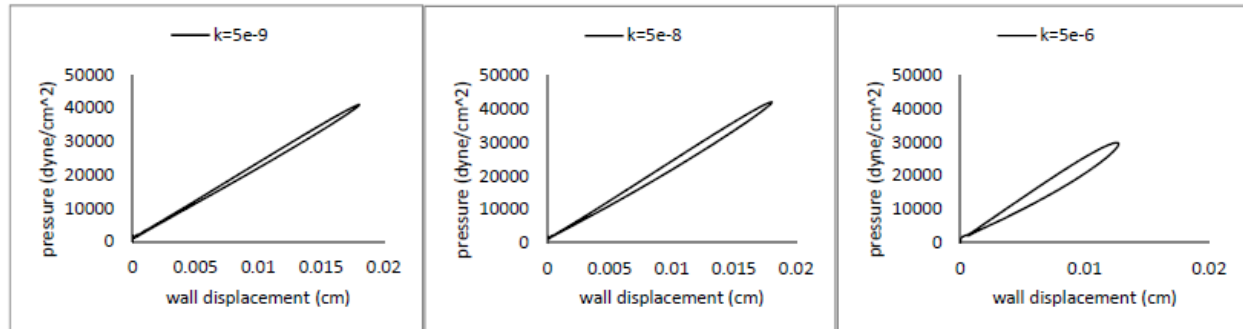


Figure 35. Comparing hysteresis loop for different values of hydraulic conductivity

The sensitivity analysis of hydraulic conductivity may help to give interpretation of the mechanical behavior of tissue engineered vascular grafts (TEVGs). These grafts are porous [95] and in [96], the hydraulic conductivity of $k=10^{-7}$ cm².s/g is considered for the arterial graft which is in the range of k for our sensitivity study. Using FPSI model is crucial to investigate how the prosthetic graft behaves in different configurations from implantation (initial time) to matured artery, as well as in estimating the risk of both mechanical mismatch in the initial stages and the eventual rupture.

4.4 DISCUSSION

In the benchmark problem 2, after the poroelastic structure expands to attain equilibrium strain, pore fluid flow arises within the structure. Both the magnitude of the deformation of the material and the energy loss associated with its deformation are affected by the flow of the viscous fluid within the structure, that we call filtration velocity. Using our FPSI model, we investigate the variation of the filtration velocity inside the poroelastic structure. A remarkable feature of the numerical results is that the velocity field in the porous matrix has a large variation in the radial direction. Indeed, in Figure 25 we observe that the filtration velocity changes through the thickness and so $\text{div}(q) \neq 0$. For an incompressible flow in a rigid porous matrix that behavior would be impossible, because it violates the divergence free constraint, arising from the mass conservation law.

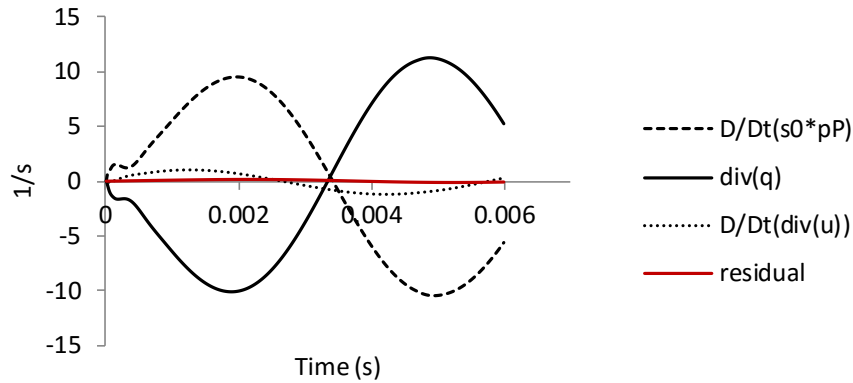


Figure 36. Time variation of mass conservation terms in the Biot model through the wall thickness

However, in a poroelastic material this effect may be possible. For this reason, we aim to validate the expressions $(\frac{D}{Dt}(s_0 p_p + \nabla \cdot U) + \nabla \cdot q = 0)$ in the Biot model, derived under the mass conservation assumption inside the pores of the porous medium. Figure 36 shows the time

variation of the different components of this expression for benchmark problem 2. This plot confirms that $\text{div}(q)$ is remarkably large. Also, we observe that the residual of this equation is almost zero, which confirms that mass conservation in average is satisfied in the porous matrix.

An important contribution of this chapter is the use of porohyperelastic structural model in fluid structure interaction to elaborate on energy dissipation in the poroelastic media. The energy loss in the poroelastic media has been determined by solving Biot's complete equations of poroelasticity for the case of the interaction between the fluid and a poroelastic structure. Dissipation in porous media depends only on the relative motion between the pore fluid and the skeleton. More precisely, the dissipation vanishes when there is no relative motion of fluid and solid [97]. According to [98] and [86] viscous forces retard the filtration velocity within the structure and the relative fluid movement might cause significant energy loss. We have analyzed the influence of the model parameters on these effects.

Our results suggest that energy loss depends both on the fluid filtration speed (q) and on the poroelastic parameters (hydraulic conductivity k and storativity s_0). When the load frequency is low, the fluid flows slowly through the porous medium, so that little energy is lost in a cycle due to viscosity of the fluid filling the pores. Therefore, the behavior of the system approaches that of an elastic system. The same is true for very small permeability values. In the opposite situation, if load is applied abruptly to a poroelastic material, the energy dissipation is significant since the flow through the wall increases. In our simulations, in the case of high loading rates (3ms), plots in Figure 31 show that dP_p/dt is higher and there exists larger pore pressure from the beginning of the loading phase. So the filtration velocity can attain higher values more rapidly. as thus the energy loss occurs much quicker than slower loading rate (12 ms) due to the rapid fluid flow. This observation is in agreement with results obtained in [99] for studying the

dynamic stability of the poroelastic medium. The idea of dependency of the energy loss to the load frequency is also investigated in Yeh-Tyai [100]. They evaluated the complex dynamic modulus of the poroelastic media which is a measure of damping in the system, which shows that there is a frequency at which maximum loss modulus occurs and it depends on the dissipation coefficient and the length to thickness ratio of the poroelastic slab.

Lastly, by comparing the time-dependent deformation properties of the poroelastic medium in the FPSI framework with viscoelastic model, one can identify the relative contributions of poroelasticity and solid matrix viscoelasticity in these time-dependent behaviors. indeed, the study of the time-dependent deformation properties of the poroelastic medium in the FPSI framework helps to identify the similarities between poroelasticity and solid matrix viscoelasticity. In [5] it is stated that a porous model has the viscoelastic character of a living tissue because of the motion of the pore fluid. The hysteresis exhibited by viscoelastic materials is an outcome of the fact that some part of the stored energy in these materials during loading gets dissipated and cannot be recovered. Therefore, these materials will come back to their initial configuration through a different unloading path. The dissipative behavior that we observe for poroelastic model for high loading rates, is similar to the hysteresis loop in the viscoelastic model (such as Figure 19, top and middle panel). More precisely, poroelasticity and viscoelasticity may result in the similar energy dissipation in experiments, and this work gives a mechanistic explanation of this analogy.

The magnitude of displacement has significant effect on the energy loss in the poroelastic model, and the dynamic behavior (rate effect, i.e how fast the loading is applied) excites the loss. In other words, when the model is subject to high internal pressure gradients, which are producing large filtration fluid flow such as in benchmark 2, then poroelastic material behavior

and energy dissipation are noticeable. For the benchmark 1 case, volume change (dilation) is small and filtration velocity is negligible. Hence, the poroelastic model features time-dependent behavior associated primarily with the solid-phase deformation and the effect of poroelasticity on hysteresis loop is negligible.

We also study the sensitivity of the amplitude of the pressure-displacement hysteresis cycle with respect to some parameters, namely storativity, permeability, loading frequency and young modulus. To this purpose we define a *quantitative indicator* of the hysteresis cycle amplitude that we call for simplicity the *hysteresis amplitude* (HA). It measures the amplitude of the cycle as the difference of pressure in the loading and unloading curves at 75% of maximum displacement (Figure 37). In all charts, this indicator ranges between 2000 and 30000 dyne/cm². Using the numerical experiments of Figure 29-Figure 35, we have studied the variation of HA when each parameter is varied individually. The outcome of the analysis is reported in Figure 38. For a better comparison of the different charts, the parameters are normalized with respect to a reference values that are chosen as follows: $s_0=5\times 10^{-6}$, $k=5\times 10^{-6}$, loading frequency = 1/0.006, $E=1\times 10^7$. The data points corresponding to the reference value are highlighted in red.

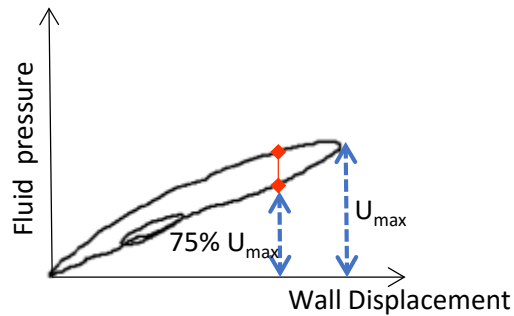


Figure 37. Schematic of the measuring indicator used in the sensitivity analysis

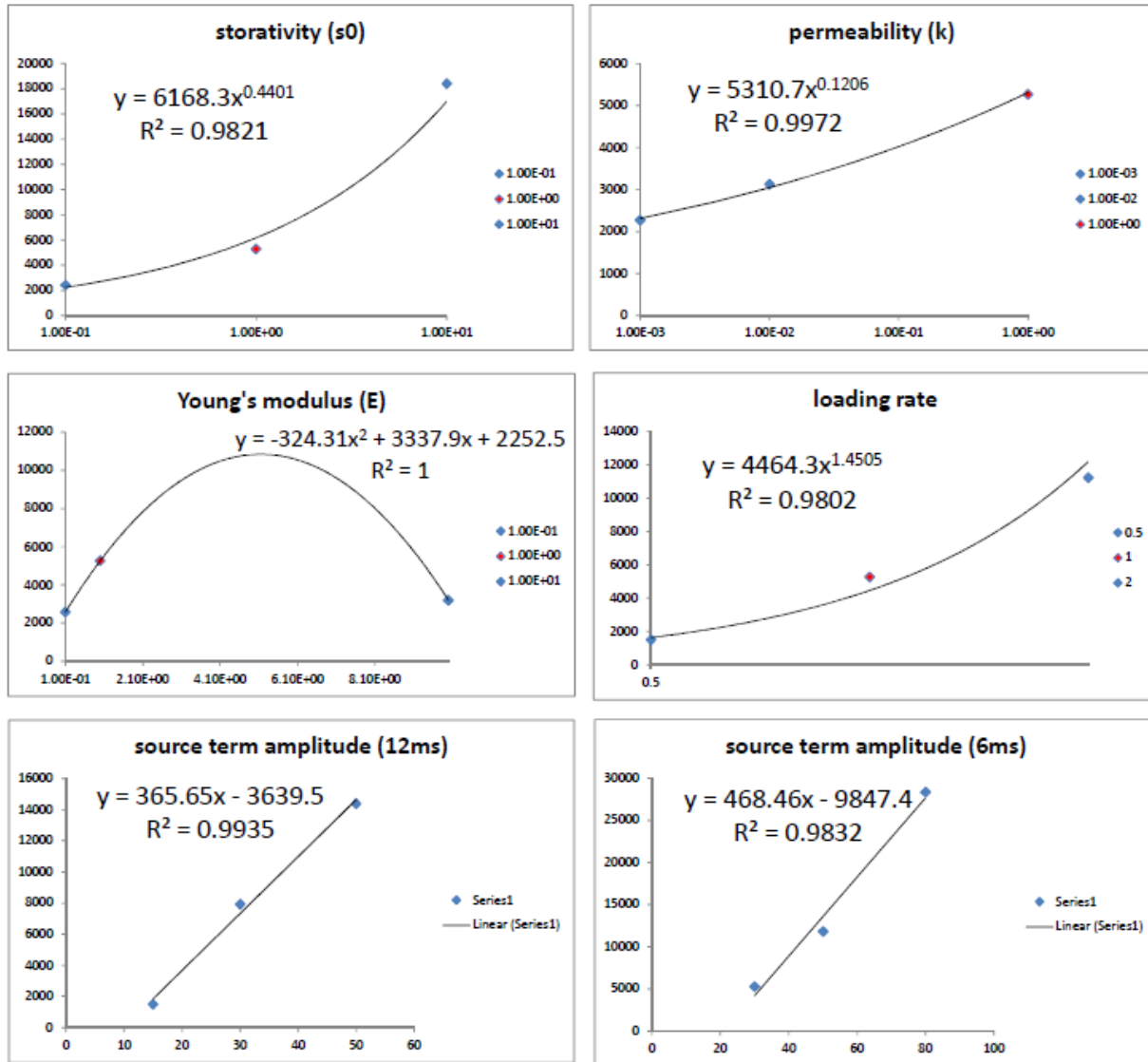


Figure 38. Sensitivity results for dependence of hysteresis loop to the model parameters

We observe that the amplitude of the hysteresis cycle increases with the storativity, permeability and loading frequency. We also observe that the dependence of the hysteresis amplitude from the parameters is nonlinear. Since the data for storativity, permeability and loading frequency feature a similar increasing trend, we have fitted them using a power law

model, namely $y = c \cdot x^p$, where (p) is the exponent that quantifies the sensitivity of the quantity of interest (y) with respect to the control parameter (x) and c is a scaling constant.

We observe that, thanks to the renormalization, all the charts show a similar behavior and the scaling constants are comparable, but the exponents of the power law are different. In particular, the loading frequency shows the maximum impact on the hysteresis, followed by the storativity and the permeability (Table 8).

The dependence of the hysteresis cycle from the Young modulus is of difficult interpretation. We believe that our analysis substantially shows that the pressure-displacement cycle is barely affected by the stiffness of the material.

Table 8. Exponent of the power law for different parameters on the sensitivity analysis

Parameter	value of the exponent (p) in $y = c \cdot x^p$
Loading rate	1.4505
Storativity	0.4401
permeability	0.1206

The last column of plots shows the variation of the pressure-displacement cycle when we vary the amplitude of the source term. This analysis is performed for two different loading rates. In both cases we observe a linear dependence of the hysteresis amplitude from the source term magnitude. This would be the observed trend for any linear partial differential equation, which sets a linear dependence of the solution from the right hand side. However, the model adopted here is nonlinear, especially in the regime of large deformations. More precisely, we observe up to 10% displacement for higher amplitude of the source term, which is for sure in the regime of

large deformations and therefore we need large deformation formulation to handle this problem. Indeed, the results confirm that this is when we have significant poroelastic coupling effect and hysteresis loop. However, we observe that by increasing the loading amplitude the hysteresis indicator shows linear increase with respect to the loading amplitude which says that the response of the model to variation of the load is still linear.

5.0 CONCLUSION

In the context of hemodynamics, we have developed a computational model for the interaction between pulsatile fluid flow in a channel, confined with a thick poroelastic wall. In order to approximate this problem, we have proposed and analyzed a partitioned, loosely coupled finite element solver based on weak enforcement of interface conditions using Nitsche's method that allows us to independently solve the equations at each time step. Namely, structure mechanics, the intramural filtration and the fluid flow problem are solved separately at each time step. In this way, we uncouple the original problem into the parts defined on separate subregions, which leads to a more efficient calculation of the numerical solution. This method can accommodate a mixed formulation for the Darcy's equations and it guarantees stability as well, provided that several penalty and stabilization parameters are appropriately selected. To improve the accuracy of the scheme, we have also considered its application as a preconditioner for the fully coupled (monolithic) FSI problem formulation, with very encouraging results both for performance and accuracy of the method. The theoretical results have been complemented by numerical simulations. We have tested our algorithm on 2D and 3D idealized geometries to simulate the propagation of the pressure waves and the related wall deformation. Also, our computational method allowed us get an accurate representation of the intramural flow within the wall.

Also, we have performed a sensitivity analysis of the effects of poroelastic parameters on FSI results. More precisely, by means of a collection of numerical experiments, we qualitatively analyze how the poroelastic phenomena affect the propagation of pressure waves and the wall displacement. We conclude that increasing the hydraulic permeability (leaky domain) decreases the amplitude of pressure wave, which means that we have more dissipation.

In order to enhance our understanding of the underlying phenomena of poroelasticity, we have analyzed the role of intramural fluid flow in the apparent viscoelastic behavior of the poroelastic wall. To this aim, we have studied the energy exchange in the interaction between the blood flow and the arterial wall, to investigate the distribution and dissipation of the energy delivered to the artery during one heart cycle. We have compared the energy distribution when the wall is modeled using different constitutive models: namely elastic, viscoelastic and poroelastic. Although this analysis has informed us about qualitative energy exchange due to conductivity of the pores and corresponding filtration velocity, we haven't observed any hysteresis loop for the poroelastic model. Therefore, based on the hypothesis that large deformations and nonlinear elasticity may trigger the poroelastic effects, we have moved to finite elasticity formulation of the poroelastic media in a FSI framework.

We have investigated numerically the effects of poroelasticity parameters, as well as loading rate and loading magnitude, on the energy dissipation. Namely, we distinguish a fast loading rate, a high storativity and a high permeability case in the Darcy equations, and the obtained hysteresis loops are compared for different values of each model parameter. By employing finite elasticity in our FPSI solver, the results show that the energy loss differs substantially between poroelastic model and elastic wall models, and confirmed that accurate

representation of the structure model as a poroelastic medium is essential for low loading frequencies, and high hydraulic conductivity and storativity.

Both poroelasticity and viscoelasticity are coupled solid-fluid problems but in different ways. Perhaps the most interesting feature of the model studied in this work is its capability of explicitly capturing these two distinct phenomena. Namely, one is the influence of fluid viscosity on the vessel wall dynamics (poroelasticity), and a separate one is the vessel wall viscoelastic mechanical properties that is modeled by utilizing a linearly viscoelastic model based on Kelvin-Voigt viscoelasticity. It is shown that the mechanism of the energy dissipation of the poroelastic material is different from that of a conventional solid material because of the interaction between the fluid and solid phase. In the poroelastic material, the energy dissipation and related hysteresis loop is not primarily because of effects within the material of the skeleton itself. It is because the skeleton is permeated with fluid. Therefore, we conclude that the effect of the transmural flow in the total structure stress should be accounted depends on poroelastic parameters value. In summary, the results in this thesis highlight the importance of including both poroelasticity and viscoelasticity in modeling fluid-structure interaction.

All the previous results illustrate the role of poroelasticity on the mechanics of soft tissues in general. For the specific case of cardiovascular applications, some partially conclusive results are available in Chapter 3. There, we have performed a test case that resembles a medium size artery, see in particular Section 3.4.2 “Benchmark 2: FSI analysis under physiological condition”. This test case highlights some characteristic features on the poro-visco-elastic behavior of an artery, which are outlined below:

- The dissipative effect of intramural flow on the mechanical energy of the artery, is relevant for high hydraulic conductivities of the arterial wall. These values are

significantly larger than the physiological permeability of healthy arteries (see Table 5). Indeed, in Section 3.4.2, benchmark problem 2, we barely see any effect for poroelasticity when comparing it to the elastic one for the physiological range of permeability parameter. For larger values of permeability, our results confirm that the poroelastic model appreciably changes the displacement and wave propagation speed in structure as well as the energy distribution.

- In the physiological range of material parameters, the viscous dissipation in the blood flow is the dominant dissipative term during a heartbeat. Only in the range of high vascular permeability and in the late diastole phase, intramural filtration dissipates comparable amount of energy (see Figure 17 of Chapter 3). For small permeability values, we barely notice any contribution related to intramural filtration. We also observe that the energy dissipated in the wall is a small fraction of that dissipated by the fluid.
- If a viscoelastic behavior is accounted for, non-negligible energy losses can be observed even in the case of healthy tissue (see Figure 17).
- Viscoelasticity is responsible for establishing a hysteresis loop in the pressure vs displacement plots. In contrast, poroelasticity does not generate any hysteresis, under physiological conditions (see Figure 19).
- The results of Chapter 4 (more precisely Figures 29-35) also suggest that high deformation rates in the solid matrix trigger effects of hysteresis in the poroelastic material. However, to observe these effects, the deformations rates that we use are remarkably higher than the physiological ones.

These conclusions will be further strengthened when a few limitations of this work will be overcome:

- The computational results are affected by significant uncertainty on the physiological parameters characterizing the poro-visco-elastic behavior of an artery. To our best knowledge, the parameters that describe a healthy artery are collected in Table 5. Better experiments or more advanced modeling approaches based on mathematical homogenization might in future fill this knowledge gap.
- We did not explore the variations of the geometric configuration of the artery, but we are aware that the conclusions of this study may no longer apply to small arteries, such as the cerebral arteries, for example.
- At the level of numerical methods, more accurate discretization schemes may be adopted, in order to improve the mass and energy conservation properties of the simulator.

For future work, the main focus will be to minimize the computational cost due to the iterations between the fluid and solid sub problems, especially in the nonlinear solver. Decreasing computational cost, makes us able to solve for more complicated geometries which is particularly important for the biomedical applications of this work, namely for the interaction between the blood flow and the arterial wall, to reach the goal of simulating realistic vascular districts. Another interesting application of this work will be to simulate LDL transport or drug delivery through the arterial walls, with pulsatile blood flow. In this case, a mass transfer model, coupled to the FPSI problem shall be implemented. In [101, 102] a mathematical model has been developed to capture the interplay between blood perfusion, fluid exchange with the interstitial volume, and mass transport in the capillary bed, through the capillary walls and into the

surrounding tissue. Our model can be combined with [101] to provide a poroelastic description of the interstitial tissue, in order to capture the interplay of mechanical deformations and transport phenomena.

BIBLIOGRAPHY

1. Chapelle, D., et al., *A poroelastic model valid in large strains with applications to perfusion in cardiac modeling*. Computational Mechanics, 2009. **46**(1): p. 91-101.
2. Calo, V.M., et al., *Multiphysics model for blood flow and drug transport with application to patient-specific coronary artery flow*. Computational Mechanics, 2008. **43**(1): p. 161-177.
3. Feenstra, P.H. and C.A. Taylor, *Drug transport in artery walls: A sequential porohyperelastic-transport approach*. Computer Methods in Biomechanics and Biomedical Engineering, 2009. **12**(3): p. 263-276.
4. Badia, S., A. Quaini, and A. Quarteroni, *Coupling Biot and Navier-Stokes equations for modelling fluid-poroelastic media interaction*. Journal of Computational Physics, 2009. **228**(21): p. 7986-8014.
5. Koshiba, N., et al., *Multiphysics simulation of blood flow and LDL transport in a porohyperelastic arterial wall model*. J Biomech Eng, 2007. **129**(3): p. 374-85.
6. McCutchen, C.W., *Cartilage is poroelastic, not viscoelastic (including an exact theorem about strain energy and viscous loss, and an order of magnitude relation for equilibration time)*. Journal of Biomechanics, 1982. **15**(4): p. 325-327.
7. Yang, Z. and P. Smolinski, *Dynamic finite element modeling of poroviscoelastic soft tissue*. Computer Methods in Biomechanics and Biomedical Engineering, 2006. **9**(1): p. 7-16.
8. Bukac, M., et al., *Effects of Poroelasticity on Fluid-Structure Interaction in Arteries: a Computational Sensitivity Study*, in *Modeling the Heart and the Circulatory System*. 2015, Springer. p. 197-220.
9. Prosi, M., et al., *Mathematical and numerical models for transfer of low-density lipoproteins through the arterial walls: a new methodology for the model set up with applications to the study of disturbed lumenal flow*. J Biomech, 2005. **38**(4): p. 903-17.
10. Chepelenko, G.V., *Atherosclerosis regulation via media lipid-driven VSMC cholesterol efflux switch*. Medical Hypotheses, 2015. **84**(2): p. 141-144.

11. Smith, E., *Transport, interactions and retention of plasma proteins in the intima: the barrier function of the internal elastic lamina*. European heart journal, 1990. **11**(suppl E): p. 72-81.
12. Smith, E. and R. Slater. *In Atherogenesis: Initiating Factors*. in *Ciba Foundation Symposia, New Series*. 1973.
13. Bertolotti, C. and V. Deplano, *Three-dimensional numerical simulations of flow through a stenosed coronary bypass*. J Biomech, 2000. **33**(8): p. 1011-22.
14. Bazilevs, Y., et al., *Isogeometric fluid-structure interaction analysis with applications to arterial blood flow*. Computational Mechanics, 2006. **38**(4-5): p. 310-322.
15. Nichols, W., M. O'Rourke, and C. Vlachopoulos, *McDonald's Blood Flow in Arteries, Sixth Edition: Theoretical, Experimental and Clinical Principles*. 2011: Taylor & Francis.
16. Armentano, R.L., et al., *Arterial wall mechanics in conscious dogs. Assessment of viscous, inertial, and elastic moduli to characterize aortic wall behavior*. Circ Res, 1995. **76**(3): p. 468-78.
17. Čanić, S., et al., *Modeling viscoelastic behavior of arterial walls and their interaction with pulsatile blood flow*. SIAM Journal on Applied Mathematics, 2006. **67**(1): p. 164-193.
18. Fung, Y., et al., *Biomechanics, its foundations and objectives*. 1972: Prentice-Hall.
19. Holzapfel, G.A., T.C. Gasser, and M. Stadler, *A structural model for the viscoelastic behavior of arterial walls: Continuum formulation and finite element analysis*. European Journal of Mechanics, A/Solids, 2002. **21**(3): p. 441-463.
20. Causin, P., J.F. Gerbeau, and F. Nobile, *Added-mass effect in the design of partitioned algorithms for fluid-structure problems*. Computer Methods in Applied Mechanics and Engineering, 2005. **194**(42-44): p. 4506-4527.
21. Kennedy, J.M. and T.B. Belytschko, *Theory and application of a finite element method for arbitrary Lagrangian-Eulerian fluids and structures*. Nuclear Engineering and Design, 1982. **68**(2): p. 129-146.
22. MIKELIĆ, A. and M.F. WHEELER, *ON THE INTERFACE LAW BETWEEN A DEFORMABLE POROUS MEDIUM CONTAINING A VISCOUS FLUID AND AN ELASTIC BODY*. Mathematical Models and Methods in Applied Sciences, 2012. **22**(11): p. 1250031.
23. Ganis, B., et al., *Modeling fractures in a poro-elastic medium*. Oil & Gas Science and Technology-Revue d'IFP Energies nouvelles, 2014. **69**(4): p. 515-528.

24. Girault, V., et al., *A lubrication fracture model in a poro-elastic medium*. Mathematical Models and Methods in Applied Sciences, 2014: p. 1-59.
25. Badia, S., A. Quaini, and A. Quarteroni, *Coupling Biot and Navier–Stokes equations for modelling fluid–poroelastic media interaction*. Journal of Computational Physics, 2009. **228**(21): p. 7986-8014.
26. Zakerzadeh, R., et al. *Computational models for fluid-structure interaction with a poroelastic structure*. in *APS Division of Fluid Dynamics Meeting Abstracts*. 2013.
27. Bukač, M., et al., *Partitioning strategies for the interaction of a fluid with a poroelastic material based on a Nitsche’s coupling approach*. Computer Methods in Applied Mechanics and Engineering, 2015. **292**: p. 138-170.
28. Zakerzadeh, R. and P. Zunino. *Fluid-structure interaction in arteries with a poroelastic wall model*. in *Biomedical Engineering (ICBME), 2014 21th Iranian Conference on*. 2014. IEEE.
29. Zakerzadeh, R. and P. Zunino, *Fluid-Structure Interaction in Arteries with a Poroelastic Wall Model*. 21st Iranian Conference of Biomedical Engineering (ICBME) IEEE,,: p. 35 - 39.
30. Zakerzadeh, R., M. Bukac, and P. Zunino, *Computational analysis of energy distribution of coupled blood flow and arterial deformation*. International Journal of Advances in Engineering Sciences and Applied Mathematics, 2015: p. 1-16.
31. Zakerzadeh, R. and P. Zunino, *Fluid-Structure interaction modeling in deformable porous arteries*. Bulletin of the American Physical Society, 2015. **60**.
32. Zakerzadeh, R. and P. Zunino, *Numerical modeling of fluid-porous structure interaction in arteries*. 2016.
33. Tully, B. and Y. Ventikos, *Coupling poroelasticity and cfd for cerebrospinal fluid hydrodynamics*. IEEE Transactions on Biomedical Engineering, 2009. **56**(6): p. 1644-1651.
34. Ma, X., G.C. Lee, and S.G. Wu, *Numerical Simulation for the Propagation of Nonlinear Pulsatile Waves in Arteries*. Journal of Biomechanical Engineering, 1992. **114**(4): p. 490-496.
35. Bukač, M., et al., *Partitioning strategies for the interaction of a fluid with a poroelastic material based on a Nitsche’s coupling approach*. Computer Methods in Applied Mechanics and Engineering, 2014.
36. Hansbo, P., *Nitsche's method for interface problems in computa-tional mechanics*. GAMM-Mitteilungen, 2005. **28**(2): p. 183-206.

37. Burman, E. and M.A. Fernández, *Stabilization of explicit coupling in fluid-structure interaction involving fluid incompressibility*. Computer Methods in Applied Mechanics and Engineering, 2009. **198**(5-8): p. 766-784.
38. Burman, E. and M.A. Fernández, *Explicit strategies for incompressible fluid-structure interaction problems: Nitsche type mortaring versus Robin–Robin coupling*. International Journal for Numerical Methods in Engineering, 2014. **97**(10): p. 739-758.
39. Ambartsumyan, I., et al., *Simulation of Flow in Fractured Poroelastic Media: A Comparison of Different Discretization Approaches*, in *Finite Difference Methods, Theory and Applications: 6th International Conference, FDM 2014, Lozenetz, Bulgaria, June 18-23, 2014, Revised Selected Papers*, I. Dimov, I. Faragó, and L. Vulkov, Editors. 2015, Springer International Publishing: Cham. p. 3-14.
40. Bukac, M., Yotov, I., Zakerzadeh, R., and Zunino P., *Effect of poroelasticity on fluid-structure interaction in arteries: a computational sensitivity study*. Modeling the heart and the circulatory system, 2014. **vol 13** (MS&A, Springer Italia).
41. Hecht, F., *New development in freefem+*. Journal of Numerical Mathematics, 2012. **20**(3-4): p. 251-265.
42. Bukač, M., et al., *Fluid-structure interaction in blood flow capturing non-zero longitudinal structure displacement*. Journal of Computational Physics, 2013. **235**: p. 515-541.
43. Quarteroni, A. and A. Valli, *Numerical approximation of partial differential equations*. Vol. 23. 2008: Springer Science & Business Media.
44. Brezzi, F. and J. Pitkäranta, *On the Stabilization of Finite Element Approximations of the Stokes Equations*, in *Efficient Solutions of Elliptic Systems: Proceedings of a GAMM-Seminar Kiel, January 27 to 29, 1984*, W. Hackbusch, Editor. 1984, Vieweg+Teubner Verlag: Wiesbaden. p. 11-19.
45. Nobile, F., M. Pozzoli, and C. Vergara, *Time accurate partitioned algorithms for the solution of fluid–structure interaction problems in haemodynamics*. Computers & Fluids, 2013. **86**(0): p. 470-482.
46. Caro, C.G., et al., *The mechanics of the circulation, second edition*. The Mechanics of the Circulation, Second Edition. 2011. 1-524.
47. Barbenel, J.C., *The Arterial Wall*, in *Arteries and Arterial Blood Flow*, C.M. Rodkiewicz, Editor. 1983, Springer Vienna. p. 129-177.
48. Humphrey, J.D. and S.L. Delange, *An Introduction to Biomechanics: Solids and Fluids, Analysis and Design*. 2004: Springer.
49. Cowin, S.C. and J.D. Humphrey, *Cardiovascular soft tissue mechanics*. 2001: Springer.

50. Cowin, S.C. and S.B. Doty, *Tissue mechanics*. Tissue Mechanics. 2007. 1-682.
51. Formaggia, L., et al., *On the coupling of 3D and 1D Navier-Stokes equations for flow problems in compliant vessels*. Computer Methods in Applied Mechanics and Engineering, 2001. **191**(6-7): p. 561-582.
52. Gerbeau, J.-F., M. Vidrascu, and P. Frey, *Fluid–structure interaction in blood flows on geometries based on medical imaging*. Computers & Structures, 2005. **83**(2–3): p. 155-165.
53. Nobile, F., *Numerical approximation of fluid-structure interaction problems with application to haemodynamics*. 2001, EPFL.
54. Skalak, R., et al., *The Energy Distribution in the Pulmonary Circulation, II: Experiments*. Physics in Medicine and Biology, 1966. **11**(3): p. 437.
55. Skalak, R., et al., *The Energy Distribution in the Pulmonary Circulation, I: Theory*. Physics in Medicine and Biology, 1966. **11**(2): p. 287.
56. Bertram, C.D., *Energy dissipation and pulse wave attenuation in the canine carotid artery*. Journal of Biomechanics, 1980. **13**(12): p. 1061-1073.
57. Tsaturyan, A.K., et al., *Extracellular fluid filtration as the reason for the viscoelastic behaviour of the passive myocardium*. Journal of Biomechanics, 1984. **17**(10): p. 749-755.
58. Huyghe, J.M., *Non-linear finite element models of the beating left ventricle and the intramyocardial coronary circulation*. Ph.D. thesis, 1986.
59. Yang, M. and L.A. Taber, *The possible role of poroelasticity in the apparent viscoelastic behavior of passive cardiac muscle*. J Biomech, 1991. **24**(7): p. 587-97.
60. Armentano, R., et al., *Effects of hypertension on viscoelasticity of carotid and femoral arteries in humans*. Hypertension, 1995. **26**(1): p. 48-54.
61. London, G.M. and B. Pannier, *Arterial functions: how to interpret the complex physiology*. Nephrology dialysis transplantation, 2010. **25**(12): p. 3815-3823.
62. Canic, S., et al., *Blood flow in compliant arteries: an effective viscoelastic reduced model, numerics, and experimental validation*. Ann Biomed Eng, 2006. **34**(4): p. 575-92.
63. Bukac, M. and S. Canic, *Longitudinal displacement in viscoelastic arteries: a novel fluid-structure interaction computational model, and experimental validation*. Math Biosci Eng, 2013. **10**(2): p. 295-318.
64. Badia, S., A. Quaini, and A. Quarteroni, *Splitting methods based on algebraic factorization for fluid-structure interaction*. SIAM Journal on Scientific Computing, 2007. **30**(4): p. 1778-1805.

65. Warriner, R.K., K.W. Johnston, and R.S.C. Cobbold, *A viscoelastic model of arterial wall motion in pulsatile flow: Implications for Doppler ultrasound clutter assessment*. *Physiological Measurement*, 2008. **29**(2): p. 157-179.
66. Badia, S., A. Quaini, and A. Quarteroni, *Splitting methods based on algebraic factorization for fluid-structure interaction*. *SIAM Journal on Scientific Computing*, 2008. **30**(4): p. 1778-1805.
67. Grandmont, C., M. Lukáčová-Medvid'ová, and Š. Nečasová, *Mathematical and Numerical Analysis of Some FSI Problems*, in *Fluid-Structure Interaction and Biomedical Applications*, T. Bodnár, G.P. Galdi, and Š. Nečasová, Editors. 2014, Springer Basel. p. 1-77.
68. Muha, B. and S. Čanić, *Existence of a solution to a fluid–multi-layered-structure interaction problem*. *Journal of Differential Equations*, 2014. **256**(2): p. 658-706.
69. Bukac, M., Yotov, I., Zakerzadeh, R., and Zunino P. *Partitioning strategies for the interaction of a fluid with a poroelastic material based on a Nitsche's coupling approach*. *ArXiv e-prints*, 2014. **1403**, 5707.
70. Brooks, A.N. and T.J. Hughes, *Streamline upwind/Petrov-Galerkin formulations for convection dominated flows with particular emphasis on the incompressible Navier-Stokes equations*. *Computer methods in applied mechanics and engineering*, 1982. **32**(1): p. 199-259.
71. Hasegawa, H. and H. Kanai, *Measurement of elastic moduli of the arterial wall at multiple frequencies by remote actuation for assessment of viscoelasticity*. *Japanese journal of applied physics*, 2004. **43**(5S): p. 3197.
72. Bukač, M., et al., *A modular, operator-splitting scheme for fluid-structure interaction problems with thick structures*. *International Journal for Numerical Methods in Fluids*, 2014. **74**(8): p. 577-604.
73. Quaini, A., *Algorithms for fluid-structure interaction problems arising in hemodynamics*. 2009.
74. Bukac, M., *A Fluid-structure Interaction Model Capturing Longitudinal Displacement in Arteries: Modeling, Computational Method, and Comparison with Experimental Data*. 2012, University of Houston.
75. Craiem, D., et al., *Cardiovascular engineering: modelization of ventricular-arterial interaction in systemic and pulmonary circulation*. *Latin American applied research*, 2005. **35**(2): p. 111-114.
76. Polzer, S., et al., *Impact of poroelasticity of intraluminal thrombus on wall stress of abdominal aortic aneurysms*. *BioMedical Engineering OnLine*, 2012. **11**: p. 62-62.

77. Govindaraju, K., et al., *Effect of porous media of the stenosed artery wall to the coronary physiological diagnostic parameter: a computational fluid dynamic analysis*. *Atherosclerosis*, 2014. **233**(2): p. 630-5.
78. Page, R.C. and H.E. Schroeder, *Pathogenesis of inflammatory periodontal disease. A summary of current work*. *Lab Invest*, 1976. **34**(3): p. 235-49.
79. Ayyalasomayajula, A., J.P. Vande Geest, and B.R. Simon, *Porohyperelastic finite element modeling of abdominal aortic aneurysms*. *J Biomech Eng*, 2010. **132**(10): p. 104502.
80. Dabagh, M., et al., *Distribution of shear stress over smooth muscle cells in deformable arterial wall*. *Med Biol Eng Comput*, 2008. **46**(7): p. 649-57.
81. Prosi, M., et al., *Mathematical and numerical models for transfer of low-density lipoproteins through the arterial walls: a new methodology for the model set up with applications to the study of disturbed luminal flow*. *Journal of Biomechanics*, 2005. **38**(4): p. 903-917.
82. Balzani, D., et al., *Numerical modeling of fluid–structure interaction in arteries with anisotropic polyconvex hyperelastic and anisotropic viscoelastic material models at finite strains*. *International journal for numerical methods in biomedical engineering*, 2015.
83. Tricceri, P., et al., *Fluid-structure interaction simulations of cerebral arteries modeled by isotropic and anisotropic constitutive laws*. *Computational Mechanics*, 2015. **55**(3): p. 479-498.
84. Quaini, A. and A. Quarteroni, *A semi-implicit approach for fluid-structure interaction based on an algebraic fractional step method*. *Mathematical Models and Methods in Applied Sciences*, 2007. **17**(6): p. 957-983.
85. Taber, L.A. and A.M. Puleo, *Poroelastic plate and shell theories*, in *Mechanics of Poroelastic Media*. 1996, Springer. p. 323-337.
86. Costi, J.J., et al., *Frequency-dependent behavior of the intervertebral disc in response to each of six degree of freedom dynamic loading: solid phase and fluid phase contributions*. *Spine*, 2008. **33**(16): p. 1731.
87. Le Tallec, P. and J. Mouro, *Fluid structure interaction with large structural displacements*. *Computer Methods in Applied Mechanics and Engineering*, 2001. **190**(24): p. 3039-3067.
88. Discacciati, M. and A. Quarteroni, *Navier-Stokes/Darcy coupling: modeling, analysis, and numerical approximation*. *Revista Matemática Complutense*, 2009. **22**(2): p. 315-426.

89. Uzuoka, R. and R.I. Borja, *Dynamics of unsaturated poroelastic solids at finite strain*. International Journal for Numerical and Analytical Methods in Geomechanics, 2012. **36**(13): p. 1535-1573.
90. Quarteroni, A., R. Sacco, and F. Saleri, *Numerical mathematics*. Vol. 37. 2010: Springer Science & Business Media.
91. Razzaq, M., et al., *Numerical Simulation and Benchmarking of Fluid Structure Interaction with Application to Hemodynamics*. 2009: Techn. Univ., Fak. für Mathematik.
92. Jendoubi, A., J. Deteix, and A. Fortin, *A simple mesh-update procedure for fluid–structure interaction problems*. Computers & Structures, 2016. **169**: p. 13-23.
93. *Finite Element Methods*, in *Robust Numerical Methods for Singularly Perturbed Differential Equations: Convection-Diffusion-Reaction and Flow Problems*. 2008, Springer Berlin Heidelberg: Berlin, Heidelberg. p. 277-425.
94. Ijiri, T., et al., *A Kinematic Approach for Efficient and Robust Simulation of the Cardiac Beating Motion*. PLoS ONE, 2012. **7**(5): p. e36706.
95. Ravi, S. and E.L. Chaikof, *Biomaterials for vascular tissue engineering*. Regenerative medicine, 2010. **5**(1): p. 107.
96. Bjork, J.W. and R.T. Tranquillo, *Transmural flow bioreactor for vascular tissue engineering*. Biotechnology and bioengineering, 2009. **104**(6): p. 1197-1206.
97. Biot, M.A., *Theory of propagation of elastic waves in a fluid-saturated porous solid. I. Low-frequency range*. The Journal of the acoustical Society of america, 1956. **28**(2): p. 168-178.
98. Ren, H., G. Goloshubin, and F.J. Hiltebrandt, *Poroelastic analysis of permeability effects in thinly layered porous media*. Geophysics, 2009. **74**(6): p. N49-N54.
99. Cederbaum, G., L. Li, and K. Schulgasser, *Poroelastic structures*. 2000: Elsevier.
100. Yeh, F.-H. and H.-S. Tsay, *Dynamic behavior of a poroelastic slab subjected to uniformly distributed impulsive loading*. Computers & Structures, 1998. **67**(4): p. 267-277.
101. Nabil, M., P. Decuzzi, and P. Zunino, *Modelling mass and heat transfer in nano-based cancer hyperthermia*. Royal Society Open Science, 2015. **2**(10).
102. Nabil, M., P. Zunino, and L. Cattaneo, *A Computational Study of Microscale Flow and Mass Transport in Vasculatized Tumors*. 21st Iranian Conference of Biomedical Engineering (ICBME) Pages 23-28, IEEE,, 2015.